Maria João Borlido Oliveira Lima

Phytoplankton dynamics off southern Portugal: a physical-biological approach

Faculdade de Ciências e Tecnologia

2021

Maria João Borlido Oliveira Lima

Phytoplankton dynamics off southern Portugal: a physical-biological approach

Master in Marine and Coastal Systems

Work performed under the supervision of:

Prof. Dr. Ana Barbosa

Prof. Dr. Paulo Relvas

Faculdade de Ciências e Tecnologia

2021

Phytoplankton dynamics off southern Portugal: a physical-biological approach

Declaração de autoria de trabalho

Declaro ser a autora deste trabalho, que é original e inédito. Autores e trabalhos consultados estão devidamente citados no texto e constam da listagem de referências incluída.

Maria João Borlido Oliveira Lima

Copyright

Acknowledgements

I would like to express my sincere gratitude to my supervisors, Dr Ana Barbosa and Dr Paulo Relvas, for their invaluable support at every stage of the master thesis, and for transmitting their considerable knowledge and experience that encourages me to pursue a research career. I would also like to thank Dr Lilian Krug, for her insightful suggestions, and for motivating me during difficult times. This thesis is strongly supported on abundance of toxigenic phytoplankton groups made available by Instituto Português do Mar e da Atmosfera (Portuguese Institute of the Sea and Atmosphere - IPMA). I deeply acknowledge the free, high-quality harmful algal bloom data retrievable from IPMA public database. Furthermore, this master thesis was supported by a scholarship within the scope of the project MAR-01.04.02-FEAMP-0003 – CONPRAR – "Contributo para a Proteção do recurso amêijoa *Ruditapes decussatus* no ecossistema da Ria Formosa". This project provided me with the opportunity and funding to work with phytoplankton data from the Ria Formosa, and relate the occurrence of potentially toxigenic species inside this coastal lagoon with the natural processes acting at adjacent coastal waters (addressed in the current thesis). I would also like to recognize the continuous effort of OceanColor, Copernicus Marine Service, Ocean Productivity, "Centro de Investigação Marinha e Ambiental", and other groups that provide free, regular, and high-quality oceanographic products to the scientific community. My appreciation also extends to my life partner, André Lopes, who patiently nurtured me when I most needed, and dear friends (Rita, Piri, Davide, Cláudia, Ben), for always making me laugh during tough times. Lastly, to my entire family, in particular my parents, Maria Helena and João Manuel, for believing in me in every single step of the way since I first expressed a profound admiration and respect for the great ocean.

Abstract

Identifying the environmental drivers of phytoplankton blooms, especially harmful algal blooms, has become imperative for forecasting these events. This study aimed to evaluate phytoplankton variability patterns, phenology and underlying environmental determinants within specific regions off southern Portugal, during a 6-year period (2014-2019). Phytoplankton phenology was assessed using region-specific chlorophyll-a concentration (Chl-a) and abundance of phytoplankton taxa, responsible for amnesic (ASP), diarrhetic (DSP) and paralytic shellfish poisoning (PSP), and relationships between abiotic environmental variables and phytoplankton were explored using Generalized Additive Models (GAM). Over oceanic regions, Chl-a showed a unimodal annual cycle, with increases during the mixed layer deepening phase and late-winter to early-spring maxima. The slope and coastal regions showed an additional summer peak, related with local upwelling, more prominent for the west coast. The development of a coastal counter-current that probably transports riverine nutrients and phytoplankton biomass, might have also contributed for Chl-a increase over the south coast. GAM explained from 14% to 77% of Chl-a variance, with higher explanatory power for oceanic and coastal regions under riverine influence. Sea surface temperature, photosynthetically available radiation, and mixed layer depth emerged as the most influential predictors, and large-scale climate indices showed minor effects. ASP-producing species showed a bimodal annual cycle for most coastal production areas, with first bloom onset in spring, and peak timing during late-spring and summer, associated with upwelling conditions that favour diatom blooms. DSP and PSP-producers exhibited a unimodal annual cycle, peaking during late-summer and late-spring, respectively, during upwelling relaxation periods. DSP models explained between 21% and 54% of the deviance, whereas ASP models revealed a weaker performance (7-8%). In addition to the referred Chl-a predictors, high river discharges exerted a negative influence on both ASP- and DSP-producers. Downwelling/countercurrent regimes globally favoured DSP-producers, while upwelling promoted ASP-producers only over the most southeastern coastal area. Future predictions of harmful phytoplankton blooms for the area should then consider the identified influential predictors but must be complemented with additional environmental variables, and explore specific periods (e.g., seasons, extreme events) and hybrid modelling approaches.

Keywords: phytoplankton variability, phytoplankton phenology, harmful algal blooms, environmental drivers, hydrodynamic regime, generalized additive models

Resumo

O fitoplâncton é o principal produtor primário em ecossistemas marinhos, responsável pela assimilação de CO_2 proveniente da atmosfera e transferência de energia para níveis superiores da rede trófica, incluindo os recursos pesqueiros. A variabilidade temporal e espacial do fitoplâncton está relacionada com diversos fatores ambientais, tais como o vento, as correntes oceânicas, o afloramento costeiro, a radiação e temperatura do oceano, turbulência e nutrientes inorgânicos. A identificação dos principais fatores que controlam o florescimento de fitoplâncton, em particular, de espécies produtoras de toxinas, é fundamental para os modelos preditivos, de forma a anteciparem os possíveis impactos associados a futuros florescimentos de algas nocivas.

Na presente tese pretendeu-se avaliar os padrões de variabilidade sazonal e interanual do fitoplâncton, bem como identificar os principais forçadores ambientais que ditam a sua abundância em diferentes regiões ao largo da costa sudoeste portuguesa (três regiões costeiras, uma região sob o talude continental e duas oceânicas) caracterizadas por diferentes regimes hidrodinâmicos, durante um período de seis anos (2014-2019). Um conjunto de dados provenientes de deteção remota por satélite (direção e velocidade do vento, temperatura à superfície do oceano, radiação fotossinteticamente ativa e concentração de clorofila-a, Chl-a), modelos (profundidade da camada de mistura), observações *in situ* (descargas fluviais dos rios Guadiana e Guadalquivir, abundância de grupos de fitoplâncton potencialmente produtores de toxinas e concentração de biotoxinas em duas espécies alvo de moluscos bivalves, *Mytilus* spp. e *Donax trunculus*) e indicadores climáticos de larga escala (*Multivariate El Niño Southern Oscillation* - ENSO, *North Atlantic Oscillation* - NAO, *Atlantic Multidecadal Oscillation* - AMO, *East Atlantic* - EA, *Western Mediterranean Oscillation* - WeMO) foi utilizado para analisar os padrões de variabilidade intra- e interanual do fitoplâncton. Em particular, as séries temporais de Chl-a e abundância dos grupos de fitoplâncton produtores de toxinas que ocorrem regularmente ao longo da costa portuguesa, em diferentes regiões ou áreas costeiras de produção de moluscos bivalves foram utilizadas para descrever os padrões fenológicos do fitoplâncton. A fenologia baseou-se na análise das seguintes métricas: intensidade, frequência, duração e períodos de iniciação, máximo e término das florescências de fitoplâncton. A aplicação de modelos aditivos generalizados (GAM) a cada região permitiu identificar os forçadores ambientais relevantes para a previsão de Chl-a e dos dois grupos de fitoplâncton mais frequentemente detetados ao largo da costa sudoeste portuguesa, responsáveis pelas síndromes intoxicação amnésica por marisco (*Amnesic Shellfish Poisoning*, ASP) e intoxicação

diarréica por marisco (*Diarrhetic Shellfish Poisoning*, DSP). Adicionalmente, estes modelos foram ainda utilizados para identificar os padrões de variabilidade intra-anuais e interanuais de Chl-a e dos grupos de fitoplâncton potencialmente produtores de toxinas amnésicas (ASP) e diarréicas (DSP). A distribuição Gaussiana com função de ligação identidade foi aplicada à transformação logarítmica da Chl-a, enquanto para os grupos de fitoplâncton produtores de ASP e DSP, a regressão Binomial Negativa com função de ligação logarítmica foi considerada a mais adequada para ultrapassar o problema de sobredispersão na base de dados. No entanto, a presença de sobredispersão nos dados de abundância do grupo produtor de DSP, em determinadas áreas de produção de bivalves (L6 e L7c-L8), mesmo após a aplicação da regressão Binomial Negativa, sugere que se deveria considerar modelos Zero Inflacionados. Contudo, estes últimos não convergiram para nenhuma área, tendo-se optado pelos resultados obtidos com a primeira distribuição (Binomial Negativa).

De modo geral, a Chl-a nas regiões oceânicas exibiu um ciclo anual unimodal, com aumentos durante a fase de aprofundamento da camada de mistura devido ao incremento de nutrientes e/ou à diminuição da mortalidade, e um máximo relativo entre o final do inverno e o início da primavera, provavelmente relacionado com alterações da temperatura e estratificação da camada superficial do oceano. Adicionalmente, filamentos de *upwelling*, estruturas de mesoescala formadas durante períodos de afloramento costeiro, constituem um importante mecanismo de adveção entre águas costeiras e oceânicas, tal como verificado para a zona oceânica ao largo da costa oeste. A região sob o talude continental exibiu um segundo pico de Chl-a no verão, resultante da combinação dos efeitos da estratificação da coluna da água associada a baixa disponibilidade de nutrientes, e da advecção de nutrientes a partir das zonas costeiras adjacentes durante eventos de afloramento forte. As regiões costeiras também apresentaram um máximo adicional de Chl-a no verão, relacionado com o afloramento costeiro, mais intenso na costa oeste. A presença de uma contracorrente costeira formada durante períodos de relaxamento do afloramento, que provavelmente transporta nutrientes das descargas fluviais e biomassa fitoplânctónica, pode ter também contribuído para o aumento de Chl-a na costa sul. Os modelos aditivos generalizados mistos, aplicados à Chl-a para cada região específica, exibiram uma melhor performance ($\geq$ 60% variância) em oceano aberto e em zonas diretamente influenciadas por descargas fluviais. De modo geral, as variáveis ambientais locais, como a temperatura da superfície do oceano, radiação fotossinteticamente ativa e a profundidade da camada de mistura, emergiram como os preditores mais influentes, enquanto

os indicadores climáticos de larga escala apresentaram efeitos secundários, menos significativos, destacando-se entre eles o AMO e EA.

As espécies de fitoplâncton potencialmente associadas ao síndrome ASP (*Pseudo-nitzschia* spp.) apresentaram um ciclo anual bimodal, para a maior parte das áreas de produção de bivalves, com o início dos florescimentos na primavera (mais tarde em relação à Chl-a), e com máximos relativos no final da primavera e verão, em resultado da diminuição da extensão da camada de mistura e aumento da disponibilidade de nutrientes fornecidos pelo afloramento costeiro, favorecendo, assim, as populações de diatomáceas. Pelo contrário, as espécies responsáveis pelos síndromes DSP (e.g., *Dinophysis* spp.) e PSP (e.g., *Gymnodinium catenatum*) exibiram um padrão unimodal, com o máximo de abundância no final do verão (assemelhando-se ao padrão de Chl-a nas regiões costeiras), perante situações de estratificação mais intensa entre pulsos de afloramento relativamente fraco ou subsidência da água superficial, que favorecem os dinoflagelados, e final da primavera, respetivamente. No entanto, o pico de espécies potencialmente produtoras de PSP, registado no final da Primavera, não é concordante com a maioria dos estudos que referem uma abundância máxima durante o outono. As espécies potencialmente produtoras de DSP e ASP foram responsáveis pela maioria dos eventos de florescimentos toxigénicos durante o período de estudo, sendo que as espécies associadas ao síndrome ASP atingiram abundâncias mais elevadas, provavelmente devido às elevadas taxas potenciais de crescimento *in situ* das diatomáceas. Os modelos GAM para espécies potencialmente produtoras de DSP apresentaram um poder preditivo superior (21% - 54% da variância) aos modelos associados a espécies produtoras de ASP (7% - 8% da variância). Para além dos preditores mais influentes referidos para a Chl-a, descargas fluviais elevadas associaram-se a abundâncias inferiores dos grupos produtores de ASP e DSP. Adicionalmente, o regime de convergência/contracorrente associou-se a abundâncias superiores de produtores de DSP, enquanto o regime de afloramento favoreceu a abundância de espécies produtoras de ASP apenas na zona produção sudeste (L9). Contrariamente ao esperado, a intensidade e persistência das condições de afloramento costeiro não foram considerados preditores da abundância de espécies produtoras de ASP na maior parte das áreas de produção, provavelmente devido à existência de um desfasamento temporal (*lag*) entre as condições favoráveis de afloramento costeiro e a resposta das diatomáceas. Futuros modelos de previsão aplicados à área de estudo deverão assim considerar os preditores mais influentes identificados pelos modelos GAM. Contudo, outras variáveis ambientais deverão também ser ponderados, tais como, a concentração de nutrientes inorgânicos dissolvidos, a turbulência e

os processos de mortalidade do fitoplâncton (ex.: predação). Trabalhos futuros poderão ainda contemplar a aplicação dos modelos GAM a diferentes estações do ano, a comparação do desempenho destes modelos com modelos híbridos e a investigação de eventos climáticos extremos. As previsões destes modelos poderão auxiliar na implementação de um sistema de alerta precoce de florescimentos de algas nocivas e no desenvolvimento de programas de gestão integrada dos ecossistemas costeiros mais eficientes.

Palavras-chave: variabilidade do fitoplâncton, fenologia do fitoplâncton, florescimentos de algas nocivas, fatores ambientais, regime hidrodinâmico, modelos aditivos generalizados

Table of Contents

List of Figures

List of Tables

List of Acronyms and Abbreviations

ADCP – Acoustic Doppler Current Profiler

AIC –Akaike Information Criterion

AMO – Atlantic Multidecadal Oscillation

APA – Agência Portuguesa do Ambiente

AR – Alcalá del Río

ASCAT – Advanced Scatterometer

ASP – Amnesic Shellfish Poisoning

AZP – Azaspiracid Shellfish Poisoning

BSW – Blended Sea Winds

CCC – Coastal Countercurrent

CCMAR – Centro de Ciências do Mar

CFP – Ciguatera Fish Poisoning

Chl-a – Chlorophyll-a

CIMA-UAlg – Centro de Investigação Marinha e Ambiental da Universidade do Algarve

CMS – Copernicus Marine Service

CO_2 – Carbon Dioxide

CSET – Cross-Shore Ekman transport

DA – Domoic Acid

DSP – Diarrhetic Shellfish Poisoning

EA – East Atlantic

EBUS – Eastern Boundary Upwelling Systems

ECSM – East Cape Santa Maria

EF – Eastward Flow

ENACW – Eastern North Atlantic Central Water

ENSO-MEI – Multivariate El Niño Southern Oscillation

ESA – European Space Agency

GAM – Generalized Additive Models

GAMM – Generalized Additive Mixed Models

Gdn – Guadiana

GoC – Gulf of Cádiz

HAB – Harmful Algal Bloom

HAEDAT – Harmful Algal Event Database

HY – Homoyesso- and Yessotoxins

HYCOM – Hybrid Coordinate Ocean Model

I0 – Light intensity at the surface

IBI – Iberian Biscay Irish regional seas

$\mathbf{I_m}$ – Mean PAR intensity in the mixed layer

IPC – Iberian Poleward Current

IPMA – Portuguese Institute of the Sea and Atmosphere

$\mathbf{K_{PAR}}$ – PAR light attenuation coefficient

LOD – Limit Of Detection

MERIS – Medium Resolution Imaging Spectrometer

MLD – Mixed Layer Depth

MODIS – Moderate resolution Imaging Spectroradiometer

$\mathbf{N_2}$ – Nitrogen

NAO – North Atlantic Oscillation

NB – Negative Binomial

NCAR – National Center for Atmospheric Research

NCEI-NOAA – National Centers for Environmental Information-National Oceanic and Atmospheric Administration

NOff – North Offshore

NSP – Neurotoxic Shellfish Poisoning

O_2 – Oxygen

OA – Okadaic Acid

OC-CCI – Ocean Colour Climate Change Initiative Group

Off – Offshore

PAR – Photosynthetically Available Radiation

PL – Pulo do Lobo

PSP – Paralytic Shellfish Poisoning

PSTs – Paralytic Shellfish Toxins

RL – Regulatory Limit

SAIH – Sistema Automático de Información Hidrológica

SC – South Coast

SeaWiFS – Sea-viewing Wide Field of View Sensor

SMA – Standardized Major Axis

SSlp – South Slope

SST – Sea Surface Temperature

STX – Saxitoxin

UI_{SST} – SST-based Upwelling Index

VIIRS – Visible Infrared Imaging Radiometer Suite

WC – West Coast

WCSM – West Cape Santa Maria

WeMO – Western Mediterranean Oscillation

WOff – West Offshore

ZI – Zero Inflated

1 Introduction

1.1 Phytoplankton and harmful algal blooms

Phytoplankton are the main primary producers in marine ecosystems and the source of approximately 50% of atmospheric O_2. Moreover, phytoplankton communities are major contributors to the drawdown of CO_2 from the atmosphere, sequestering 20-35% of the worldwide CO_2 emissions per year, while playing a key role in the production of organic matter to higher trophic levels (Tweddle et al., 2018). Among the 5000 species of living phytoplankton, 300 of those are associated with harmful algal blooms (HABs) that can cause water discoloration, and more than half of those are known to produce toxins (Hallegraeff, 2004). Considering toxin-producing species, 90% are flagellates, notably dinoflagellates (Smayda, 1997; Sildever et al., 2019). These organisms constitute a major part in the functioning of aquatic ecosystems and global climate, hence the importance of understanding the factors that control phytoplankton communities (Villamaña et al., 2019). Phytoplankton variability is regulated by distinct bottom-up (e.g., light, inorganic nutrients, turbulence) and top-down controls (e.g., grazing, viral lysis, programmed cell death, sinking, advection), that determine phytoplankton growth and loss rates, respectively (see Behrenfeld and Boss, 2018 and references therein), albeit physical processes are considered particularly relevant.

The term "bloom", applied to phytoplankton assemblages, is a condition intrinsically related with biomass accumulation, representing a transient event when intrinsic growth rates overcome losses (Behrenfeld and Boss, 2014). Nonetheless, the definition varies as certain species may also have significant harmful impacts at concentrations below bloom densities (e.g., *Dinophysis* spp., which can be harmful at $<10^3$ cells L^{-1}; Reguera et al., 2014). For nontoxic species, relative biomass is the most used criterion to establish bloom status, whereas for harmful species, mere presence or measurable toxin levels define a HAB occurrence (Smayda, 1997). Besides natural causes (e.g., storms, currents, climate change), phytoplankton growth and loss rates can also be driven by anthropogenically induced alterations (Barbosa et al., 2010). Humankind has contributed by transporting toxic species in ballast water, as well as by adding increasing quantities of industrial, agricultural and sewage effluents to coastal waters, which in turn create a more favourable nutrient environment for certain HAB species (Anderson, 2009; Glibert et al., 2018). Depending on the species, blooms may have different deleterious effects, such as oxygen depletion, decreased light availability, damage or clogging of invertebrate and fish gills, mortality of cultured fish and invertebrates or toxin accumulation

along the food web, eventually reaching humans (Hallegraeff, 2004; Anderson, 2009; see review by Shumway et al., 2018). In addition to ecological and human health problems, HABs can have serious economic impacts, due to fish mortality and closure of fishery grounds, negative influence on tourism, and additional costs on monitoring and public health (Hoagland et al., 2002; Hallegraeff, 2004; Anderson, 2009; Berdalet et al., 2016; Sildever et al., 2019).

Different human toxic syndromes associated with phycotoxins, i.e., toxins produced by phytoplankton, were recognised, including amnesic, diarrhetic, paralytic, neurotoxic and azaspiracid shellfish poisoning (ASP, DSP, PSP, NSP and AZP, respectively), and ciguatera fish poisoning (CFP). All these syndromes are associated with dinoflagellates, except for ASP, that is produced by diatoms such as *Pseudo-nitzschia* (Anderson, 2009; Silva et al., 2016). This pennate diatom was identified as the main source of domoic acid which bioaccumulates along the food web. Also, after the decline of surface diatom blooms, domoic acid may reverberate into benthic food webs (Costa et al., 2004, 2005). The symptoms range from gastrointestinal (nausea, vomiting, diarrhoea), to neurological (headaches, dizziness, disorientation, seizures, short-term memory loss, permanent brain damage), to death in some cases (Bates et al., 1989; James et al., 2010). In turn, the dinoflagellate genus *Dinophysis* produce lipophilic toxins (okadaic acid derivatives and pectenotoxins), that accumulate in the digestive gland of bivalve molluscs (hepatopancreas; James et al., 2010), causing a gastrointestinal syndrome, DSP, whose symptoms include diarrhoea followed by nausea, vomiting and abdominal cramps. *G. catenatum* produce saxitoxins, that accumulate in bivalve molluscs and sediments in the form of resting cysts. These toxins are linked to PSP syndrome, whose mild symptoms include a tingling sensation or numbness starting around the lips, in fingertips and toes, and gradually spreading. Severe intoxications induce headache, nausea, vomiting and diarrhoea with increasing muscular paralysis and pronounced respiratory difficulty (James et al., 2010). Other dinoflagellate groups, such as *Ostreopsis* and *Karenia*, can produce palytoxins and brevetoxins, two of the most potent neurotoxins of marine origin that have been related to serious human poisoning through aerosolization (Prince et al., 2010; Abdennadher et al., 2017). However, it is important to emphasize that shellfish contamination is not the result of a simple lineal process dependent on the abundance of toxin producers but of a complex balance from a chain of processes, including the toxin production, uptake, biotransformation, and elimination, that are species-specific and also depend on individual life stage and size (Reguera et al., 2014).

1.2 Phytoplankton dynamics and drivers

Several decades ago, relatively few countries were affected by HABs, but nowadays most countries are threatened, in many cases by more than one harmful or toxic species. This global expansion is, in part, a reflection of higher scientific awareness and improved detection methods that help to minimize impacts and protect public health and marine resources (Sildever et al., 2019). However, HAB problems are likely to be aggravated in an ever-changing world due to population growth, pollution, and climate change (Ralston and Moore, 2020). In fact, phytoplankton will be among the first to respond to changes in ocean conditions, as they have rapid generation times and short lifetimes (Litchman et al., 2015), and their distribution, survival and success depend on the physical and chemical properties of the water masses they inhabit (Trainer et al., 2020).

For more than half a century, several paradigms and hypotheses have been developed to explain the general mechanisms behind phytoplankton bloom initiation (see review by Behrenfeld and Boss, 2018). However, from the earliest critical depth hypothesis of Sverdrup in 1953, these premises have been under continuous scientific debate. The critical depth hypothesis is a bottom-up approach, based on abiotic drivers, that explains the timing of spring bloom initiation in temperate oceans by an increase in light availability, generated during the mixed layer shallowing period. Later, other hypotheses were suggested, still supported by bottom-up controls, namely the critical turbulence and the convection shutdown hypothesis. The most recent proposed explanation is the disturbance recovery-hypothesis that considers also biotic drivers (top-down controls; Behrenfeld and Boss, 2014). This hypothesis suggests that a disturbance factor, the increase in mixed layer depth, decreases phytoplankton grazing mortality, allowing phytoplankton biomass to increase, initiating a bloom during the mixed layer deepening period (see review by Behrenfeld and Boss, 2018). However, phytoplankton temporal variability patterns, bloom dynamics and phenology vary depending on the location and period, due to the prevalent ocean circulation patterns, atmosphere-land-ocean interactions, and biotic pressures (Cloern and Dufford, 2005; Longhurst, 2007).

1.2.1 Relevant physical processes

Phytoplankton blooms tend to form in waters enriched in nutrients by convective and wind-driven mixing, riverine inputs, or coastal upwelling (Behrenfeld and Boss, 2014). While, wind stress fluctuations and freshwater inputs control bloom intensity, timing and duration, inner-shelf dynamics regulate phytoplankton spatial distribution (Pitcher et al., 2010). The distribution of bloom events in the Eastern Boundary Upwelling Systems (EBUS: California,

Canary, Humboldt, and Benguela current systems), and their linkages to the physical environment, have been widely studied (see review by Pitcher et al., 2010). Wind-driven upwelling in EBUS supplies nutrients that support around 5% of global marine primary production (Carr, 2002) and 20% of worldwide fisheries (Chavez and Messié, 2009). The Iberia/Canary upwelling ecosystem, associated with the North Atlantic anticyclonic gyre (Wooster et al., 1976), is one of the most studied upwelling systems due to the large shellfish aquaculture industry in this region (Trainer et al., 2010). In particular, the Iberian Coast, located in the northern limit of this upwelling system, is of particular interest for management and environmental policymaking, as it covers a large area that makes up most of the EU Marine Strategy Framework Directive, subregion 'Bay of Biscay and the Iberian Coast' (Ferreira et al., 2019).

From a general perspective, the seasonal upwelling regime at the Iberian coast results from the evolution of the Azores high and the Iceland low pressure centres which determine the wind regime and the onset of an upwelling (spring-summer) and a downwelling season (autumn-winter), interspersed by mixed hydrodynamics conditions in spring and autumn (Díaz et al., 2019). Northerly winds from April to September cause an offshore Ekman transport of surface sea water along the Iberian west coast, and the upwelling of cold and nutrient rich subsurface Eastern North Atlantic Central Water (ENACW). This regime is followed by a shift during autumn, to southerly winds which favour downwelling conditions over the shelf, coinciding with the onset of a warm and saline poleward slope current, the Iberian Poleward Current (IPC). Along the Portuguese south coast, coastal upwelling events are triggered by strong westerly winds (Relvas and Barton, 2002). Frequently, during westerly wind relaxation, warm surface waters are carried westward along the south coast of Portugal, on occasion turning clockwise around Cape São Vicente to flow poleward along the west coast (Fiúza et al., 1982; Relvas and Barton, 2002). This westward counterflow is driven by an alongshore pressure gradient, whose effect is intensified or diminished by wind forcing. Other processes contributing to the nutrient pool include river discharge from large drainage basins along the coast (e.g., Tagus, Douro, Guadiana, Guadalquivir), especially when combined with rain events, and remineralization of benthic sediments (González-García et al., 2018; Ferreira et al., 2019).

1.2.2 Phytoplankton group-specific functional traits

In addition to the identification of relevant environmental drivers for phytoplankton, it is important to consider the functional traits characteristic of different phytoplankton groups, since these lead to different responses across environmental gradients, and changeable

temporal variability patterns. The major niche-defining phytoplankton traits include resource acquisition and utilization traits, grazer and parasite resistance traits, and various physiological traits affecting species persistence, namely structures and/or physiological processes associated with buoyancy control and motility (Glibert and Burford, 2017; see review by Weithoff and Beisner, 2019). HAB-forming species, in particular, are characterized by a wide set of plastic traits (e.g., nitrogen-N_2 fixation, mixotrophy) favouring their success in different environments (Litchman et al., 2010; Otero et al., 2018). Differences between diatoms and dinoflagellates are clearly recognized. Blooms of diatoms are typically related to turbulent, nutrient-rich conditions, common during upwelling events, transferring energy to higher trophic levels while vertically exporting organic matter to benthic systems (Barton et al., 2013). However, recent studies have recognized that diatoms are not strictly limited to the high-turbulence-high nutrient end of the spectrum, but have specific adaptations (e.g., grow in low light conditions at depth, mine nutrients from deeper regions, migrate to higher light levels, engage in symbioses with N_2-fixing cyanobacteria) that allow them to subsist and grow under stratified conditions (see Kemp and Villareal, 2018 and references therein). In turn, dinoflagellates reach highest abundance in relatively stratified and nutrient-depleted environments, common during summer upwelling relaxation stages, being associated with weaker vertical transport and retention of organic matter at the ocean surface (Glibert and Burford, 2017). These pelagic populations may act as seed banks, inoculating nearshore blooms during upwelling relaxation periods (Pitcher et al., 2017). Margalef (1978) formalized this view in what is commonly known as Margalef's Mandala, although some limitations were later recognized (Reynolds, 1987; Smayda and Reynolds, 2001; Glibert, 2016). For instance, the original mandala did not consider the whole phytoplankton assemblage (only microphytoplankton groups) and underestimated the importance of biological N_2 fixation, and the role of diatom-diazotroph symbiosis, phytoplankton thin layers, the effect of iron on planktonic productivity and mixotrophy (Villamaña et al., 2019). According with Smayda and Trainer (2010), diatom life cycles tend to exploit seeding opportunities, whereas dinoflagellates are more oriented towards survival. However, several climate change scenarios project a shift in dominance from diatoms to smaller flagellates (and potentially harmful species; e.g., Bopp et al., 2005; Leterme et al., 2008), thereby modifying ecosystem functions (i.e., reduction of carbon sequestration and transfer to higher trophic levels, alterations in nutrient cycling; Beaugrand, 2005; David et al., 2012; Trombetta et al., 2019), while others envision a scenario whereby increased ocean stratification may actually enhance overall diatom production and export (Kemp and Villareal, 2018). Hence, the need to contemplate functional and trait-based approaches to better

understand and predict when and why certain types of phytoplankton bloom under specific environmental conditions (Glibert, 2016; Weithoff and Beisner, 2019).

1.3 Dynamics of phytoplankton and harmful algal blooms off southern Portugal

During recent years, phytoplankton have been investigated along domains off southern Portugal, using in situ and remote-sensing sampling strategies. These studies have contributed to the understanding of phytoplankton biomass variability and phenology for the western and southern Portuguese coasts (e.g., Cristina et al., 2016; Krug et al., 2017, 2018; Ferreira et al., 2019, 2021; Santos et al., 2020), and species composition and size structure (e.g., Lorenzo et al., 2005; Mendes et al., 2011; Goela et al., 2014). Particularly, remote sensing is considered a powerful tool due to its extensive spatial and temporal coverage and low end-user cost and is currently acknowledged as the best option for observing coastal and oceanic blooms (at large scales), especially if supplemented with direct sampling that allows the quantification of HABs (Babin et al., 2008; Caballero et al., 2020). Chlorophyll variability patterns were also used for partitioning the area off southwest Iberia (Navarro and Ruiz, 2006; Krug et al., 2017; Ferreira et al., 2019). Some studies also revealed significant relationships between phytoplankton and specific environmental processes, such as riverine discharges (e.g., Moita et al., 2003; Prieto et al., 2009; Guerreiro et al., 2013; Krug et al., 2017) and coastal upwelling (e.g., Cravo et al., 2010; Pérez et al., 2010; Vidal et al., 2017). For instance, off northwest Portugal, physical processes and climate were considered the main drivers of phytoplankton variability, while over the southwest region, phytoplankton appeared to be more dependent on nutrient availability (Krug et al., 2018; Ferreira et al., 2019, 2021).

Despite the increasing number of studies focusing on phytoplankton, the number of publications specifically addressing dynamics of harmful phytoplankton groups is mostly focused on the northwest Portuguese coast (e.g., Moita et al., 2006, 2016; Díaz et al., 2016; Ruiz-Villarreal et al., 2016; Vidal et al., 2017; Díaz et al., 2019; Palenzuela et al., 2019), while off the south and southwest coasts of Portugal is still limited (Loureiro et al., 2005; Navarro et al., 2012; Pinto et al., 2016; Danchenko et al., 2019; Santos et al., 2019, 2020; Caballero et al., 2020).Three main toxigenic phytoplankton taxa, that threat human health after consumption of contaminated shellfish, have been referred for southern Portuguese coastal waters: *Pseudo-nitzschia*, *Dinophysis* spp. and *Gymnodinium catenatum* (e.g., Moita, 2001; Danchenko et al., 2019). More recently, other toxigenic taxa including benthic (*Ostreopsis*) and planktonic

dinoflagellates (*Karenia*, *Karlodinium*, *Azadinium*) have also been reported for the Portuguese southern coast (Danchenko et al., 2019; Santos et al., 2019). According with studies addressing the northwest Iberian coast, blooms of *Pseudo-nitzschia* are recurrent events during the spring-summer upwelling season, taking advantage of increased turbulence and higher nutrient levels (Palma et al., 2010; Mateus et al., 2013; Vidal et al., 2017). *Dinophysis* blooms are also more recurrent in northwest Iberia during the upwelling season (spring to early autumn), but are favoured during periods of thermohaline stratification, between moderate pulses of upwelling, and upwelling relaxation (autumn transition) that cause cross-shelf accumulation (Díaz et al., 2016, 2019; Vidal et al., 2017). For this area, blooms of *Gymnodinium catenatum* have been related with alongshore transport, at the end of the upwelling season, and weak currents or inshore eddies may contribute to the maintenance of this species near the coast (Moita et al., 2003, 2006; Díaz et al., 2019). In addition, *G. catenatum* forms cysts that germinate rapidly (within two weeks), allowing a nearly continuous transport of cells (Hallegraeff et al., 2012). For the southern Portuguese coast, few studies have documented the same seasonal patterns (Amorim et al., 2004; Loureiro et al., 2005; Mateus et al., 2013; Pinto et al., 2016; Danchenko et al., 2019; Santos et al., 2019), highlighting the need for further research in this area.

The generalized reported increase in HAB frequency (see review by Stauffer et al., 2019 and references therein), and the variable functional traits of different HAB-producers motivated the development of HAB forecasting models, based on empirical-statistical, deterministic numerical or hybrid approaches (see reviews by Rossini, 2014, and Ralston and Moore, 2020). Several predictive models were developed for northwestern Iberia (Palma et al., 2010; Moita et al., 2016; Díaz et al., 2016), but no modelling studies are currently available for HABs off the southern Portuguese coast.

1.4 Study objectives

In this context, the main goal of the current study was to characterize phytoplankton variability patterns and phenology in a complex marine domain, off southern Portugal, during a 6-year period (2014-2019), and identify underlying environmental determinants. The specific objectives of this study included: (i) the analysis of phytoplankton phenology, intra- and inter-annual variability patterns, and associated environmental drivers over specific regions of the study area (coastal, transition and oceanic domains); (ii) the analysis of intra- and inter-annual variability patterns, phenology, and associated environmental drivers for the most frequently reported toxigenic phytoplankton taxa in the study area, over different coastal bivalve production areas; (iii) the establishment of empirical statistical models linking phytoplankton

biomass and the abundance of key toxigenic taxa with critical environmental drivers; and (iv) the description of spatial-temporal variability patterns of phycotoxins in selected bivalve mollusk species, over different coastal bivalve production areas. Environmental determinants included large-scale climate indices, ocean currents, upwelling intensity, freshwater discharge, surface radiation, sea surface temperature, and mixed layer depth. Toxigenic phytoplankton taxa comprised two distinct groups (diatoms and dinoflagellates), with contrasting functional traits and environmental requirements. Based on previous studies (Pitcher et al., 2010; Behrenfeld et al., 2013; Reboreda et al., 2014; Díaz et al., 2016, 2019; Li et al., 2020), it was hypothesized that *Pseudo-nitzschia* blooms will be triggered under upwelling conditions, while *Dinophysis* spp. are more likely to be associated with downwelling/counterflow or mixed conditions. Hence, the physical oceanographic regime is expected to represent an important environmental predictor of both diatom and dinoflagellate blooms.

2 Materials and Methods

2.1 Study area

The study area, the domain off southern Portugal (35º to 38ºN and 12º to 5.8ºW; see Fig. 2.1), is located at the northernmost section of the Iberian Canary Eastern Boundary Upwelling system. This area, with a continental shelf ranging from 5 to 35 km width, encompasses complex marine domains influenced by different physical regimes (Garel et al., 2016; Relvas et al., 2007), and terrestrial nutrient inputs (e.g., Guadiana and Guadalquivir rivers; Caballero et al., 2014; submarine groundwater discharges; Hugman et al., 2015). Other fluvial contributions include the Mira estuary, Odeceixe, Aljezur and Bordeira streams, Arade estuary, and Alvor and Ria Formosa coastal lagoons (Krug et al., 2017). Mesoscale and sub-mesoscale features (e.g., upwelling filaments, fronts, cyclonic and anticyclonic eddies, jets, countercurrents) are also characteristic and often associated with topographic irregularities that affect local circulation patterns (Cape São Vicente, Cape Santa Maria, Cape Trafalgar; Peliz et al., 2004; García-Lafuente et al., 2006; García-Lafuente and Ruiz, 2007; Relvas et al., 2007).

Phytoplankton variability patterns, based on satellite retrieved surface chlorophyll-a (Chl-a), were investigated for different spatial domains based on a previous objective partition of the study area (Krug et al., 2017). Based on this study, the following five regions were considered (see Fig. 2.1A): three coastal regions, West Coast (WC), South Coast (SC), and Guadiana (Gdn); one intermediate region, South Slope (SSlp); and two oceanic regions, West Offshore (WOff), which includes part of Offshore (Off) and North Offshore (NOff) regions from the aforementioned partition, and a sub-region of Gulf of Cádiz (GoC). Variability of specific HAB taxa, based on *in-situ* abundance data, was investigated for five different coastal bivalve production areas (L6, L7a, L7c, L8 and L9), derived from ten sampling stations (from north to south and west to east: Sesimbra, Galapos, Comporta, Aljezur, Porto de Mós, Praia Dona Ana, Falésia, Praia de Faro, Culatra, and Monte Gordo; see Fig. 2.1B). Although, L6 area, that comprises three sampling points (Sesimbra, Galapos and Comporta), extends beyond the study domain. L7b was excluded from the analysis due to altered conditions associated with offshore marine fish-cage farming, whilst L7c1 and L7c2 areas were aggregated since these areas are part of the same coastal partition defined by Krug *et al.* (2017). Furthermore, two land-based hydrological stations (Pulo do Lobo and Alcalá del Río) were used for riverine flows. Current velocity and temperature data were measured using an Acoustic Doppler Current Profiler (ADCP) moored near Armona island (Latitude: 37º 00.648', Longitude: -7º 44.480'; see Fig. 2.1B).

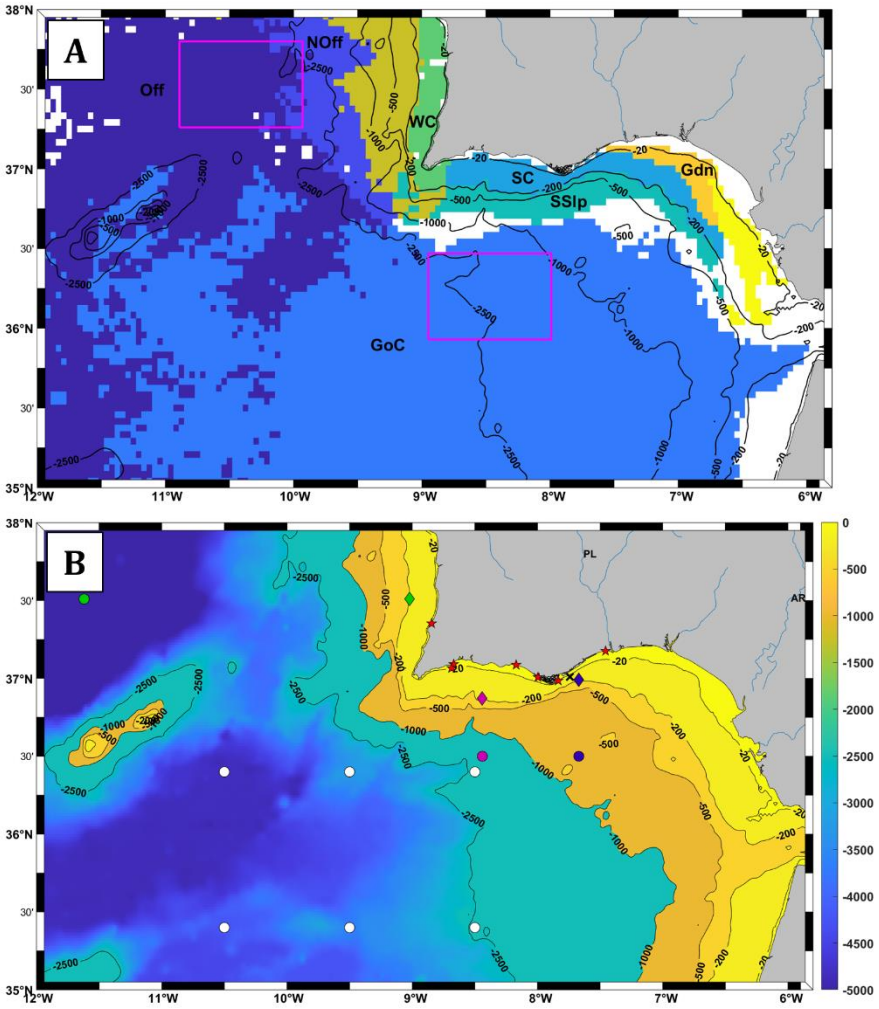

Figure 2.1 - A) Regions of interest with coherent, covarying chlorophyll-a variability patterns off southwest Iberia, previously defined by Krug *et al.* (2017): Offshore (Off), North Offshore (NOff), Gulf of Cádiz (GoC), South Slope (SSlp), West Coast (WC), South Coast (SC), and Guadiana (Gdn). Pink boxes mark two oceanic domains: West Offshore (WOff), which includes part of Off and NOff regions, and a sub-region of GoC; B) study area, off southern Portugal, with information on bathymetry and major estuarine systems. PL and AR depict the location of Pulo do Lobo and Alcalá del Río hydrographic stations, respectively. Diamonds and circles show the approximate positions used for the calculation of the upwelling indices (wind and temperature-based) for the West Coast (green), and west (pink) and east Cape Santa Maria sectors (blue). White circles identify three pairs of control points used to calculate the latitude effect on sea surface temperature. Black cross mark represents the Armona site where current velocities were measured, and red stars represent approximate positions of the Portuguese Institute of the Sea and Atmosphere sampling stations over the shellfish production areas L7a, L7c, L8 and L9 (from west to east: Aljezur, Porto de Mós, Praia Dona Ana, Falésia, Praia de Faro, Culatra, and Monte Gordo; see text for further details). L6 area was not included since it extends (northward) beyond the study area.

2.2 Environmental setting

A set of environmental drivers were acquired for the study period (2014-2019) from different sources: satellite remote sensing (wind speed and direction, Sea Surface Temperature-

SST, and Photosynthetically Available Radiation-PAR), model-based data (Mixed Layer Depth-MLD), *in situ* observations (Guadiana and Guadalquivir river discharges, abundance of HAB species, and biotoxin concentration in selected bivalve species), and large-scale climate indices (El Niño Southern Oscillation-ENSO, North Atlantic Oscillation-NAO, Atlantic Multidecadal Oscillation-AMO, East Atlantic pattern-EA, and Western Mediterranean Oscillation-WeMO) from a combination of different methods, with different spatial-temporal resolutions (see Table 2.1). Hence, whenever possible, variables were re-gridded to the same resolution.

2.2.1 Physical oceanographic variables

Level 3, 8-day composites of satellite-derived SST data were retrieved from MODerate resolution Imaging Spectroradiometer, MODIS-Aqua, available at NASA's Oceancolor database (http://oceancolor.gsfc.nasa.gov/; see Table 2.1), for the study period (2014-2019). SST data (at 4 km resolution) was limited to night-time passes, to avoid diurnal solar heating effects (Robinson, 2010), and high-quality data (AVHRR quality flags 6 and 7, and MODIS-A quality flag 0). SST 8-day mean values were averaged for each of the five study regions (WC, SC, Gdn, SSlp, WOff, and GoC; see Fig. 2.1A).

Daily MLD data, at ~ 0.083° spatial resolution, was acquired from the Iberian Biscay Irish regional seas (IBI) reanalysis database (Product ID: IBI_REANALYSIS_PHYS_005_002) provided by Copernicus Marine Service (CMS; https://marine.copernicus.eu/; see Table 2.1), and further adjusted to local bathymetry, with maximum values defined at 50 m from the coast. To estimate missing MLD data during year 2019, the best-fitting regression equations (N=1089, coefficient of determination (R^2) between 0.47 and 0.83, and p-values < 2.2e-^{16}) relating IBI REANALYSIS dataset with two additional products, Hybrid Coordinate Ocean Model (HYCOM) based on the 0.03 density contrast (that computes MLD as the depth at which the potential density changes by a fixed threshold value of 0.03 km m^{-3} relative to the one at a near-surface reference depth; ID: expt_91.0, expt_91.1 and expt_91.2) and IBI ANALYSIS (ID: IBI_ANALYSIS_FORECAST_PHYS_005_001), retrieved from Ocean Productivity (http://sites.science.oregonstate.edu/ocean.productivity/) and CMS, respectively, were applied to each region. After comparing the two products using the R-squared values, IBI ANALYSIS was considered a better fit to estimate the missing values. Daily MLD values were averaged over 8-day periods, within each study region.

Table 2.1 – Summary of physical, hydrographic, climatological and phytoplankton variables used in this study, and associated spatial and temporal resolution, and sources (see text for further details). CMS: Copernicus Marine Service, NCEI-NOAA: National Centers for Environmental Information-National Oceanic and Atmospheric Administration, CCMAR: Centro de Ciências do Mar, CIMA-UAlg: Centro de Investigação Marinha e Ambiental da Universidade do Algarve, IPMA: Portuguese Institute of the Sea and Atmosphere, APA: Agência Portuguesa do Ambiente, SAIH: Sistema Automático de Información Hidrológica, NCAR: National Center for Atmospheric Research, OC-CCI: Ocean Colour Climate Change Initiative Group, ENSO-MEI: Multivariate El Niño Southern Oscillation Index, NAO: North Atlantic Oscillation, AMO: Atlantic Multidecadal Oscillation, EA: East Atlantic pattern, WeMO: Western Mediterranean Oscillation. *8-day mean values.

	Variables	Spatial resolution	Temporal resolution	Source
Physical	SST	4 km	ca. Weekly*	OceanColor Link: http://oceancolor.gsfc.nasa.gov/
	PAR	1 km	ca.Weekly*	OceanColor
	MLD	0.083°	Daily	CMS Link: https://marine.copernicus.eu/
	Zonal (U) and meridional (V) winds	0.25°	Daily	NCEI-NOAA Link: https://www.ncdc.noaa.gov/data-access/marineocean-data/blended-global/blended-sea-winds
	Alongshore (u) and cross-shore (v) current velocities	37º 00.648', -7º 44.480'	Hourly	CCMAR/CIMA-UAlg/IPMA (data access provided by Dr. Erwan Garel)
Hydrographic and climatological	Guadiana and Guadalquivir river discharges	37º 48.18', -7º 37.98' (Pulo do Lobo); 37º 31.11', -11º	Daily	SNIRH, APA (http://snirh.apambiente.pt/), SAIH del Guadalquivir (http://www.chguadalquivir.es/saih/)

		58.57’ (Alcalá del Rio)		
	Large-scale climate indices (ENSO-MEI, NAO, AMO, EA, WeMO)	-	Monthly	NOAA, NCAR, University of Barcelona's Climatology Group Links: https://www.psl.noaa.gov/data/climateindices/; https://www.cpc.ncep.noaa.gov/; https://climatedataguide.ucar.edu/climate-data; http://www.ub.edu/gc/wemo/
Phytoplankton	Chlorophyll-*a*	4 km	ca. Weekly*	OC-CCI Link: https://www.oceancolour.org/
	Abundance of harmful algal bloom taxa	-	ca. Weekly	IPMA public database Link: https://www.ipma.pt/pt/index.html/
	Biotoxins in shellfish species	-	ca. Weekly	

Weekly (8-day) level-3 mean surface PAR data, at 1 km spatial resolution, from MODIS-Aqua were also assessed from NASA's Oceancolor Group (Table 2.1). Light attenuation coefficient at 490 nm wavelength (K_{490}, m^{-1}), obtained from OC-CCI, was converted to PAR light attenuation coefficient (K_{PAR}, m^{-1}) using Eq. (1), following Rochford et al. (2001). Mean PAR intensity in the mixed layer (I_m, µmol photons m^{-2} s^{-1}) was calculated using Eq. (2), according to Kirk (1986), where I0 represents PAR intensity at the surface (µmol photons m^{-2} s^{-1}), K_{PAR} is the PAR light attenuation coefficient (m^{-1}), and MLD corresponds to the mixed layer depth (m). The resultant values were averaged over each region (WC, SC, Gdn, SSlp, WOff, and GoC; see Fig. 2.1A).

$$K_{PAR} = 0.085 + 1.6243K_{490} \quad \text{Eq.1}$$

$$I_m = I0\frac{(1 - e^{-K_{PAR}\,MLD})}{K_{PAR}\,MLD} \quad \text{Eq.2}$$

Daily sea surface zonal (U) and meridional (V) wind fields, at 0.25º spatial resolution, were obtained from the Blended Sea Winds dataset (BSW) available at NCEI-NOAA (https://www.ncdc.noaa.gov/data-access/marineocean-data/blended-global/blended-sea-winds; see Table 2.1). Blended Sea Winds are based on a combination of several scatterometers and standardized across platforms, resulting in high quality ocean wind vectors (Zhang et al., 2006). Additionally, daily Advanced Scatterometer (ASCAT)-B wind data, at ~ 0.25º spatial resolution, in both descending and ascending modes, were retrieved from the Global Ocean L3 Wind Product available through CMS, and compared with Blended Sea Winds using regression analysis (N=751, R^2 between 0.54 and 0.61, and p-values between $9.47e^{-157}$ and $5.87e^{-130}$ for the south coast, and N=809, R^2=0.59, and p-value=$3.88e^{-156}$ for the west coast), for estimation of missing wind data for the year 2019.

Upwelling intensity was estimated using two indices: an SST-based index (UI_{SST}), and a wind-based index (cross-shore Ekman transport, CSET). Wind data were used to calculate CSET (Bakun, 1973; Alvarez et al., 2011). CSET represents the magnitude of the offshore component of Ekman transport, which roughly compares to the amount of water upwelled from the base of the Ekman layer (Bograd et al., 2009). This index was computed for three specific points (see Fig. 2.1B): one located at ~ 20km off the west Portuguese coast ($CSET_{WC}$), and two located on the south Portuguese coast, at western and eastern sectors of Cape Santa Maria,

located at 24 km and 11 km from the coastline, respectively ($CSET_{wCSM}$ and $CSET_{eCSM}$). This method was based on the average of as many adjacent pixels as possible, depending on distance from the coast. For the western coast, the average of nine pixels was considered, whereas for the southeastern coast, only six pixels were considered. The orientation of the south and west Portuguese coastlines (zonally and meridionally, respectively) affected CSET calculation. For the south coast, the meridional component (y) of the Ekman transport, $CSET_y$, induced by the zonal component of wind-stress, was used as upwelling index (τx; see Eq. 3). In contrast, the wind-based upwelling index over the west coast was obtained through the zonal (x) component of the Ekman transport, $CSET_x$, induced by the meridional component of wind stress (τy; Eq. 4). The following equations were considered:

$$CSETy = -\frac{1000\tau x}{\rho W f} = -\frac{\rho_a C_d}{\rho_W f}\left(W_x^2 + W_y^2\right)^{\frac{1}{2}} 1000 W_x \quad \text{Eq. 3}$$

$$CSETx = \frac{1000\tau y}{\rho W f} = \frac{\rho_a C_d}{\rho_W f}\left(W_x^2 + W_y^2\right)^{\frac{1}{2}} 1000 W_y \quad \text{Eq. 4}$$

where W represents wind magnitude (m s^{-1}), ρ_w is seawater density (1025 kg m^{-3}), ρ_a is air density (1.22 kg m^{-3}), C_d is the drag coefficient (1.4×10^{-3}), and f is the Coriolis parameter ($f = 2\ \Omega\sin(\theta)$, where Ω and θ correspond to the Earth's angular velocity and latitude, respectively). Negative values of the upwelling index indicate offshore Ekman transport and thus upwelling-favourable conditions, whereas positive values represent onshore Ekman transport and downwelling-favourable conditions (Bakun, 1973; Alvarez et al., 2011). The wind-based upwelling index was used to infer the physical regime for the west and south-western Portuguese coasts.

The UI_{SST} was calculated as the difference between SST at oceanic and coastal points, located at the same latitude (western coast) or longitude (southern coast) For each point, an SST value was computed as the average of all adjacent pixels available (maximum: 9 pixels). Off the western coast, a pair of points was considered at 20 km and 250 km from the coast. The latter was positioned according with general spatio-temporal variability patterns of this index, that remain similar within the range 400-1000 km offshore (Nykjaer and Van Camp, 1994; Santos et al., 2005; deCastro et al., 2008), adjusted to the current spatial domain (i.e., reducing the distance from the coast to ~250 km). Along the southern coast, two pairs of points were placed at 24-65 km and 11-64 km from the coast (see Fig. 2.1B). Since no upwelling filaments are usually referred off the south coast (except at Cape São Vicente; Haynes et al., 1993), the

distance between points was relatively reduced in respect with the west coast. Nonetheless, the difference between oceanic and coastal points at the south coast cannot be considered as an absolute upwelling index since temperature also changes with latitude, due to differences in solar heating. To minimize the influence of latitudinal changes in SST, a previous analysis was performed, following Alvarez *et al.* (2011). Three pairs of control points were considered along 36.4ºN and 35.4ºN latitude, spanning from 8.5^{O}W to 10.5^{O}W longitude (east, central, and west control points; see Fig. 2.1B). SST difference was calculated between each pair of points, located at the same longitude, and then averaged. The results showed that SST values increased southward, at a rate of 0.54 ºC ºlatitude^{-1}. Then, when estimating UI_{SST}, the SST values of the two oceanic points were corrected considering this value, and the difference between ocean and coastal waters was calculated. Positive (negative) UI_{SST} values mean upwelling favorable (unfavorable) conditions (Alvarez et al., 2011). Both upwelling indices were averaged over an 8-day period, for the three locations (WC, wCSM and eCSM).

Additionally, over the south-eastern Portuguese coast, v and u current velocities and SST data, measured at Armona site (23 m depth level; see Fig. 2.1B) using an ADCP, with a high temporal resolution (1-4 hours), were provided by Dr. Erwan Garel, from 'Centro de Investigação Marinha e Ambiental da Universidade do Algarve' (CIMA-UAlg; Table 2.1). A Butterworth filter of 40 hours was used to remove high frequency oscillations in current and SST data (e.g., tides). Then, for this coastal area, the predominant oceanographic physical regime was also inferred from the current velocity information at Armona site, and local SST information (see Garel et al., 2016). A threshold criterion, of at least seven consecutive days of negative (positive) current velocities, was used to identify countercurrent (upwelling) conditions at the south-eastern coast, associated with westward (eastward) flows along the south coast. This criterion was based on a previous study of the periodic components of the upwelling index off the western Iberian margin, that defined an upwelling cycle in about seven days (Palma et al., 2010). Periods when this criterion was not met were classified under a mixed physical regime.

2.2.2 Hydrographic and climatological variables

Guadalquivir river discharge, measured at the Alcalá del Río station during the period 2014-2019 (daily resolution), was acquired from the Spanish Regional Water Management Agency (http://www.chguadalquivir.es/saih/). Guadiana river discharge, measured at the hydrometric station Pulo do Lobo, at daily resolution, during the same period, was accessed from the Portuguese Environmental Agency public database (http://snirh.apambiente.pt/).

A total of five large-scale climate indices (monthly data) were used as indicators of wide-atmospheric forcing over the study area: Multivariate El Niño Southern Oscillation (ENSO) Index (MEI), North Atlantic Oscillation (NAO) index, Atlantic Multidecadal Oscillation (AMO) index, East Atlantic pattern (EA) index, and Western Mediterranean Oscillation (WeMO) index. MEI and AMO data were retrieved from NOAA's Earth System Research Laboratory portal (https://www.psl.noaa.gov/data/climateindices/), EA data were available at NOAA's Climate Prediction Center website (https://www.cpc.ncep.noaa.gov/), NAO were acquired from the (USA) NCAR website (https://climatedataguide.ucar.edu/climate-data), and WeMO data from the University of Barcelona's Climatology Group website (http://www.ub.edu/gc/wemo/).

2.3 Phytoplankton data

2.3.1 Chlorophyll-a

Satellite-derived surface Chl-a, used as a proxy for total phytoplankton biomass, was retrieved from the European Space Agency (ESA)'s OC-CCI group (https://www.oceancolour.org/; see Table 2.1). The OC-CCI Chl-a product combines information from several sensors (Sea-viewing Wide Field of View Sensor - SeaWiFS, MODISAqua, Medium Resolution Imaging Spectrometer - MERIS, and Visible Infrared Imaging Radiometer Suite - VIIRS), enabling an increased spatial-temporal resolution data (Sathyendranath et al., 2019). Level 3, 8-day composites of satellite-derived Chl-a, at 4 km resolution, were averaged during the period 2014-2019 for each coastal (WC, SC, and Gdn), intermediate (SSlp), and oceanic regions (WOff, and GoC; see Fig. 2.1A).

2.3.2 Harmful algal blooms

In Portugal, the Portuguese Institute of the Sea and Atmosphere (IPMA) is the entity responsible for managing bivalve production zones and keeping the national phytoplankton and biotoxin monitoring databases updated (Oliveira et al., 2015). IPMA monitoring program include the analyses of phytoplankton in different estuarine and coastal shellfish production areas, and uses two regulatory abundance levels for specific phytoplankton toxin-producing genera/species (see Annex A.1; IPMA, 2021): alert level (imposes an increase in sampling frequency but allows bivalve harvesting), and interdiction level (imposes closure of bivalve harvesting, independently on phycotoxin levels). Abundance of different HAB species (see Annex A.2), measured approximately weekly at different sampling stations (see Fig. 2.1B), integrated into five coastal shellfish production areas (L6, L7a, L7c, L8, L9), was obtained from IPMA public database (http://www.ipma.pt/pt/index.html/). IPMA sampling stations

were defined with an effort to ensure that results were representative of the corresponding coastal bivalve production areas (https://www.ipma.pt/pt/bivalves/docs/index.jsp). However, since IPMA database included reference to the specific stations, within each production area, only for a limited period (available for January-October 2014), all data for each production area were combined, independently on the sampling station. Monthly sampling effort, for each production area, was calculated as the proportion of HAB processed samples evaluated each month in respect with total number of HAB samples, considering specific years and the global dataset. L7c and L6 production areas were the most consistently assessed areas for HAB abundance data (with a maximum of 161 and 129 processed samples, respectively). However, considering the monthly sampling effort per year, HAB processed samples only represented up to ~14% and 12% of the yearly sampling (specifically, of 2014), at L7c and L6, respectively.

HAB abundance classified as below the limit of detection (LOD) or 'ND' (undetected) in the IPMA public database were considered as zero. Other data descriptions including 'NDi' (unavailable), 'NR' (unfulfilled), and 'NQ' (unquantified) were not considered. Multiple samples collected during the same day for each production area were averaged. As the information on species-specific abundance at the public database was available only between January - October 2014, the abundance of all HAB groups potentially associated with each human syndrome (ASP, DSP, PSP, NSP and AZP), was represented by the summation of all group-representative species and genus (see Annex A.2). NSP and AZP toxin-producing dinoflagellates were not included due to the reduced extent of available data. Ciguatoxin and palytoxin producing dinoflagellates were not accounted as only 'NR' or '0' values were reported.

According with information available at the Harmful Algal Event Database (HAEDAT; http://haedat.iode.org), during the period 2014-2019, a total of 72 bloom events of *Dinophysis acuminata* (associated with DSP syndrome) were registered along the Portuguese coast, of which 11 events occurred within the study area. No *D. acuta* blooms were reported during the same period in coastal Portuguese waters. For *Pseudo-nitzschia* spp., 13 bloom events potentially responsible for ASP syndrome were registered for the Portuguese coast, but none in the study area. In the case of *Gymnodinium catenatum* (responsible for PSP syndrome), a total of 15 bloom events were detected for Portugal, and three occurred over southwest Portuguese coastal areas.

2.3.3 Phytoplankton phenology

Phytoplankton phenology was assessed using Chl-a, a proxy for phytoplankton biomass, over the six spatial domains defined over coastal, slope, and oceanic regions. Additionally, phenological patterns were also investigated using abundance data from the most frequently reported toxin-producing phytoplankton groups in the study area (ASP, DSP, and PSP).

In this study, bloom events were defined as occurrences characterized by a Chl-a or phytoplankton abundance (HABs) that exceeded the threshold criterion of 5% above the annual local median value, at least during two consecutive weeks (Siegel et al., 2002). This threshold is frequently used in phytoplankton phenology studies (Ferreira et al., 2014; see Krug et al., 2018 and references therein). The following phenological indices were estimated for each region, considering all bloom events (primary, associated with the maximum Chl-a concentration in each year, and secondary, with Chl-a concentration maxima lower than primary bloom), for each annual cycle: (1) number of bloom events; (2) average duration of bloom events; (3) total duration of all bloom events per year; (4) Chl-a or HAB abundance peak value; (5) principal bloom initiation timing (i.e., first week when Chl-a or HAB abundance surpassed the threshold criterion); (6) principal bloom peak timing, for Chl-a and HAB abundance (week of Chl-a or HAB group peak value, for each primary bloom event); (7) principal bloom termination timing (last week of Chl-a or HAB abundance above the threshold criterion); (8) bloom duration (time interval between bloom initiation and termination); (9) duration of the bloom accumulation phase (time interval between bloom initiation and peak); and (10) duration of the bloom deceleration phase (time interval between bloom peak and termination). Whenever the duration of the bloom accumulation or deceleration phase, in weeks $year^{-1}$, was zero, the exact number of days from the threshold value until reaching the maximum Chl-a concentration (or vice-versa) was calculated.

Based on documented phytoplankton seasonal variability patterns for the study area (Krug et al., 2017), Chl-a time series were organized considering the starting point of the annual cycle as the first week of September (week 1) and the end point as the last week of August (week 46), spanning two years. For the abundance of specific HAB groups, the beginning of the annual cycle was associated to the first week of January (week 1), ending during the last week of December (week 46), since most HAB blooms for the study area develop between spring and autumn (Goela et al., 2014; Danchenko et al., 2019).

2.4 Phycotoxins in bivalve molluscs

IPMA is the entity also responsible for monitoring bivalve toxicity through surveillance of toxin levels accumulated in their tissues (Vale et al., 2008). Toxic events are typically identified when bivalve toxicity values surpass the corresponding regulatory limit (RL; see Annex A.3). When shellfish tissue samples exceed the RL, harvesting of shellfish resources are closed until toxicity of two consecutive samples, taken from the same sampling point, is below that threshold, as prescribed by the European Regulation (Regulation EC, 2004). Phytoplankton toxin concentrations in recurrently surveyed bivalve species (*Mytilus* spp. and *Donax trunculus*), sampled, ca. weekly, at different sampling stations included into five coastal shellfish production areas (L6, L7a, L7c, L8, L9), were collected from IPMA public database (http://www.ipma.pt/pt/index.html/; see Annex A.4). For L7a and L9 areas, available information was restricted to *Mytilus* spp. and *Donax trunculus*, respectively. Toxin data for the year 2014 were excluded from further analysis due to the unusual stability of the reported values. As for HAB abundance, the monthly sampling effort, considering specific years and the global dataset, was calculated for each bivalve species. L7c and L8 were the most frequently evaluated production areas for bivalve toxins. The mussel *Mytilus* spp. and the wedge clam *Donax trunculus* were the most repeatedly analysed taxa at L7c and L8, with up to 134 and 89 processed samples, respectively. Monthly sampling efforts of approximately 100% were achieved at these production areas, in 2019 and 2017, respectively (data not shown).

The same procedures used for the abundance of HAB taxa were applied to unusual data descriptions of biotoxin data. Moreover, following Rao *et al.* (1991), and assuming that data was non normally distributed, data reported with as less than/less than or equal to a specific value ($<a$ or $\leq a$) were replaced by the square root of that value ($\sqrt{a}$), whereas values greater than/greater than or equal ($>a$ or $\geq a$) to were replaced by the specific value (a).

2.5 Data analysis

2.5.1 Non-parametric exploratory analysis

Intra- and interannual phytoplankton patterns and linkages with environmental drivers were investigated for both region-specific Chl-a and specific HAB groups. Normality tests (Lilliefors test, QQ plots, Shapiro-Wilks test) were applied to all variables to check for statistical assumptions underlying parametric tests (normality, homogeneity of variance and independence of errors). Since these conditions were not satisfied, non-parametric methods were used. Differences in physical oceanographic variables and phytoplankton (Chl-a, HAB

abundance, phenology indices) among spatial domains (regions or shellfish production areas) and physical oceanographic regimes were analyzed using the Kruskal-Wallis test, a one-way analysis of variance on ranks, followed by multiple pair-wise comparisons using the Dunn's test (Dunn, 1961). This strategy was also used for comparing specific phenological indices among and within HAB taxa. The influence of the physical oceanographic regime on region-specific Chl-a, HAB abundance, and biotoxins was evaluated using data binned into three main regimes: upwelling-favourable, downwelling or counterflow-favourable, and mixed regime (see section 2.2.1). For each region (Chl-a) or coastal bivalve production area (HAB), differences in Chl-a, HAB abundance, and bivalve biotoxins between seasons were analyzed considering four different periods, spring (April-June), summer (July-September), autumn (October-December), and winter (January-March), as well as the above-mentioned physical regimes. For this analysis, physical oceanographic regimes were defined using either CSET or along-shore current velocity data, depending on the region or production area. The use of UI_{SST} as an upwelling index was excluded due to its lower temporal resolution (weekly) in comparison with the other methods (hourly or daily resolution). Spearman correlation was used to evaluate the strength of monotonic relationships between HAB abundance and toxin concentrations. All statistical tests were considered at a 0.05 significance level.

2.5.2 Generalized additive models

Generalized Additive Models (GAMs) were developed, for each specific region and phytoplankton group, to identify the most significant environmental predictors of Chl-a and key toxigenic taxa (DSP and ASP). GAMs are considered empirical-statistical models, attempting to fit non-linear relationships between a dependent response variable and multiple predictors (independent variables; Wood, 2006). Since GAMs do not assume a particular type of response function, they are considered an effective modeling approach for assessing the responses of plankton communities to environmental factors (e.g., Irwin and Finkel, 2008; Llope et al., 2009; Otto et al., 2014). To develop these models, a family distribution needs to be specified for the dependent variable, along with a link function to relate the mean of the response variable to a smoothed function of the explanatory variables (Hastie and Tibshirani, 1990). The smooth functions are linear combinations of a finite number of cubic-spline basis functions, with the smoothness estimated by minimizing the generalized cross-validation criterion (Wood, 2000) that balances the goodness-of-fit and the smoothness of the functions. The basic GAM model structure as follows (Eq. 5):

$$Y = \propto + \sum_{j=1}^{n} s_j(X_j) + \varepsilon \qquad \text{Eq. 5}$$

where Y represents the response variable, $\propto$ is the intercept, s_j are nonparametric smoothing functions specifying the partial additive effects of each predictor (X_j), and ε is a random error term assumed to be normally distributed with zero mean and finite constant variance (Wood, 2006).

GAM response variables were region-specific Chl-a (8-day mean), and abundance of phytoplankton associated with DSP and ASP syndromes. Only Chl-a was log10-transformed to reduce over-dispersion and the influence of outliers. Predictor variables (Xi) included atmospheric and oceanographic variables, representative of the local study area or its regions (SST, PAR, MLD, CSET, alongshore velocity, Guadiana, and Guadalquivir discharges), as well as large-scale climate indices (AMO, EA, MEI, NAO, and WeMO). The latter were not considered from predictive models applied to HABs. For region-specific Chl-a models, Chl-a, SST, and PAR were averaged for each of the six defined regions (WOff, GoC, SSlp, WC, SC, Gdn; see Fig. 2.1A), and the only predictor variable available with a daily resolution (MLD) was averaged over 8-day periods. For HAB models, a total of four GAM models were developed for each HAB group (DSP and ASP), applied to different individual or aggregated coastal shellfish production areas: L6, L7a, L7c-L8, and L9. Predictor variables available daily (CSET) were averaged over a 5-day period prior to each sampling date (including the sampling day), and weekly values compatible with the sampling time were considered for other predictor variables (Chl-a, SST, PAR, MLD). For satellite-derived predictors, values from the nearest coastal region to the sampling point of each production zone were used, i.e., WC measurements for L6 and L7a, SC for L7c-L8, and Gdn for L9. For L7c-L8 production areas, $CSET_{wCSM}$ and $CSET_{eCSM}$ were averaged (resulting in a new variable, $CSET_{SC}$) as the difference between these two variables was non-significant (Z-statistic value=13.98, n=274, p=0.245).

For Chl-a models, Gaussian fitting with identity link was adopted, while the type of distribution and link function for each HAB group were tested to achieve the best models (Zuur et al., 2009; Zuur, 2012). The analysis of data frequency distribution, based on histograms, indicated that HAB abundance data were unimodal and right skewed, for both groups (DSP and ASP) and all areas (L6, L7a, L7c-L8), with skewness ranging from 4.84 to 25.26. The right tail of the distribution included a relatively small number of samples with high phytoplankton

abundances. As QQ plots and Shapiro-Wilks test further showed that the data did not follow a normal distribution (Shapiro test: W-statistic values between 0.03 and 0.48, p-values < $2.2e^{-16}$), alternative distributions were investigated. Firstly, a Poisson distribution with a log link function was used for model fitting of HAB abundance data. After attaining the best model using the Poisson distribution, the amount of overdispersion in the abundance data set was calculated as the sum of squared Pearson residuals divided by sample size minus the number of parameters (Hilbe, 2011; Zuur, 2012). As recommended by Zuur *et al.* (2009), for low overdispersion (above 1.5) a quasi' correction was applied, whereas with high overdispersion (above 15 or 20), alternative distribution methods were tested (Negative Binomial or Zero-Inflated/Hurdle models). Hence, a Negative Binomial (NB) distribution with a log link function was applied, followed by the analysis of overdispersion. If there was still overdispersion, zero-inflated (ZI) models were tested with a Poisson or NB distribution (depending on previous results), and the best-fitting distribution and link terms were determined. For both DSP and ASP groups, the most suitable distribution was the NB with a log link function, since it minimized overdispersion to acceptable levels (0 – 1). Nonetheless, the presence of a small amount of overdispersion (between 1.5 and 2.5) after fitting the NB distribution to DSP data from two regions (L6 and L7c-L8) suggested that ZI models should be considered. Yet, ZI-based models did not converge.

Prior to model testing, collinearity between covariates was verified using Spearman rank correlation coefficients (r_s), and a value equal to or less than 0.7 was considered a cut-off for inclusion of covariates in the same model run (Dormann et al., 2013; see Table A.1-A.3). Most predictor variables were moderately correlated ($|r_s|<0.50$). However, correlation values between PAR, I_m, and MLD, and $CSET_{WCSM}$ and $CSET_{ECSM}$ were consistently higher than 0.7 (see Appendix A.1), and these covariates were included in different competitive models. Hence, three approaches were applied to reach the optimal GAM models. Firstly, SST and PAR were tested in the same model, then SST with MLD, and lastly, MLD without SST (since SST and MLD showed a correlation close to the threshold, between 0.52 and 0.67). For HAB models, Chl-a and SST, and PAR and MLD could not be used as covariates for the same model run (Appendices A.2 and A.3). The resultant Chl-a models were fitted using a backward stepwise process in which non-significant covariates ($p > 0.05$) were removed until all terms were statistically significant, as proposed by Wood and Augustin (2002). Conversely, a forward selection approach was followed with HAB models, as suggested by Zuur *et al.* (2009),

evaluating the contribution of each predictor variable through the percentage of deviance explained and Akaike Information Criterion (AIC) value.

Overall, the criteria used to identify the best-performing models, selected from a combination of those used in previous GAM-based studies, included: (1) high R-square (R^2) and deviance values (R^2x100), (2) low AIC scores, (3) statistically significant (p-value < 0.05) relationships between individual predictors and the response variable, and (4) the confidence envelops for the smoothing should not include zero throughout the covariate range (Wood, 2006; Zarauz et al., 2007; Llope et al., 2009). The model with the lowest AIC score, and the highest deviance explained was selected as the fit that best described the variation in the response variable (Chl-a, and abundances of DSP and ASP).

Underlying statistical assumptions (residuals normality, homoscedasticity) of GAMs were tested using visual inspection of graphical residual diagnostics (including quantile-quantile plots, histogram of residuals, and residuals versus predictors plots). Model residues were tested for temporal autocorrelation using autocorrelation and partial autocorrelation functions (acf and pacf). As results showed lag-1 partial autocorrelations in all cases, when possible, GAMs were extended to Generalized Additive Mixed Models (GAMM) by including a first order autoregressive correlation structure (ARMA) in the models (e.g., Thackeray et al., 2008; Otto et al., 2014). Some of these models also displayed partial autocorrelation for higher-order lags (up to 18), however, they did not converge or showed a worse performance.

Additionally, GAMs were used to decompose region-specific time series of CSET, along-shore current velocity, Chl-a and HAB abundance into intra-annual and interannual components, thus contributing to identify distinct circulation and phytoplankton variability patterns. The variables year and month (zero-centered in decimal form) were added to the original dataset, and response variables were modelled as a cyclic spline smoother function of month, and a cubic spline smoother function of year, using a first order autoregressive correlation structure to deal with temporal autocorrelation. However, some models failed to converge not allowing for autocorrelation correction. In those cases, the corresponding GAM model was selected. GAM and GAMM analyses were conducted using the package ‘mixed GAM computation vehicle’ (mgcv), specifically the ‘gam’ function, in R statistical software version 4.0.3 (R Core Team, 2020), while the remaining graphical representations were generated in MATLAB 9.8.0.1380330 (R2020a) software (in-house scripts). It is worth mentioning that validation of GAM models was outside the scope of the present study.

3 Results

3.1 Environmental setting

3.1.1 Physical oceanographic variables

Basic statistical information from different regions off southern Portugal, including average, standard-deviation, minimum and maximum values, is summarized in Table 3.1. Considering the complete dataset, highly significant differences were detected between regions for most variables. SST and I0 attained higher mean values over the regions off the south Portuguese coast (see Table 3.1). Deeper MLD were detected in oceanic areas, although, significant differences were found across all domains (coastal, specifically WC and Gdn, intermediate and oceanic; $p < 0.05$; Fig. 3.1B). K_{PAR} showed an increase towards coastal regions, and higher I_m was observed over coastal and slope regions off south Portugal (Table 3.1). No significant differences were observed in I_m between the WC, WOff and GoC regions, or SC, SSlp and Gdn regions ($p < 0.05$; Fig. 3.1A). Both CSET and UI_{SST} revealed higher upwelling intensity over the west coast (WC) in comparison with the south-eastern coast (ECSM; $p < 0.05$; Fig. 3.1C-D). Moreover, UI_{SST} showed significant differences along the south coast, with higher upwelling intensity at west (WCSM) in respect with east Cape Santa Maria (ECSM; $p < 0.05$; Fig. 3.1D).

Table 3.1 – General statistical information, including mean, standard deviation (SD), minimum (Min) and maximum (Max) values, and number of samples (N), for physical (Sea Surface Temperature – SST, Light intensity at the surface – I0, Photosynthetically Available Radiation (PAR) light attenuation coefficient - K_{PAR}, mean PAR intensity in the mixed layer - I_m, Mixed Layer Depth – MLD, Cross-Shore Ekman Transport – CSET, and SST-based Upwelling Index - UI_{SST}), hydrographic and climatological variables (El Niño Southern Oscillation - ENSO, North Atlantic Oscillation - NAO, Atlantic Multidecadal Oscillation - AMO, East Atlantic pattern - EA, and Western Mediterranean Oscillation index - WeMO) measured in different regions off southern Portugal, during the period 2014-2019. NV: Not Valid, PL, and AR: Pulo do Lobo and Alcalá del Río hydrometric stations. See Figure 2.1 for location of regions. N corresponds to the number of exact (SST, PAR, K_{PAR}) or averaged measurements (I_m, MLD, CSET, UI_{SST}, Along-shore current velocity, river discharges, large-climate indices) for each region.

Variable	Region	Mean	SD	Min	Max	N
SST (°C)	WOff	18.0	2.3	10.0	23.4	101 568
	GoC	19.1	2.3	14.0	24.3	101 568
	SSlp	18.6	2.4	10.8	25.0	376 464
	WC	16.5	1.9	10.9	23.8	72 864
	SC	18.4	2.5	9.9	25.7	272 688
	Gdn	18.5	2.8	12.4	25.7	81 144

I0 (µmol photons m^{-2} s^{-1})	WOff	436.5	177.2	87.7	746.3	101 568
	GoC	465.3	179.1	120.9	749.2	101 568
	SSlp	469.0	184.0	102.6	752.6	376 464
	WC	460.1	189.0	9.9	758.1	72 864
	SC	469.6	185.8	86.6	752.6	272 688
	Gdn	469.6	187.0	106.4	751.5	81 144
K_{PAR} (m^{-1})	WOff	0.2	0.0	0.1	0.6	74 567
	GoC	0.2	0.0	0.1	0.3	79 329
	SSlp	0.2	0.0	0.1	1.3	315 793
	WC	0.2	0.1	0.1	3.2	46 753
	SC	0.2	0.1	0.1	3.5	218 075
	Gdn	0.2	0.1	0.1	2.4	67 635
I_m (µmol photons m^{-2} s^{-1})	WOff	120.8	96.6	8.2	339.2	276
	GoC	143.8	114.7	10.4	380.7	275
	SSlp	160.0	125.5	10.5	486.5	276
	WC	134.5	86.7	9.3	358.4	275
	SC	164.2	128.9	9.9	564.8	276
	Gdn	177.1	140.1	12.5	730.5	275
MLD (m)	WOff	38.0	29.9	9.5	207.9	2 191
	GoC	39.8	34.6	5.9	184.9	2 191
	SSlp	31.8	28.2	3.1	153.3	2 191
	WC	20.3	15.5	7.0	109.2	2 191
	SC	27.2	24.0	1.9	140.8	2 191
	Gdn	20.7	17.6	NV	122.9	2 191
CSET (m^3 s^{-1} km^{-1} coastline)	WC	-508.2	1032.0	-7855.3	4928.2	2 092
	WCSM	-193.0	778.5	-6461.0	4601.3	2 071
	ECSM	-112.7	866.6	-5292.3	10570.0	2 068
UI_{SST} (°C)	WC	1.4	1.3	-1.7	5.1	271
	WCSM	1.0	1.0	-2.5	4.9	274
	ECSM	0.7	1.0	-2.7	3.7	274
Along-shore current velocity (m s^{-1})	Armona	0.1	0.1	-0.2	0.3	2 829
Guadiana discharge (m^3 s^{-1})	PL	29.6	76.5	0.9	1003.7	1 913
Guadalquivir discharge (m^3 s^{-1})	AR	43.5	81.1	0.3	1105.0	2 191
ENSO	-	0.2	0.8	-1.3	2.2	72
NAO	-	0.2	1.2	-3.1	2.4	72
AMO	-	0.2	0.2	-0.1	0.5	72
EA	-	0.7	1.0	-1.7	3.5	72
WeMO	-	-0.3	1.0	-2.3	2.4	72

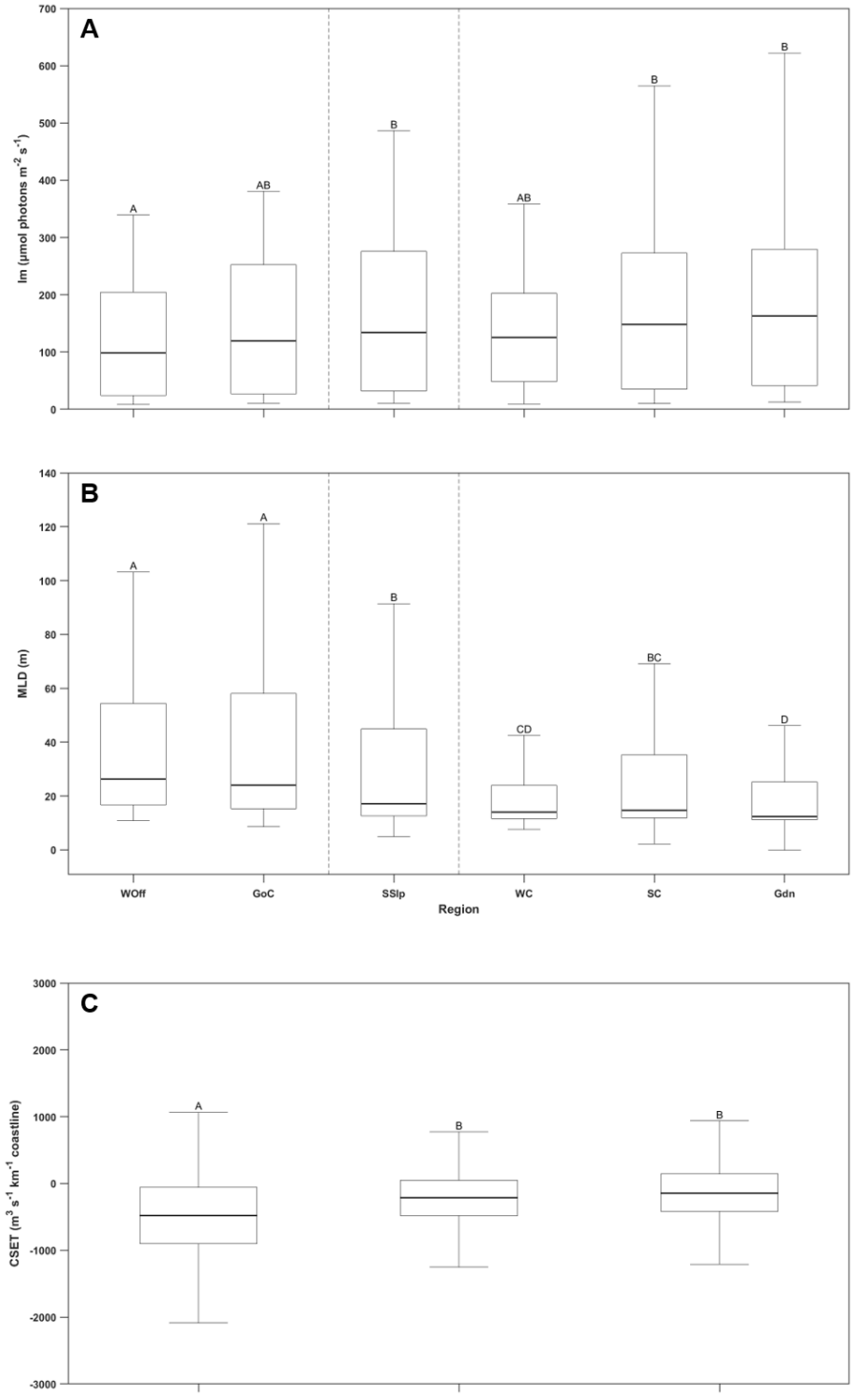
A
Im (µmol photons m-2 s-1)
700
600
500
400
300
200
100
0
A
AB
B
AB
B
B
B
MLD (m)
140
120
100
80
60
40
20
0
A
A
B
CD
BC
D
WOff
GoC
SSlp
WC
SC
Gdn
Region
C
CSET (m3 s-1 km-1 coastline)
3000
2000
1000
0
-1000
-2000
-3000
A
B
B

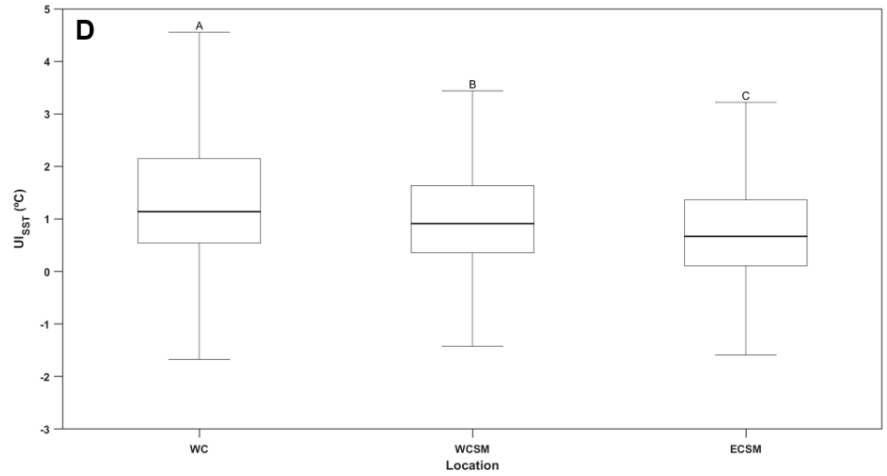

Figure 3.1 - Variability of a set of physical oceanographic variables, including (A) mean Photosynthetically Available Radiation intensity in the mixed layer (I_m), (B) Mixed Layer Depth (MLD), (C) Cross-Shore Ekman Transport (CSET), and (D) temperature-based Upwelling Index (UI_{SST}), for different regions off southern Portugal, during the period 2014-2019. Median values are identified by the central line within the box, the bottom and top edges of the box indicate the 25th and 75th percentiles, respectively, and the whiskers represent non-outlier limits. For each variable, different uppercase letters over the bars denote significant differences across regions ($p < 0.05$). See Figure 2.1 for location and designation of specific regions.

In respect with seasonal variability, SST minima were observed during February-March, while maxima occurred in August-September (Fig. 3.2). Higher I_m was consistently detected during late-spring or early summer (June-July; Fig. 3.3). Deeper MLD were characteristic of the winter season (January-March), while shallower mixed layers were observed between late-spring and early autumn (Fig. 3.4). According with CSET, upwelling favourable conditions prevailed during the spring-summer period, for both WC and SC regions (Fig. 3.5). However, UI_{SST} showed stronger upwelling episodes during summer to early- autumn (Fig. 3.6). Along-shore current velocity data, measured at Armona site, also used to identify the oceanographic regime, showed events of eastward flow (EF; mean velocity: 0.15 m s^{-1}, represent upwelling-favourable conditions) were more frequently observed (70% occasions) than coastal counter-current events (CCC: 30%; mean velocity: 0.14 m s^{-1}, Fig. 3.7). However, a similar proportion of events was observed in summer (EF: 78%; CCC: 22%) and winter periods (EF: 75%; CCC: 25%; data not shown). On average, mean velocity of eastward flows during summer and winter months were similar (0.13 m s^{-1}), albeit CCC were stronger in winter (0.17 m s^{-1}) than in summer (0.09 m s^{-1}). The mean duration of individual upwelling-favourable events and coastal counter-current events was 11.4 ± 4.9 days and 11.6 ± 3.7 days, respectively, with no clear

seasonal trend (EF: 10.0 and 13.2 days; CCC: 11.5 and 12.0 days, in summer and winter, respectively).

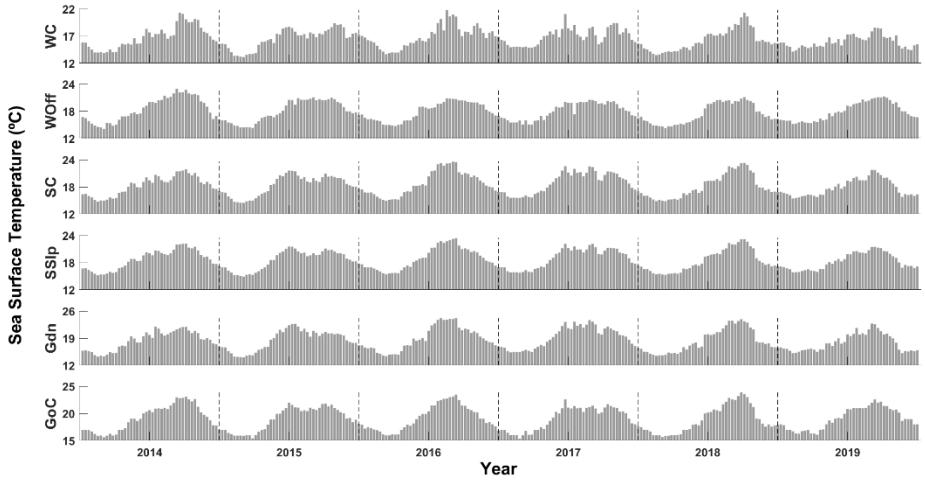

Figure 3.2 – Weekly time series of sea surface temperature (SST) for specific regions off southern Portugal, during the period 2014-2019. See Figure 2.1 for location and designation of specific regions.

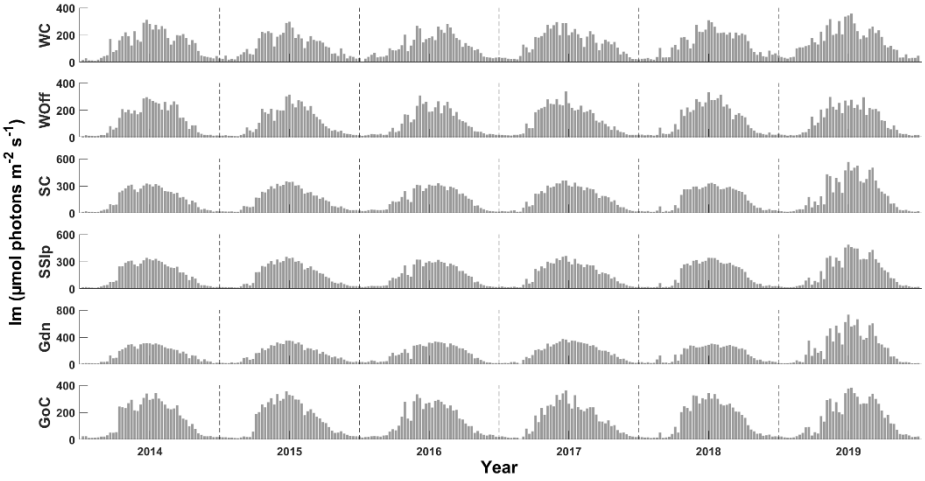

Figure 3.3 – Weekly time series of mean photosynthetically available radiation intensity in the mixed layer (I_m) for specific regions off southern Portugal, during the period 2014-2019. See Figure 2.1 for location and designation of specific regions.

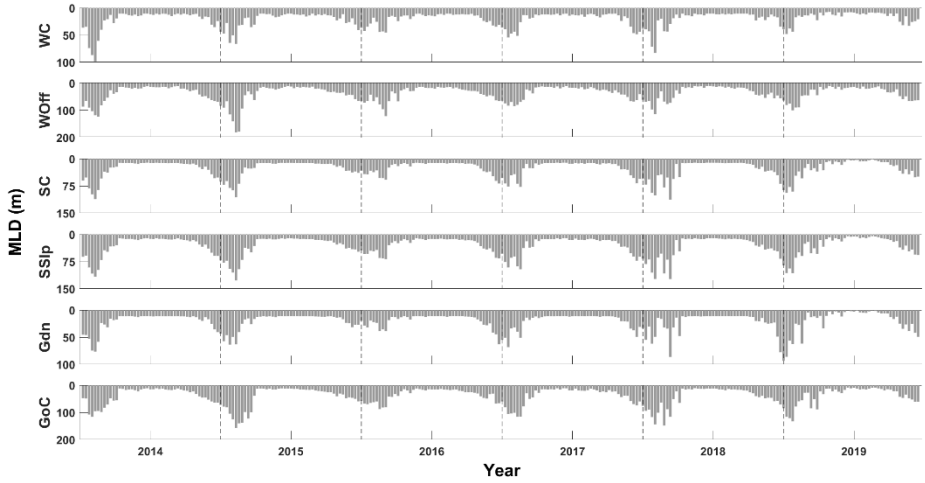

Figure 3.4 – Weekly time series of mixed layer depth (MLD) for specific regions off southern Portugal, during the period 2014-2019. See Figure 2.1 for location and designation of specific regions.

The 6-year study period was characterized by a high interannual variability in meteorological and oceanographic conditions. In respect with other periods, summer seasons of 2014 and 2016 presented higher SST, for all regions, whereas 2015 and 2019 displayed the lowest SST values (Fig. 3.2). Higher MLD were found across different years, while shallower mixed layers were mainly observed in 2019 (Fig. 3.4). Higher I_m values were attained during 2019, at all regions (except WOff; Fig. 3.3). Interannual CSET patterns revealed particularly strong spring upwelling events in 2016 and 2018, for both WC and SC regions, and strong summer upwelling events at WC during 2017 and 2019. Moderate and strong downwelling events were detected using both upwelling indices, during spring (CSET) or summer (UI_{SST}) in 2019, and summer in 2017 (UI_{SST}), along the south coast (Fig. 3.5-3.6). According with alongshore current velocity data, with a short-period available compared with the two upwelling indices, the longest upwelling (~ 27 days) and counter-current events (~ 22 days) occurred during January - February 2019, and October - November 2015, respectively (data not shown). During 2019, a higher number of alternations between CCC and EF events was observed, in respect with other years. Overall, alongshore current velocity paralleled UI_{SST} while showing an opposite pattern to CSET (as the two variables, CSET and UI_{SST}, typically behave in contrast with one another), over the south coast, for both WCSM and ECSM areas (see Appendices B.1 and B.2).

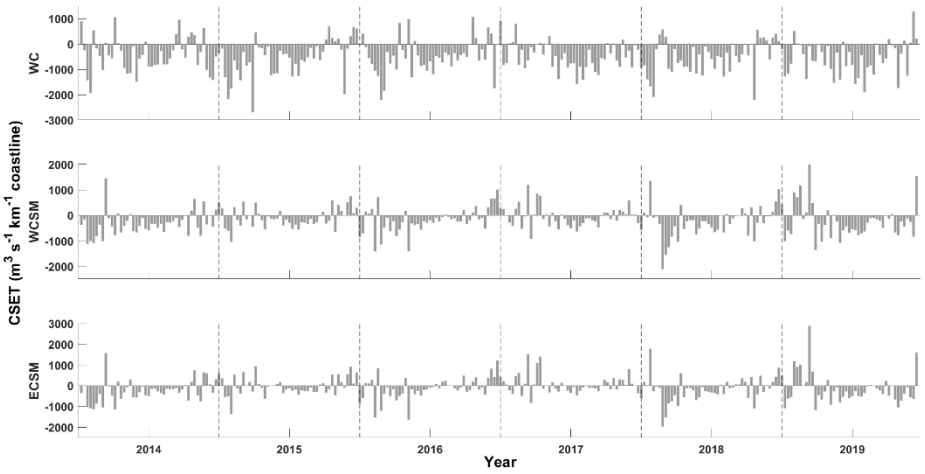

Figure 3.5 – Weekly time series of cross-shore Ekman transport (CSET) for specific regions off southern Portugal, during the period 2014-2019. Negative (positive) values represent upwelling-favourable (downwelling-favourable) conditions. See Figure 2.1 for location and designation of specific regions.

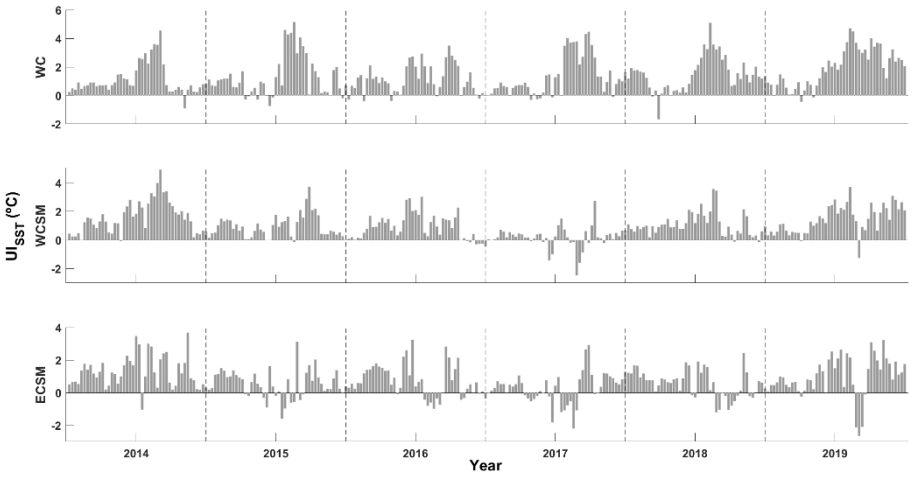

Figure 3.6 – Weekly time series of upwelling index based on Sea Surface Temperature (SST) difference (UI_{SST}) for specific regions off southern Portugal, during the period 2014-2019. Negative (positive) values represent upwelling-favourable (downwelling-favourable) conditions. See Figure 2.1 for location and designation of specific regions.

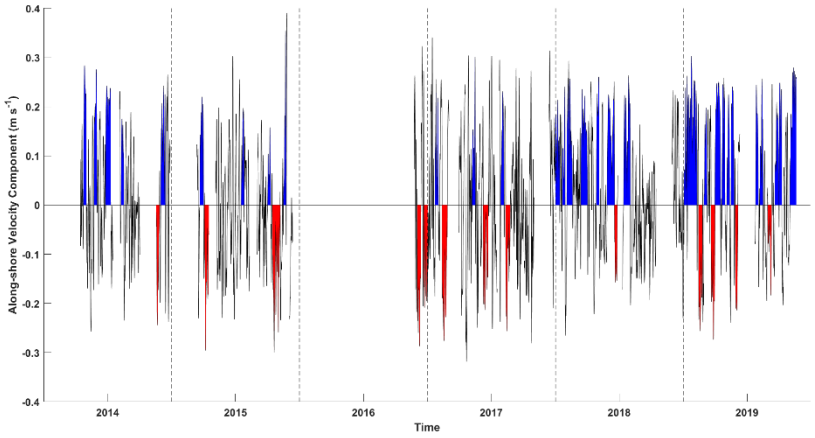

Figure 3.7 – Time series of daily-averaged alongshore current velocity during the period 2014-2019, measured at Armona site (see Fig. 2.1 for location). Blue-labelled positive values represent upwelling regime, and red-labelled negative values indicate downwelling or counterflow conditions. Blank spaces indicate no data available.

3.1.2 Hydrographic and climatological variables

During the 6-year study period, Guadiana (Gdn) and Guadalquivir (Gdq) river discharge averaged 29.6 ± 76.5 and 43.5 ± 81.1 $m^3 s^{-1}$, respectively (see Table 3.1), and showed maxima values during winter, with higher values during March (Fig. 3.8). The years 2014 and 2018 exhibited higher discharges, for both river basins, while 2015 was the driest year in the Guadalquivir basin.

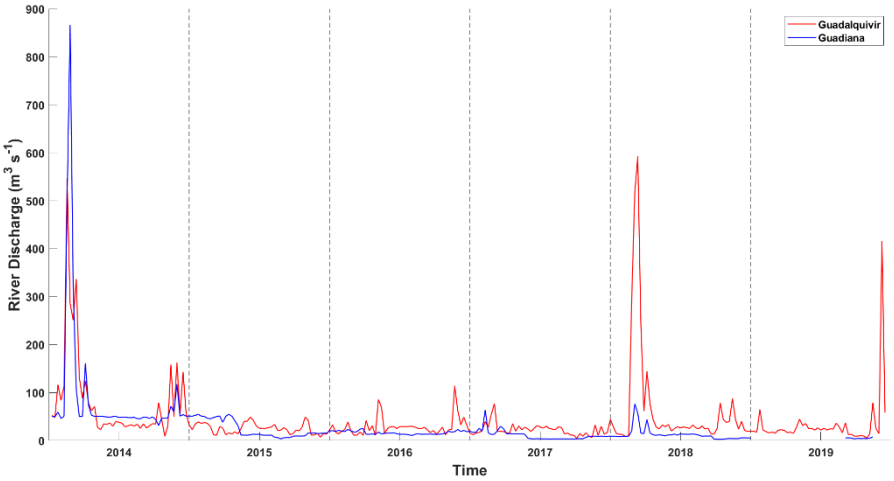

Figure 3.8 - Weekly time series of Guadalquivir (red line) and Guadiana (blue line) river discharge during the period 2014-2019.

Time series of the climate indices influencing the NE Atlantic region are represented in Figure 3.10. MEI showed strong El Niño (warm) events during 2015-2016, and weaker La Niña (cold) events in 2017-2018 (Fig. 3.9). NAO index exhibited high interannual variability, between positive and negative phases, but two persistent positive phases were observed during 2014-2015 and 2018, and two major negative periods were detected in 2015 and 2019 (longer for the latter). AMO remained mostly positive during the study period. EA index revealed a long generally positive period between 2014 and 2017, followed by a high variability period. WeMO index, apart from minor positive episodes, was mostly negative.

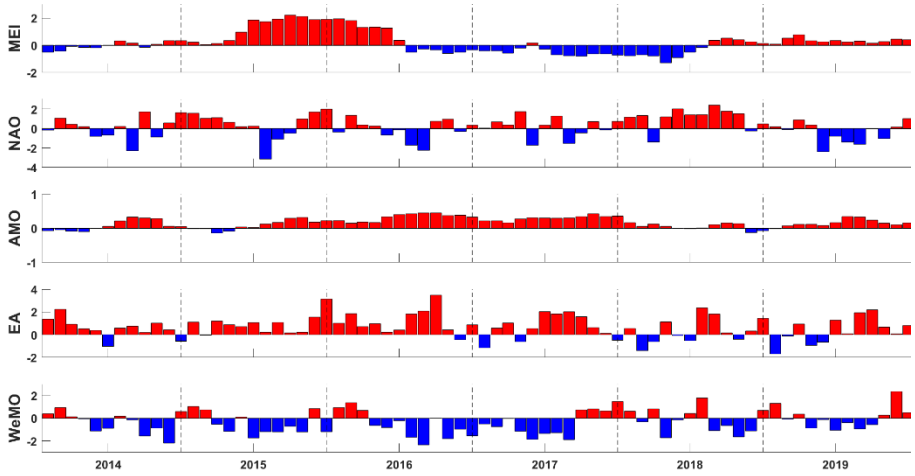

Figure 3.9 - Monthly time series of five relevant large-scale climate indices (Multivariate El Niño Southern Oscillation - MEI, North Atlantic Oscillation - NAO, Atlantic Multidecadal Oscillation - AMO, East Atlantic pattern - EA and Western Mediterranean Oscillation - WeMO) for the region of interest, during the period 2014-2019. Red color shows positive values (La Niña events), and blue color, negative values (El Niño events).

3.2 Phytoplankton variability patterns and phenology

3.2.1 Phytoplankton variability patterns

Region-specific Chl-a mean values ranged between 0.17 ± 0.07 µg L^{-1} and 0.61 ± 0.40 µg L^{-1} for GoC and WC areas, respectively. A clear coastal-offshore gradient was observed, with significantly higher values in regions closer to the coast, especially upwelling (WC) and river-influenced (Gdn), intermediate values over the slope (SSlp), and lower values over oceanic areas (see Table 3.2; Fig. 3.10). However, no difference in mean Chl-a was detected between WOff and SSlp regions.

Table 3.2 - General statistical information, including mean, standard deviation (SD), minimum (Min) and maximum (Max) values, and number of samples (N), for chlorophyll-a concentration (Chl-a), phytoplankton abundance of three specific toxigenic groups responsible for ASP

(Amnesic Shellfish Poisoning), DSP (Diarrhetic Shellfish Poisoning) and PSP (Paralytic Shellfish Poisoning) human syndromes, and toxin concentrations in two of the most recurrently surveyed bivalve species (*Mytilus* spp. and *Donax trunculus*), for different spatial domains off southern Portugal (Chl-a: regions WOff, GoC, SSlp, WC, SC, Gdn; Phytoplankton abundance and toxins: shellfish production areas L6, L7a, L7c, L8 and L9). HY: Homoyesso- and Yessotoxins, bd: below detection level. See Figure 2.1 for location and designation of specific domains. N corresponds to the number of exact available measurements for each region, considering single (coastal production areas) or multiple sampling points (Chl-a regions).

Variable	Domain	Mean	SD	Min	Max	N
Chl-a (µg L^{-1})	WOff	0.23	0.13	0.06	2.12	74 567
	GoC	0.17	0.07	0.06	0.87	79 329
	SSlp	0.26	0.22	0.06	6.20	315 791
	WC	0.61	0.40	0.06	6.44	46 751
	SC	0.38	0.40	0.07	9.38	218 071
	Gdn	0.54	0.58	0.09	9.38	67 632
ASP-producing species (x 10^3 cells L^{-1})	L6	9.9	22.3	bd	226.0	347
	L7a	13.3	55.1	bd	812.0	290
	L7c	25.1	74.9	bd	732.1	435
	L8	11.2	37.8	bd	311.5	345
	L9	13.2	41.8	bd	433.1	299
DSP-producing species (x 10^3 cells L^{-1})	L6	0.7	10.4	bd	192.9	347
	L7a	2.5	40.3	bd	685.7	290
	L7c	1.2	20.6	bd	429.2	435
	L8	0.2	0.9	bd	13.8	345
	L9	0.4	4.2	bd	72.1	299
PSP-producing species (cells L^{-1})	L6	43.7	297.7	bd	4750.0	347
	L7a	37.2	228.5	bd	3200.0	290
	L7c	43.7	249.4	bd	3560.0	435
	L8	110.7	471.8	bd	4840.0	345
	L9	83.0	347.4	bd	3040.0	299
HY-producing species (cells L^{-1})	L6	5.8	22.6	bd	230.0	212
	L7a	4.8	30.9	bd	400.0	180
	L7c	7369.4	94876.1	bd	1476246.0	261
	L8	3217.6	30367.8	bd	354365.0	148
	L9	1670.6	13670.3	bd	165640.0	179
ASP toxins in *Mytilus* spp. (mg/kg)	L6	2.5	5.4	bd	14.1	114
	L7a	1.5	4.4	bd	14.1	107
	L7c	1.6	5.1	bd	52.0	366
	L8	3.5	6.1	bd	14.1	91
ASP toxins in *Donax trunculus* (mg/kg)	L6	0.6	2.5	bd	14.1	71
	L7c	1.6	4.6	bd	14.1	18
	L8	2.1	4.7	bd	16.0	182
	L9	2.1	4.9	bd	23.0	201
	L6	133.5	172.1	bd	847.0	99

DSP toxins in *Mytilus* spp. (µg OA equiv/kg)	L7a	130.3	155.6	bd	850.0	96
	L7c	130.5	140.7	bd	850.0	332
	L8	107.4	82.7	bd	360.0	87
DSP toxins in *Donax trunculus* (µg OA equiv/kg)	L6	186.5	176.2	bd	850.0	90
	L7c	222.6	158.9	bd	550.0	22
	L8	204.0	167.5	bd	850.0	221
	L9	178.5	147.1	bd	883.0	235
PSP toxins in *Mytilus* spp. (µg STX equiv/kg)	L6	264.6	1460.7	bd	15663.0	116
	L7a	183.1	460.5	bd	3256.0	105
	L7c	82.2	218.5	bd	2400.0	353
	L8	142.1	243.1	bd	565.7	86
PSP toxins in *Donax trunculus* (µg STX equiv/kg)	L6	422.5	796.5	bd	2400.0	92
	L7c	63.5	182.7	bd	565.7	18
	L8	72.6	207.8	bd	1491.0	179
	L9	62.6	176.1	bd	565.7	194

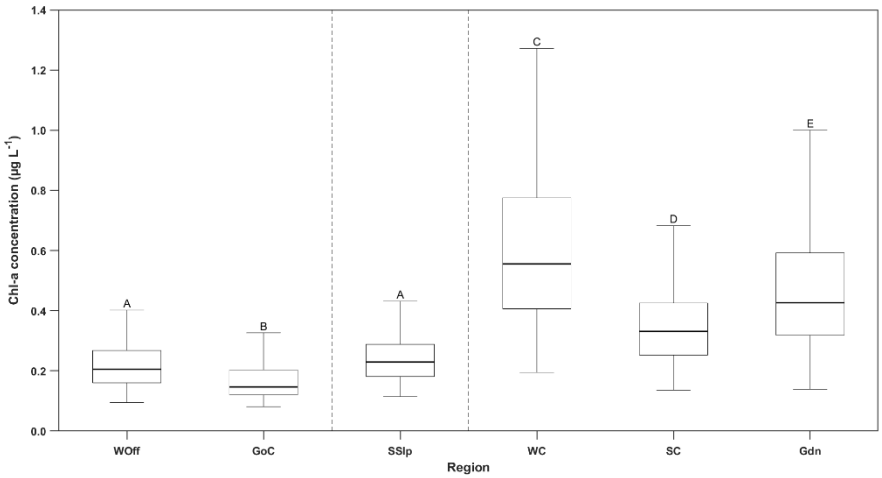

Figure 3.10 - Variability of chlorophyll-a concentration (Chl-a) for different regions off southern Portugal, during the period 2014-2019. Median values are identified by the central line within the box, the bottom and top edges of the box indicate the 25th and 75th percentiles, respectively, and the whiskers represent non-outlier limits. For each variable, different uppercase letters over the bars denote significant differences across regions ($p < 0.05$). See Figure 2.1 for location and designation of specific regions.

Overall, Chl-a over oceanic regions (WOff and GoC) displayed unimodal annual cycles, with increasing trends from autumn (October-November) to late-winter maxima (February-March; Fig. 3.11). The slope region (SSlp) was characterized by an additional brief Chl-a peak during July-August, and upwelling-influenced regions (WC and SC) showed a bimodal annual pattern, with late-winter and summer maxima. At SC region, late-winter Chl-a peak surpassed the summer peak, while the opposite occurred for the WC region. The coastal region influenced by river flow (Gdn) exhibited a unimodal annual cycle, with maxima during March. In respect

of interannual variability (Fig. 3.12), Chl-a over GoC and WOff regions was less variable, followed by SSlp, SC, Gdn, and lastly the WC region. Higher Chl-a values were attained during 2014 and 2016, for all regions except SSlp (maximum for 2017) and WC (only for 2016).

Decomposition of Chl-a time series, based on GAMM analyses, revealed a highly significant monthly variability pattern ($p < 0.001$), for all regions (see Appendix C.1, Table C.1). Significant interannual trends during the 6-year study period were also detected for all regions except WC ($p = 0.114$). Chl-a for oceanic areas showed non-linear declining trends between 2015-2016 and 2019 (WOff and GoC, $p < 0.001$). The intermediate region (SSlp) also revealed a non-linear Chl-a declining trend until mid-2017, followed by a non-linear increasing trend ($p < 0.001$). Chl-a over SC and Gdn regions displayed similar interannual patterns, with an early non-linear decline up to 2017, and a subsequent non-linear increase (see Appendix C.1, Table C.1).

Regarding the influence of oceanographic physical regimes, no significant differences in Chl-a were observed between the three physical oceanographic regimes (upwelling, downwelling and mixed) for oceanic regions (Fig. 3.13). Nonetheless, for intermediate and coastal regions, significant differences in Chl-a were detected between upwelling and downwelling or mixed regimes. Over SSlp and, using CSET, a wind-based upwelling index, mean Chl-a was higher under upwelling-favourable conditions, and higher variability was observed under downwelling-favourable conditions. Yet, UI_{SST} and along-shore current velocity showed no differences between physical regimes, and higher variability in Chl-a during upwelling-favourable and mixed regimes, respectively. In the WC region, differences in Chl-a were observed between all oceanographic regimes using CSET, or only between upwelling-favourable and mixed conditions for UI_{SST}. For the SC region, higher Chl-a was also detected during upwelling-favourable periods in respect to mixed (using CSET or the along-shore current velocity) or downwelling regimes (based on UI_{SST}; Fig. 3.13). Thus, independently of the upwelling index considered (CSET or UI_{SST}), Chl-a mean values and variability were higher during upwelling-favourable periods, for both SC and WC regions. However, considering along-shore current velocity, higher variability in Chl-a was detected under mixed conditions. Over the Gdn region, higher Chl-a was also observed with upwelling conditions, but variation was higher with mixed conditions (Fig. 3.13).

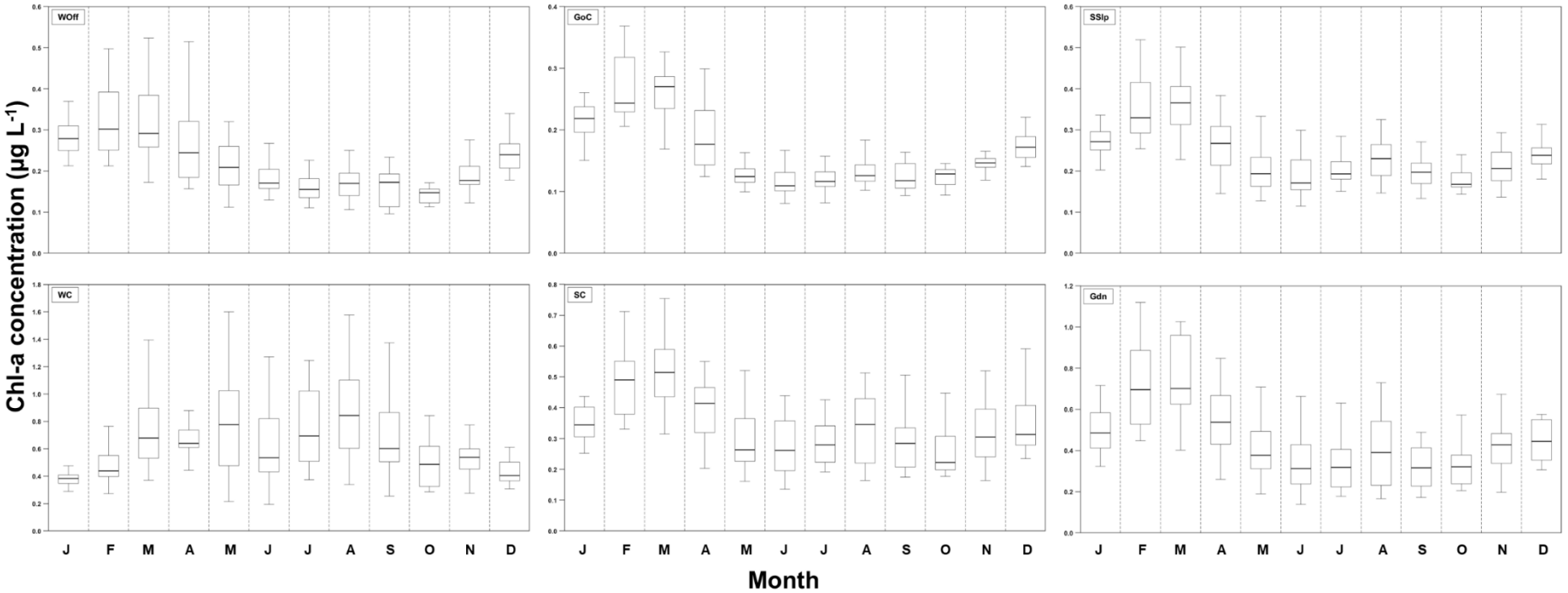

Figure 3.11 – Monthly variability of chlorophyll-a concentration (Chl-a) for different regions off southern Portugal (WOff, GoC, SSlp, WC, SC and Gdn), during the period 2014-2019. Median values are identified by the central line within the box, the bottom and top edges of the box indicate the 25th and 75th percentiles, respectively, and the whiskers represent non-outlier limits. Note differences in scale between regions. See Figure 2.1 for location and designation of specific regions.

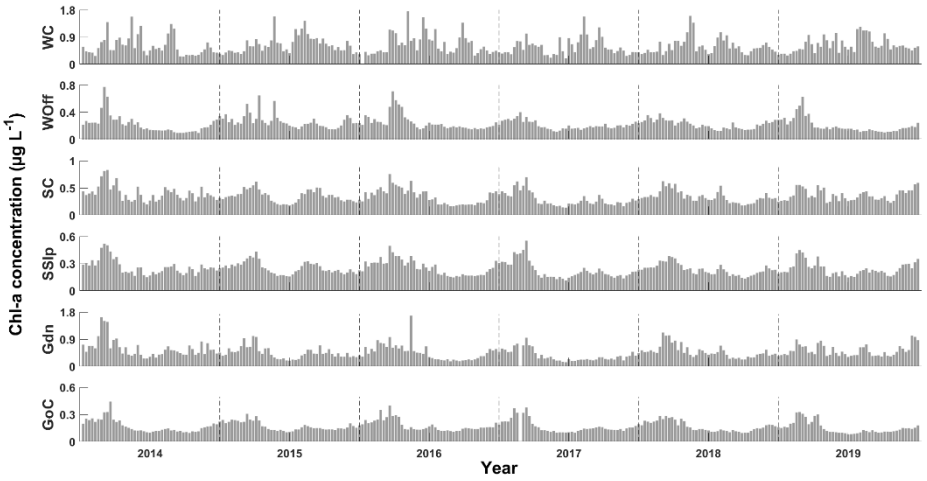

Figure 3.12 – Weekly time series of chlorophyll-a concentration (Chl-a) for specific regions off southern Portugal, during the period 2014-2019. Note differences in scale between regions. See Figure 2.1 for location and designation of specific regions.

The influence of oceanographic physical regimes on Chl-a within specific seasons was also evaluated using CSET (WOff, SSlp, WC, SC) and along-shore current velocity (SSlp, SC, Gdn) as upwelling indices (Fig. 3.14). Based on CSET, mean Chl-a was higher during upwelling-favourable regimes, compared to mixed regimes, in spring (SSlp, WC) and summer season (SSlp, SC). Also, higher Chl-a under upwelling-favourable conditions, in respect to downwelling-favourable conditions was observed during summer (WOff, WC). By contrast, during winter, mean Chl-a was lower under upwelling-favourable regimes in comparison with downwelling/counterflow (SC) or mixed regimes (SC, Gdn; Fig. 3.14). Considering along-shore current velocity, Chl-a mean values during summer were significantly higher under upwelling-favourable conditions, compared to mixed conditions, for SSlp and SC regions. In winter, Chl-a under upwelling-favourable regimes was significantly lower compared to both downwelling/counterflow and mixed regimes (Fig. 3.15). Overall, during autumn, no differences in Chl-a were detected between physical oceanographic regimes in any of the study regions.

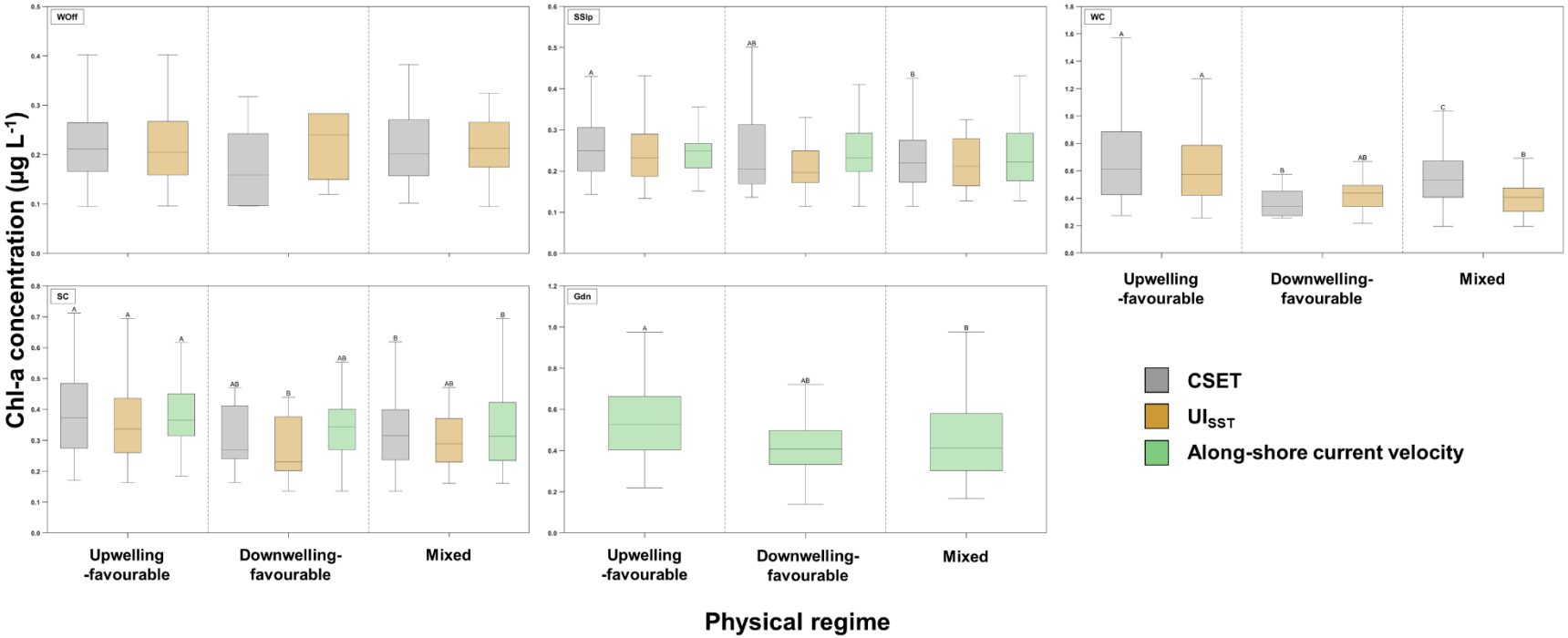

Figure 3.13 - Variability of chlorophyll-a concentration (Chl-a) in five different regions off southern Portugal (WOff, SSlp, WC, SC, Gdn), during the period 2014-2019, under three different physical oceanographic regimes: upwelling-favourable, downwelling-favourable, and mixed. The identification of oceanographic physical regimes was based on the use of different upwelling indices, depending on the region: a wind-based index, cross-shore Ekman transport, CSET (represented by a grey color), temperature-based upwelling index, UI_{SST} (brown color), and along-shore current velocity measured at the Armona site (green color). Note differences in scale between regions. Median values are identified by the central line within the box, the bottom and top edges of the box indicate the 25th and 75th percentiles, respectively, and the whiskers represent non-outlier limits. For each method, different uppercase letters over the bars denote significant differences between physical regimes ($p < 0.05$). See Figure 2.1 for location and designation of specific regions, and others (UI_{SST}, Armona).

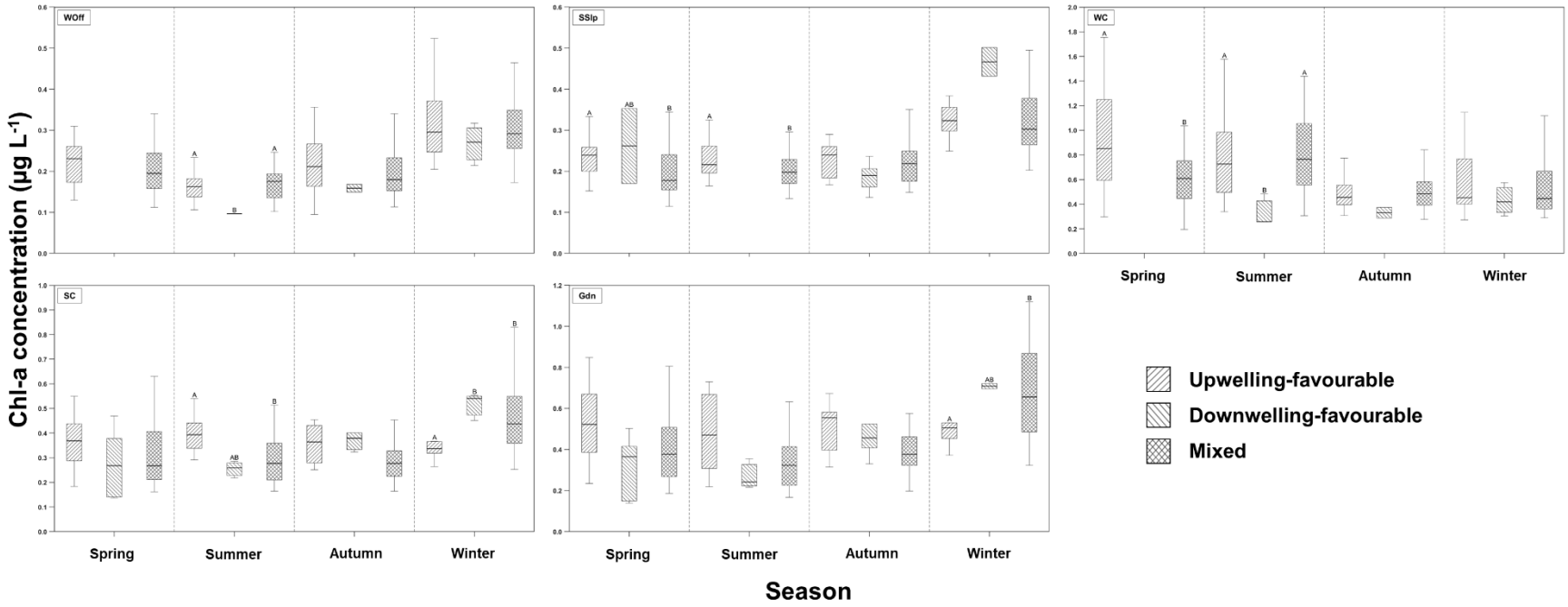

Figure 3.14 - Mean seasonal chlorophyll-a concentration (Chl-a) in five different regions off southern Portugal (WOff, SSlp, WC, SC, Gdn), during the period 2014-2019, binned according with three physical oceanographic regimes, represented by different patterns: (1) upwelling-favourable - single line bending upwards; (2) downwelling-favourable - single line bending downwards; and (3) mixed regime - crossed lines. Note differences in scale between regions. Median values are identified by the central line within the box, the bottom and top edges of the box indicate the 25th and 75th percentiles, respectively, and the whiskers represent non-outlier limits. For each region, different uppercase letters over the bars denote significant differences between physical regimes within each season ($p < 0.05$). Physical regimes were defined using either the wind-based upwelling index (CSET; WOff, SSlp, WC, SC), or the along-shore current velocity (Gdn). See Figure 2.1 for location and designation of specific regions, and others.

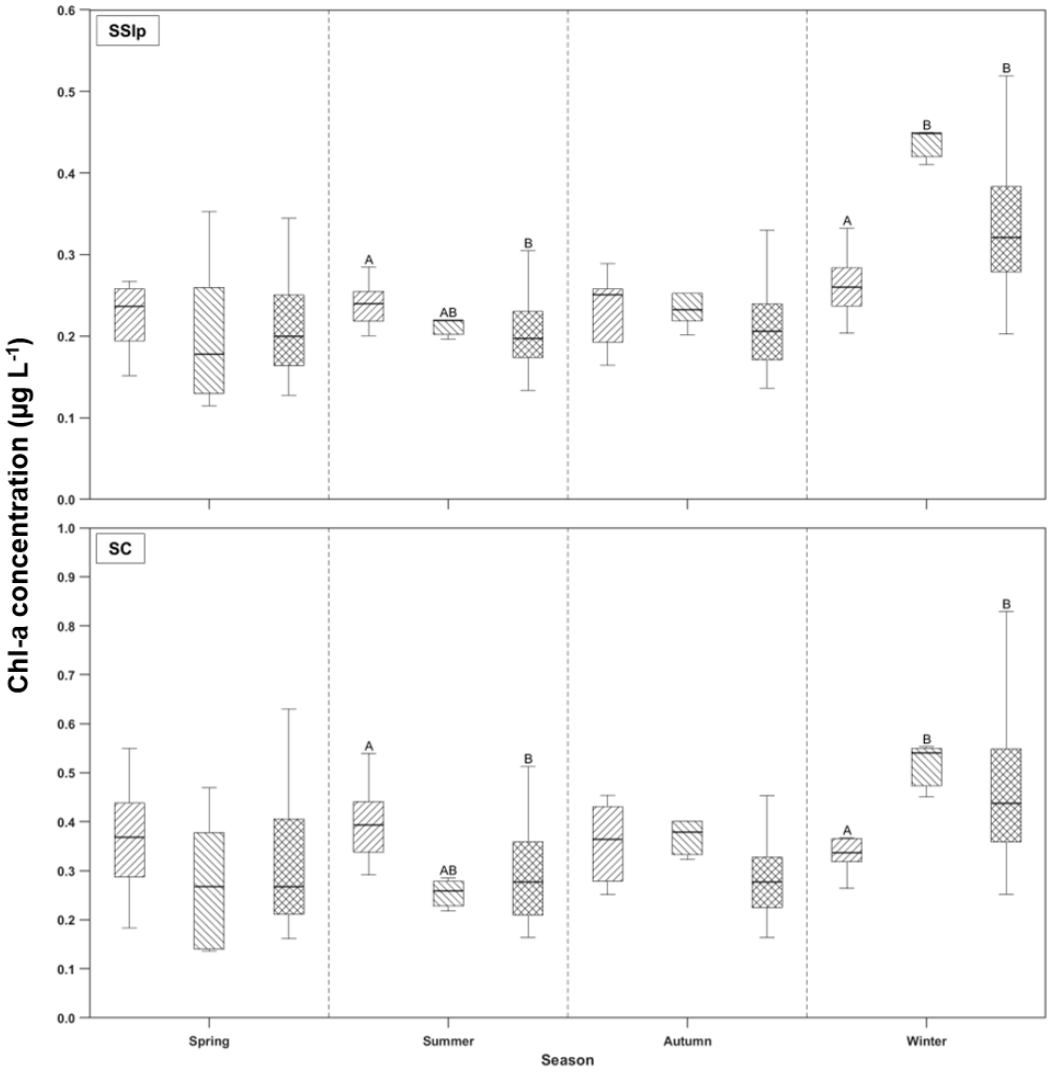

Figure 3.15 - Mean seasonal chlorophyll-a concentration (Chl-a) for South Slope (SSlp) and South Coast (SC) regions, during the period 2014-2019, binned according with three physical oceanographic regimes, represented by different patterns: (1) upwelling-favourable - single line bending upwards; (2) downwelling-favourable - single line bending downwards; and (3) mixed regime - crossed lines. Note differences in scale between regions. Median values are identified by the central line within the box, the bottom and top edges of the box indicate the 25th and 75th percentiles, respectively, and the whiskers represent non-outlier limits. For each region, different uppercase letters over the bars denote significant differences between physical regimes within each season ($p < 0.05$). Physical regimes defined using the along-shore current velocity. See Figure 2.1 for location of specific regions, and others.

3.2.2 Phytoplankton phenology

Basic statistical information on phytoplankton phenological indices, estimated using Chl-a time series (over a 6-year period), for different regions (WOff, GoC, SSlp, WC, SC, Gdn), is summarized in Table F.1 (see appendices). Mean number of bloom events per year varied from two to five, at GoC and WC, respectively. The slope region (SSlp) showed a mean number of blooms per year similar to oceanic regions (approximately two; Fig. 3.16A). Average bloom

duration showed an opposite pattern, ranging from four to 13 weeks bloom^{-1}, at WC and GoC, respectively (Appendix F.1). Overall, bloom frequency and average bloom duration were higher or lower, respectively, at WC compared with GoC and SSlp areas ($p < 0.05$; Fig. 3.16A and Appendix F.1). Region-specific mean Chl-a peak values varied between 0.36 µg L^{-1} (GoC) and 1.56 µg L^{-1} (WC), with lower values at GoC and SSlp in comparison with WC and Gdn ($p < 0.05$; Fig. 3.16C). The principal bloom initiation, peak and termination timings ranged, on average, from late-November to late-May (week of the year, WOY: 11-33), early-March to mid-June (WOY: 24-36), and mid-April to late-June (WOY: 29-38), respectively. For the WC area, delayed timings ($p < 0.05$) were observed with respect to GoC (initiation timing; Fig. 3.16G), WOff and Gdn (peak timing; Fig. 3.16H), and SC in addition to the latter regions (termination timing; Fig. 3.16I). Also, principal blooms exhibited shorter accumulation and deceleration phases at WC (three weeks year^{-1}, and two weeks year^{-1}, respectively) compared to GoC (12 weeks year^{-1}, and six weeks year^{-1}, respectively; $p < 0.05$; Fig. 3.16E-F). Region-specific mean timings for secondary blooms revealed later onset, from early-February to late-April (WOY: 20-30), but earlier peak, from late-February to mid-May (WOY: 22-32), and termination timings, from mid-March to late-May (WOY: 25-34), with respect to principal blooms. However, no differences in secondary bloom indices were detected across regions (Fig. 3.16J-L).

3.2.3 Environmental drivers of phytoplankton biomass

GAMM models were developed to explore the functional relationships between environmental variables (predictors), and Chl-a and HAB abundance (response variables) for different spatial domains. The explanatory power of the best performing Chl-a models, expressed as the percentage of Chl-a variance explained, was higher for open ocean (WOff and GoC; 52-77%) and river-influenced regions (Gdn; 60%), and lower for other regions (SSlp, SC, and WC; 14-49%), being lowest for WC. SST was the predictor with the highest partial effect for all six regions considered, showing negative linear (WOff, SSlp, SC, Gdn) or non-linear influences (GoC, WC; Fig. 3.17 and Table E.1) on Chl-a. Overall, SST values below ca. 18 ºC were associated with positive Chl-a anomalies. For WOff region, MLD was the second most influential predictor, with a negative non-linear influence on Chl-a, stronger for MLD values higher than ca. 75 m. Over GoC region, PAR and EA were less influential predictors of Chl-a. PAR revealed negative non-linear partial effects, with a positive minor influence on Chl-a for values below ca. 500 µmol photons m^{-2} s^{-1}. In turn, positive EA values were associated with positive Chl-a anomalies for GoC. At the slope region (SSlp), SST was identified as the

only relevant (linear) predictor of Chl-a. Over the WC region, MLD exhibited non-linear positive effects on Chl-a up to ca. 20 m depth, and a negative influence for higher MLD values. AMO was a less relevant ($p < 0.01$) linear predictor at WC, with values above ca. 0.1 associated with positive Chl-a anomalies. For both SC and Gdn regions, Guadalquivir river discharge appeared as the second most influential predictor of Chl-a, stronger for the Gdn region, with positive non-linear effects for river discharges up to 300 $m^3 s^{-1}$. Additionally, for the SC region, PAR above ca. 500 µmol photons $m^{-2} s^{-1}$ showed a positive linear influence on Chl-a.

3.3 Harmful algal bloom patterns and phenology

3.3.1 Harmful algal bloom spatio-temporal patterns

Basic statistical information on abundance of HAB-forming phytoplankton for different spatial domains off southern Portugal, including average, standard-deviation, minimum and maximum values, is summarized in Table 3.2. Region-specific mean abundance of ASP-producers ranged from 9942.3 ± 22267.1 cells L^{-1} to 25138.9 ± 74882.9 cells L^{-1}, at L6 and L7c, respectively. For this group, abundances at L7a, L8 and L9 were lower than L6 and L7c ($p < 0.05$, Fig. 3.18). Mean abundance of DSP-producers varied from 227.5 ± 946.8 cells L^{-1} to 2473.1 ± 40266.2 cells L^{-1}, at L8 and L7a, correspondingly. Higher DSP abundances were detected at L8 compared to L9 and L7a, as well as over L9 with respect to L7a. L7a presented lower abundances in comparison to all the remaining areas ($p < 0.05$). Mean region-specific abundances of PSP-producers fluctuated between 37.2 ± 228.5 cells L^{-1} and 110.7 ± 471.8 cells L^{-1}, at L7a and L8, respectively, following the opposite pattern of DSP-producers. Higher PSP abundances were detected over L8 and L9, whereas L7a showed lower abundances ($p< 0.05$: Fig. 3.18). The abundance of Homoyesso- and Yessotoxin (HY)-producers varied, on average, from 4.8 ± 30.9 cells L^{-1} to 7369.4 ± 94876.1 cells L^{-1}, at L7a and L7c, respectively, but no differences were observed amongst production areas (data not shown).

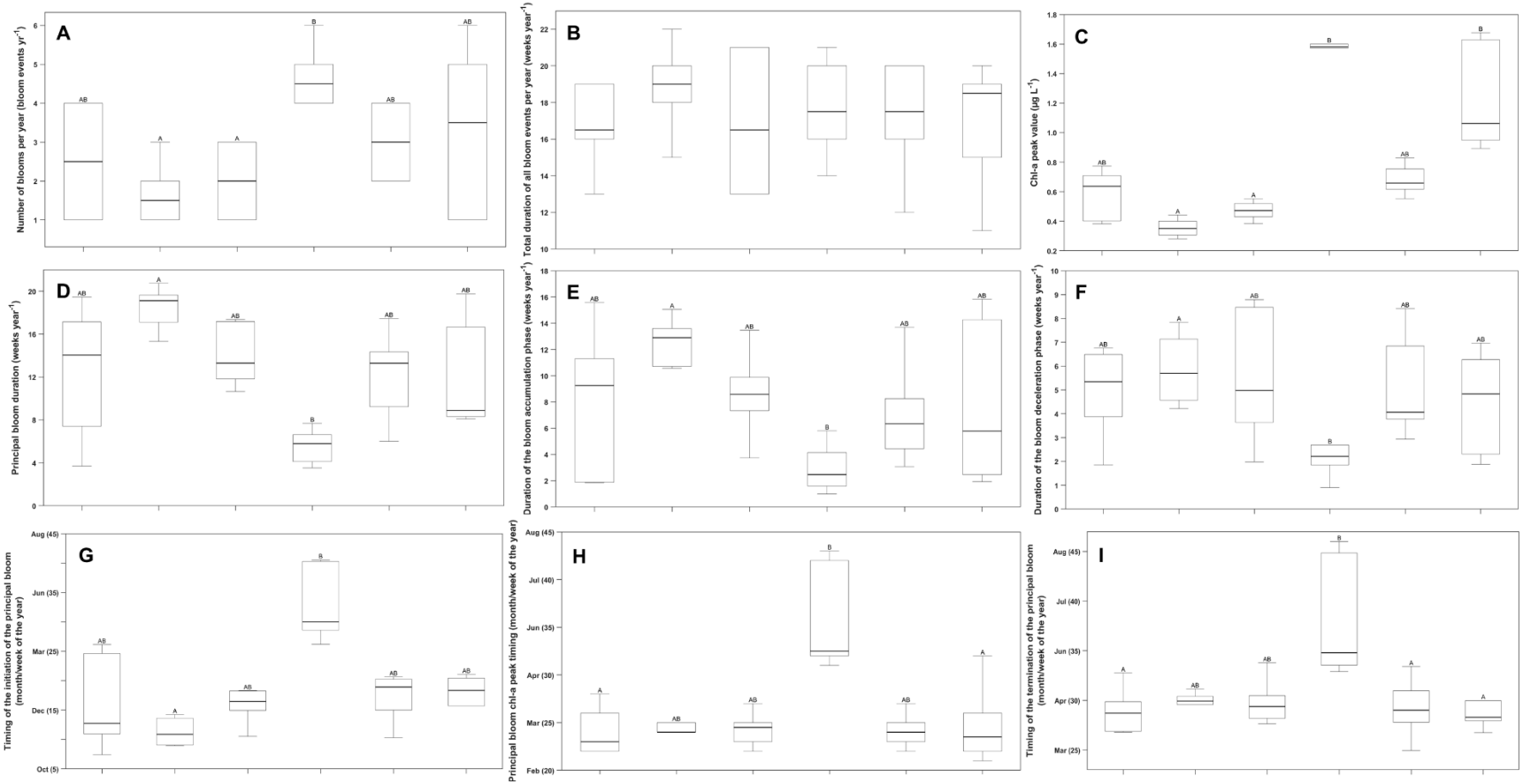
A
Number of blooms per year (bloom events yr^{-1})
B
Total duration of all bloom events per year (weeks year^{-1})
C
Chl-a peak value (µg L^{-1})
D
Principal bloom duration (weeks year^{-1})
E
Duration of the bloom accumulation phase (weeks year^{-1})
F
Duration of the bloom deceleration phase (weeks year^{-1})
G
Timing of the initiation of the principal bloom (month/week of the year)
H
Principal bloom chl-a peak timing (month/week of the year)
I
Timing of the termination of the principal bloom (month/week of the year)

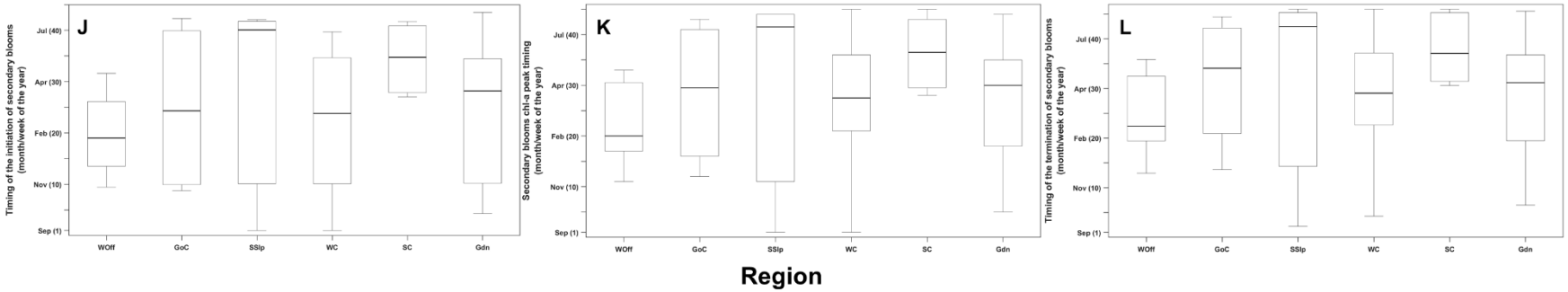

Figure 3.16 - Phytoplankton phenological indices, based on chlorophyll-a time series (Chl-a), for specific regions off southern Portugal during the period 2014-2019. (A) Number of bloom events per year; (B) Total duration of all bloom events per year; (C) Chl-a peak value; (D) Duration of principal bloom duration; (E) Duration of the (principal) bloom accumulation phase; (F) Duration of the (principal) bloom deceleration phase; (G) Principal bloom initiation timing; (H) Principal bloom peak timing; (I) Principal bloom termination timing; (J) Secondary bloom initiation timing; (K) Secondary bloom peak timing; and (L) Secondary bloom termination timing. Median values are identified by the central line within the box, the bottom and top edges of the box indicate the 25^{th} and 75^{th} percentiles, respectively, and the whiskers represent non-outlier limits. For each phenological index, different uppercase letters over the bars denote significant differences across regions ($p < 0.05$). See Figure 2.1 for designation and location of specific regions.

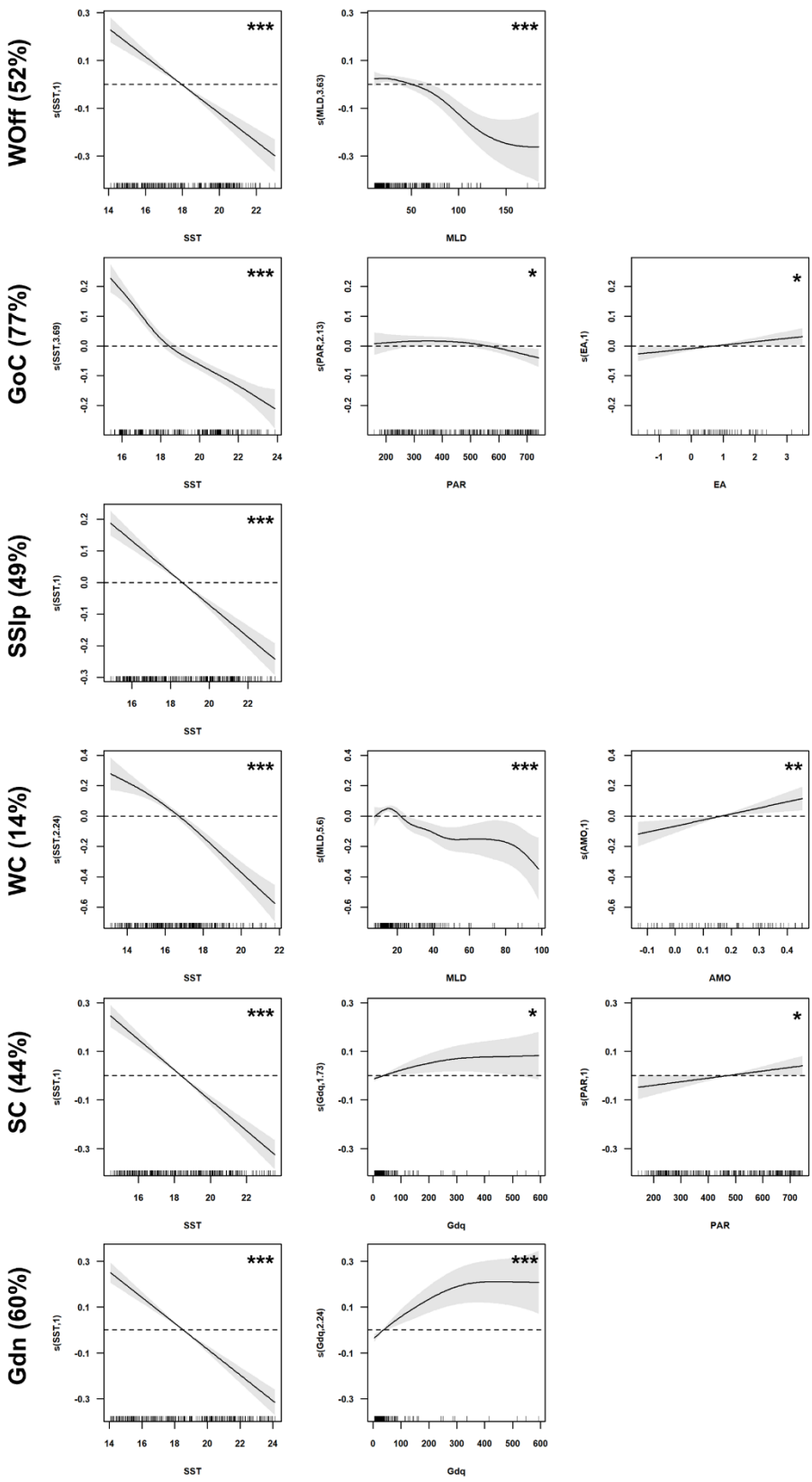

Figure 3.17 - Partial effects of individual environmental predictors on chlorophyll-a (Chl-a) anomalies, for each region off southern Portugal, during the period 2014-2019, derived from the best performing generalized additive mixed models (GAMM). For each region, the model explanatory power (as % of Chl-a variance explained) is presented in brackets, after region abbreviation; the set of plots for each region is organized in descending order of their

explanatory power, and the significance level (p-value) of each predictor is denoted by asterisk symbols (top right), where *, **, *** indicate p-values <0.05, <0.01 and <0.001, respectively. Each solid line represents the fitted models and grey shaded areas represent the 95% confidence intervals. Short vertical lines on the x-axis represent the actual predictor observations, and the values on the y-axis denote the effective degrees of freedom (edf). Edf values of 1 represent a linear effect of the predictor on Chl-a anomaly, and values higher than 1 indicate non-linear effects. Positive (negative) y-values indicate a positive (negative) influence on Chl-a concentration. See Figure 2.1 for designation and location of specific regions.

In general, the abundance of ASP-toxin producers followed a bimodal annual cycle, with peaks occurring during spring (March-April) and summer (July-August; Fig. 3.19, left column), for most production areas, except L7a, which revealed a unimodal cycle with a peak in July. During the study period, abundances of ASP-producers were systematically lower than the regulatory alert level used by IPMA regular monitoring program (80.000 cells L^{-1}), with the exception of few cases (between 2% and 8%, at L6/L7a and L7c, respectively; Fig. 3.20). GAM analyses further demonstrated the existence of highly significant intra-annual variability patterns for ASP-producing species ($p < 0.001$), for all production areas, except L9 (Appendix C.2, Table C.2). Significant interannual non-linear increasing trends were only detected for this group at L6 ($p < 0.001$), and L7c-L8 areas ($p < 0.05$).

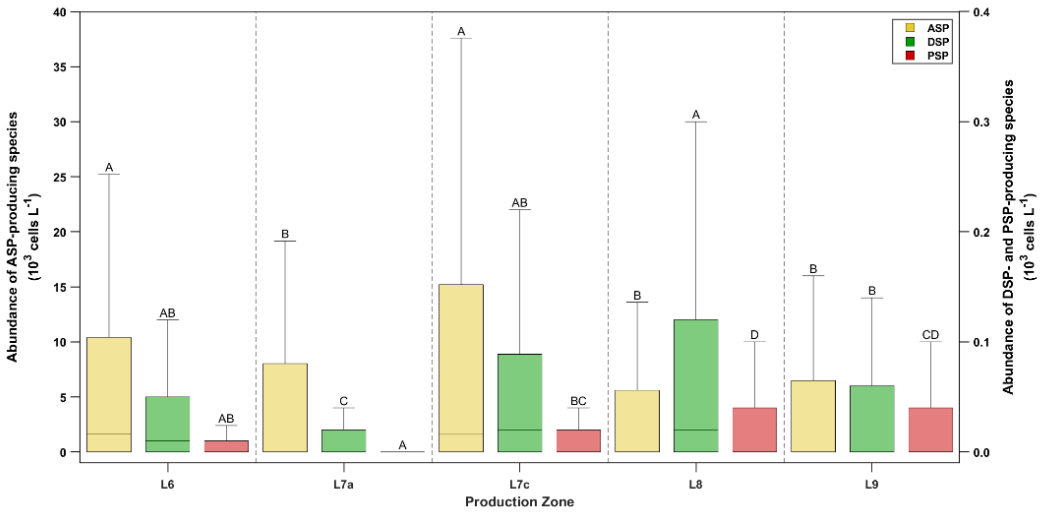

Figure 3.18 - Variability of the abundance of ASP (Amnesic Shellfish Poisoning), DSP (Diarrhetic Shellfish Poisoning) and PSP (Paralytic Shellfish Poisoning)-producing species, represented by yellow, green and red colors, respectively, for different coastal bivalve production areas (L6, L7a, L7c, L8, L9), during the period 2014-2019. Note differences in scale between harmful algal bloom (HAB) groups. Median values are identified by the central line within the box, the bottom and top edges of the box indicate the 25th and 75th percentiles, respectively, and the whiskers represent non-outlier limits. For each group, different uppercase letters over the bars denote significant differences across regions ($p < 0.05$). See Figure 2.1 for site/area location.

DSP-producers exhibited a unimodal annual cycle, with maxima during spring (April and June, at L8 and L6, respectively), or summer (July-September, for other areas; Fig. 3.19). During the study period, the regulatory alert level for DSP-producers (200 cells L^{-1}) was surpassed every year in all production areas (L6: 9% samples; L7c: 14%; L8: 17%; L9: 8%), except L7a (only 2015-2016, and 2018-2019, 4%; Fig. 3.21). GAM/GAMM analyses also revealed highly significant intra- and interannual variability patterns for DSP-producers ($p < 0.001$), for all regions, although interannual patterns were less significant ($p < 0.01$) for L7c-L8 (Appendix C.3, Table C.3). For L6 and L7a areas, DSP-producers increased non-linearly until ca. year 2018, declining subsequently. Non-linear increasing trends were also detected for L7c-L8 and L9, with a more pronounced increase between ca. 2016 and 2018, at the latter area.

PSP-producing species also showed a unimodal annual cycle, with maxima during late-winter or spring (March-May; Fig. 3.19). For this group, abundance exceeded the threshold alert level (500 cells L^{-1}) between 1% and 5% of cases, at L6 and L8, respectively (Fig. 3.22).

HY-producers were more abundant during late-spring and summer (June-August), for all areas, reflecting a unimodal annual cycle (Appendix D.1). This group was still present in early autumn (October) at L7c and L9, disappearing afterwards. Regulatory alert level for this group (1.000 cells L^{-1}) was exceeded at L7c (2018 and 2019, 1% samples), L8 and L9 areas (2014, 2018 and 2019; 1% and 3% samples, respectively), but never exceeded at L6 and L7a areas (Fig. 3.23). During 2018, the bloom event apparently spread westwards along the south coast, while during 2019, the bloom event affected all production areas (see Fig. 3.23).

The influence of physical oceanographic regimes on the abundance of HAB-forming taxa was analysed using CSET (L6, L7a, L7c areas) and the along-shore current velocity (L8, L9 areas) as upwelling indices (see Fig. 3.24). For L6 area, ASP- and DSP-producers showed similar mean abundances and variability for upwelling and mixed regimes. Higher abundances of PSP-producing species were detected under downwelling-favourable conditions. At L7a, ASP and DSP-producers showed a higher variability during upwelling favourable-periods, although no differences were detected between physical regimes for any HAB group. For the south-westernmost area (L7c), mean abundances of ASP and DSP-producing species were more variable under mixed regimes. For PSP-producers, higher mean abundances and variability were observed during upwelling periods in respect with downwelling and mixed conditions ($p < 0.05$; Fig. 3.24). HY-producers were only detected under mixed conditions (Appendix D.2). At L8 area, ASP-producers showed higher variability under mixed conditions.

Mean abundance of DSP-producers was similar between upwelling and downwelling-favourable regimes, but more variable under downwelling-favourable regimes. In turn, PSP-producers exhibited higher variability in upwelling-favourable regimes. In this area, HY-producers were only detected during downwelling-favourable conditions (Appendix D.3). For the south-easternmost area (L9), the abundance of PSP- and DSP-producers was more variable under downwelling-favourable regimes and, for the latter group, mean abundance was also higher under these conditions. By contrast, ASP-producers showed a higher variability during upwelling-favourable periods (Fig. 3.24). As for other bivalve production areas, HY-producers were only detected under downwelling-favourable regimes (Appendix D.4).

As for phytoplankton biomass, the influence of physical oceanographic regimes on the abundance of four different HAB groups (ASP, DSP, PSP and HY producers) was also investigated for specific seasons, using CSET (L6, L7a, L7c areas) and along-shore current velocity (L8, L9 areas) as upwelling indices (Fig. 3.25). In respect with mixed conditions, the abundance of ASP-producers was lower under winter upwelling-favourable (L7c) and autumn downwelling-favourable periods ($p < 0.05$; L8). Also, during autumn, higher ASP abundance was observed under upwelling-favourable compared with downwelling-favourable regimes (L9). DSP-producers were more abundant under mixed conditions in respect with summer downwelling-favourable periods (L6) or winter upwelling-favourable periods (L7c). Higher abundances of PSP-producers were detected either under upwelling compared with mixed regimes during spring (L7c), or vice-versa during winter (L8). Also, higher abundances of PSP-producers were recorded during upwelling conditions, compared to the other regimes, during autumn (L7c). For HY-producers, no differences between physical oceanographic regimes were detected for any season (Appendix D.5).

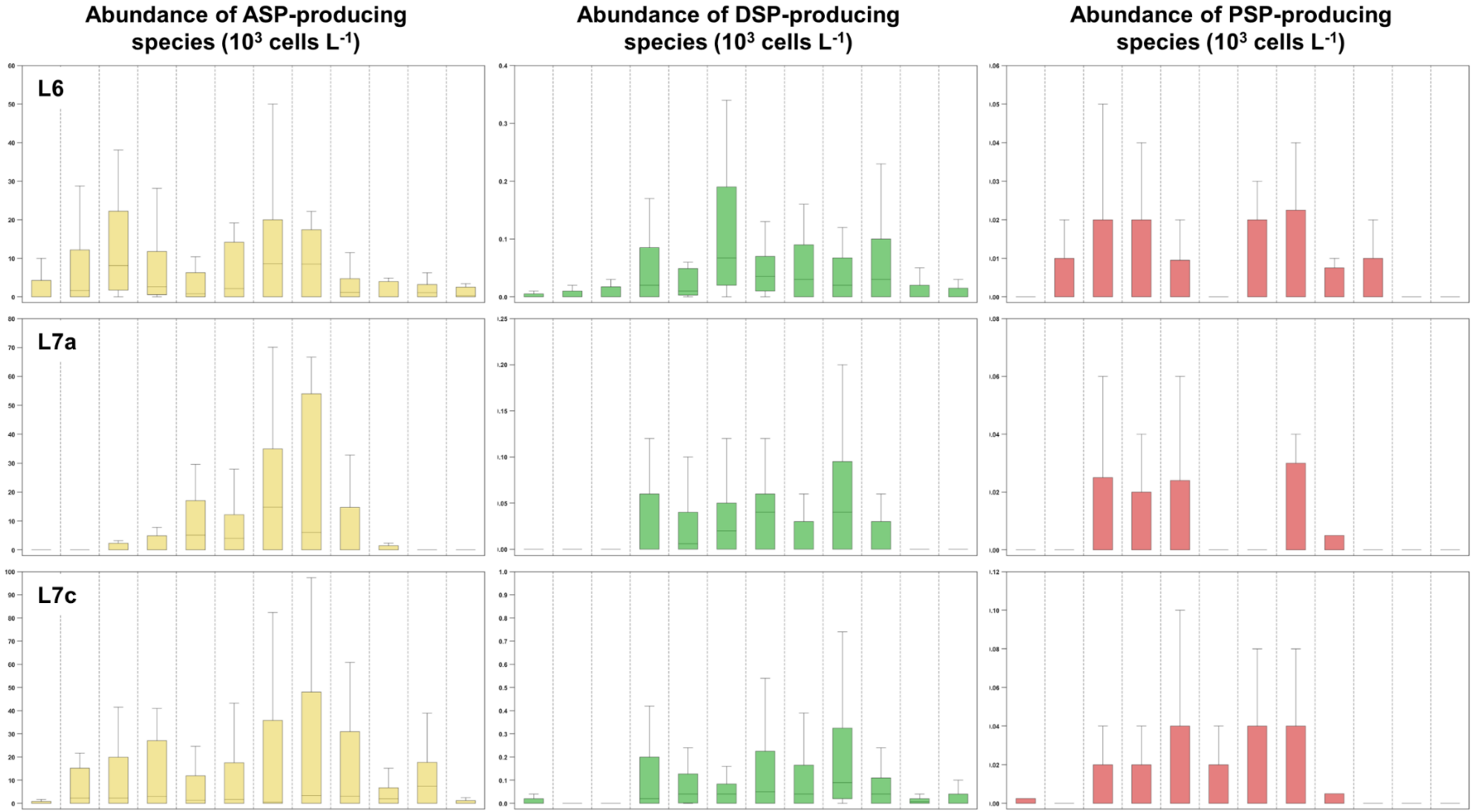
Abundance of ASP-producing species (10^3 cells L^{-1})
Abundance of DSP-producing species (10^3 cells L^{-1})
Abundance of PSP-producing species (10^3 cells L^{-1})
L6
L7a
L7c

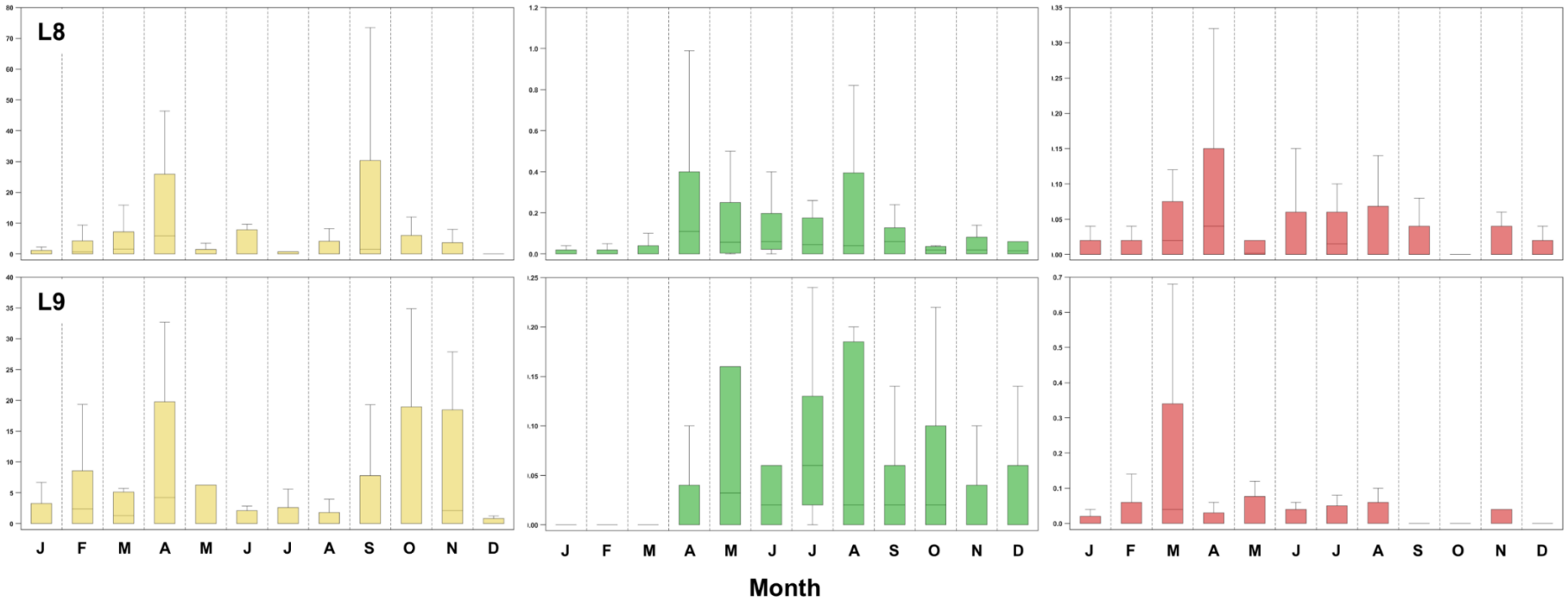

Figure 3.19 – Monthly variability of the abundance of ASP (Amnesic Shellfish Poisoning), DSP (Diarrhetic Shellfish Poisoning) and PSP (Paralytic Shellfish Poisoning) producing species, represented by yellow, green and red colors, respectively, for different coastal bivalve production areas (L6, L7a, L7c, L8, L9), during the period 2014-2019. Median values are identified by the central line within the box, the bottom and top edges of the box indicate the 25th and 75th percentiles, respectively, and the whiskers represent non-outlier limits. Note differences in scale between harmful algal bloom (HAB) groups. See Figure 2.1 for site/area location.

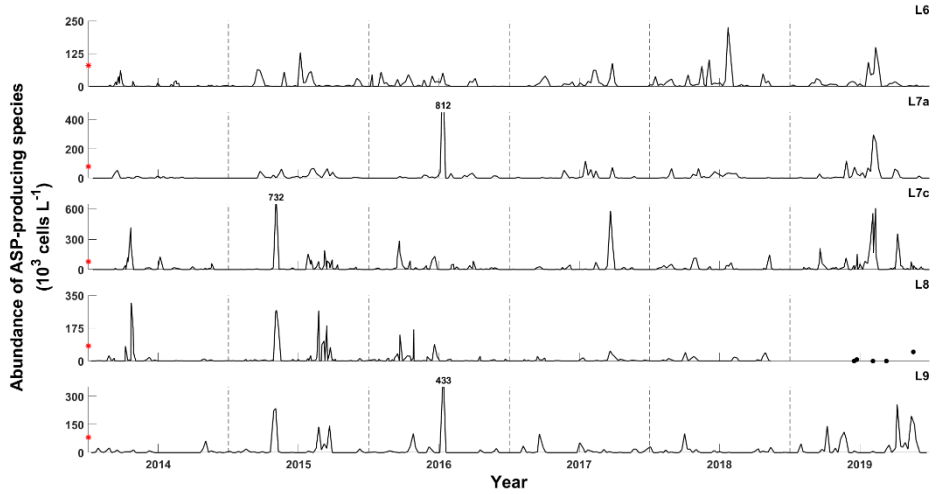

Figure 3.20 – Time series of the abundance of Amnesic Shellfish Poisoning (ASP)-producing species, for different coastal bivalve production areas (L6, L7a, L7c, L8, L9), during the period 2014-2019. Numbers associated with peaks correspond to extreme out-of-scale observations. The red asterisk signals the minimum regulatory alert level for this harmful algal bloom (HAB) group (80000 cells L^{-1}). See Figure 2.1 for site/area location.

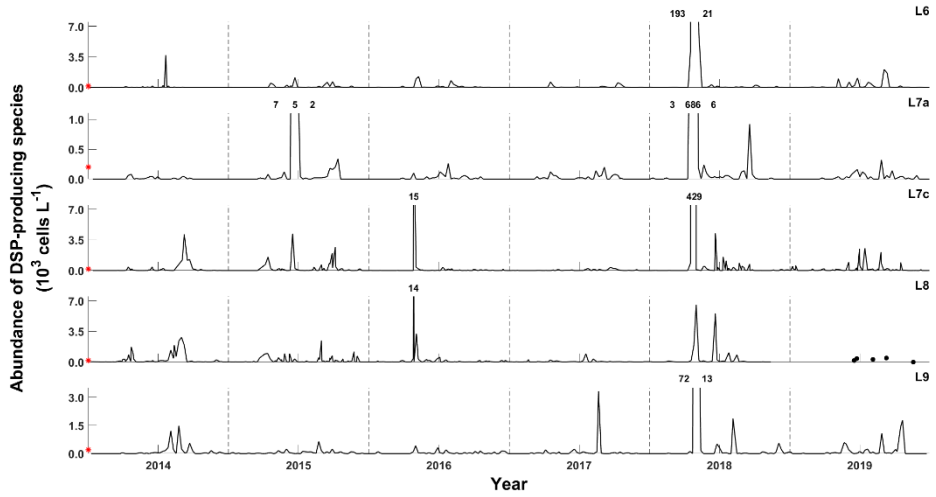

Figure 3.21 – Time series of the abundance of Diarrhetic Shellfish Poisoning (DSP)-producing species, for different coastal bivalve production areas (L6, L7a, L7c, L8, L9), during the period 2014-2019. Numbers associated with peaks correspond to extreme out-of-scale observations. The red asterisk signals the minimum regulatory alert level for this harmful algal bloom (HAB) group (200 cells L^{-1}). See Figure 2.1 for site/area location.

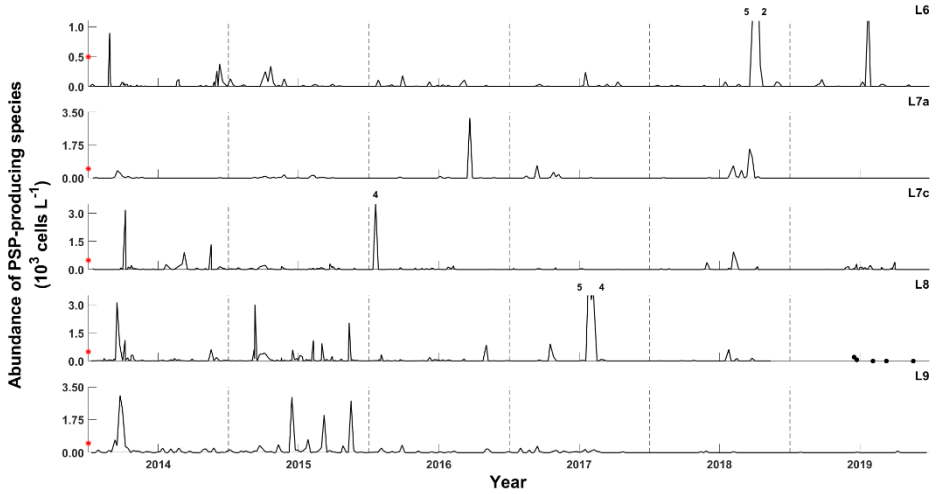

Figure 3.22 – Time series of the abundance of Paralytic Shellfish Poisoning (PSP)-producing species, for different coastal bivalve production areas (L6, L7a, L7c, L8, L9), during the period 2014-2019. Numbers associated with peaks correspond to extreme out-of-scale observations. The red asterisk signals the regulatory minimum alert level for this harmful algal bloom (HAB) group (500 cells L^{-1}). See Figure 2.1 for site/area location.

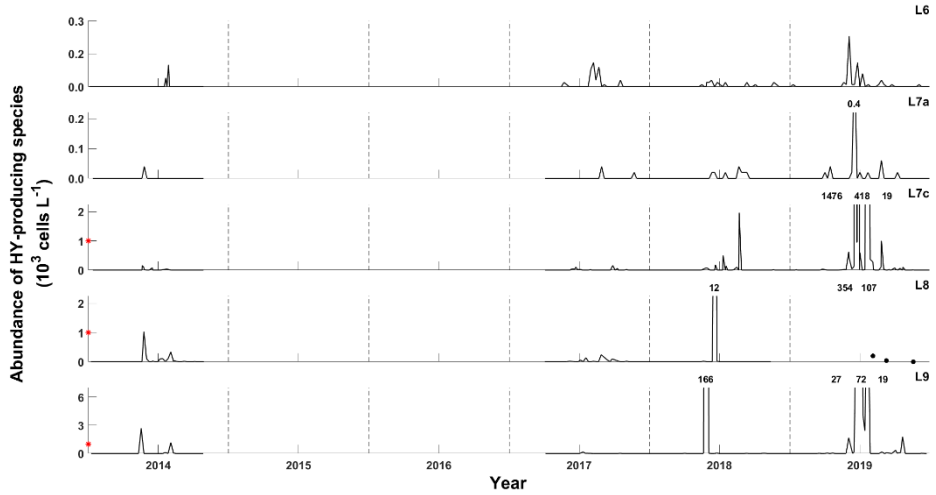

Figure 3.23 – Time series of the abundance of Homoyesso- and Yessotoxin (HY)-producing species, for different coastal bivalve production areas (L6, L7a, L7c, L8, L9), during the period 2014-2019. Numbers associated with peaks correspond to extreme out-of-scale observations. The red asterisk signals the minimum alert level for this harmful algal bloom (HAB) group (1 000 cells L^{-1}). See Figure 2.1 for site/area location.

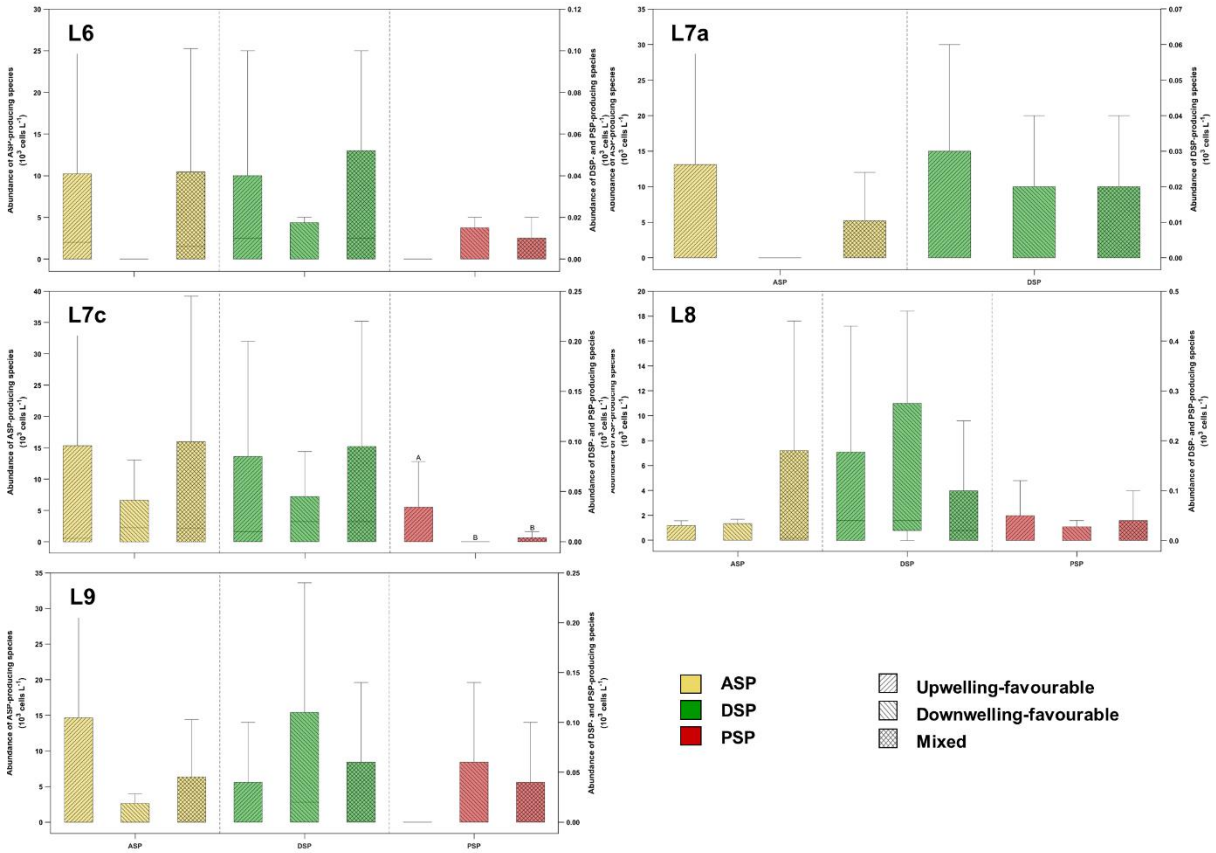

Figure 3.24 - Variability of the abundance of ASP (Amnesic Shellfish Poisoning), DSP (Diarrhetic Shellfish Poisoning) and PSP (Paralytic Shellfish Poisoning)-producing species, represented by yellow, green and red colors, respectively, in five shellfish production areas (L6, L7a, L7c, L8, L9), binned into three different physical regimes: upwelling-favourable (single line bending upwards), downwelling-favourable (single line bending downwards) and mixed (crossed lines). Physical regimes were defined using the cross-shore Ekman transport (L6, L7a, L7c) and the along-shore current velocity (L8, L9). Note differences in scale between harmful algal bloom (HAB) groups. Median values are identified by the central line within the box, the bottom and top edges of the box indicate the 25th and 75th percentiles, respectively, and the whiskers represent non-outlier limits. For each group, different uppercase letters over the bars denote significant differences between physical regimes ($p < 0.05$). See Figure 2.1 for site/area location.

3.3.2 Harmful algal bloom phenology

Basic statistical information on phenological indices for different HAB-groups and bivalve production areas (L6, L7a, L7c, L8, L9), during the 6-year study period, is summarized in Tables F.2-F.4. DSP, ASP and PSP represented 43%, 41% and 16%, respectively, of all bloom events (total: 128 events). Overall, the number of ASP and DSP blooms was higher compared with PSP blooms ($p < 0.05$; Fig. 3.26A-B). The mean number of blooms of ASP-producers per year ranged from one (L7c, L8) to three (L6), with higher bloom frequency at L6 compared with L7c and L8 areas ($p < 0.05$). By contrast, no differences across areas were detected in the number of blooms per year for DSP and PSP-producers (on average, two and one bloom per

year, respectively). The average duration of PSP blooms was shorter in respect to ASP and DSP blooms ($p < 0.05$; Fig. 3.26C-D). For ASP blooms, average bloom duration varied from three (L7c, L8, L9) to five (L7a) weeks , whereas DSP and PSP blooms persisted, on average, for four and two weeks, respectively. PSP-producers displayed the shortest total bloom duration per year compared with the remaining groups ($p < 0.05$; Fig. 3.26E-F). Total duration of all bloom events per year caused by ASP-producing species ranged, on average, from four (L8) to 12 weeks (L6), with a longer duration observed at L6 in respect to L8 area ($p < 0.05$), reflecting variability in bloom frequency. In turn, DSP and PSP blooms extended, on average, over seven and two weeks each year, respectively (at L7c). Considering peak abundance, ASP and PSP-producers reached the highest and lowest mean peak values, respectively ($p < 0.05$; Fig. 3.26G-H). For ASP-producing species, mean peak abundance varied from $6.2x10^4 \pm 3.8x10^4$ cells L^{-1} to $1.5x10^5 \pm 1.9x10^5$ cells L^{-1} at L6 and L7c, respectively. Peak values for DSP and PSP-producers, which showed no differences among production areas, averaged $2.4x10^4$ cells L^{-1} and 531 cells L^{-1}.

DSP-producers showed delayed onset and peak timings with respect to PSP-producers, while no differences were detected regarding ASP-producers ($p < 0.05$; Fig. 3.26I-L). For ASP-producing species, mean bloom initiation occurred during May (WOY: 16-19; Fig. 3.26J), the peak was attained from May to June (WOY: 18-21; Fig. 3.26L), and termination from June to July (WOY: 20-25; Table F.2 and Appendix F.2). DSP-producers presented delayed bloom timings, with mean initiation in mid-June (WOY: 22; Fig. 3.26I), peak timing in July (WOY: 24; Fig. 3.26K), and ending from June to August (WOY: 21-31), with delayed termination timing at L6 compared to L8 area ($p < 0.05$; Table F.3 and Appendix F.2). Blooms associated with PSP-producing species initiated, on average, in early-May (WOY: 16; Fig. 3.26I), peaked in mid-May (WOY: 18; Fig. 3.26K), and terminated during June (WOY: 21; Table F.4 and Appendix F.2). Considering both accumulation and deceleration phases, blooms of PSP-producers exhibited a shorter mean duration compared with ASP and DSP-producers ($p < 0.05$; Fig. 3.26M-P). However no differences in bloom onset and peak timings, and duration of accumulation and deceleration phases, were detected across production areas, for any HAB group. The mean duration of ASP blooms accumulation phase ranged, on average, from two (L7a, L7c, L8, L9) to three weeks (L6), while for DSP and PSP blooms, this bloom phase lasted for two and one week, respectively (Fig. 3.26M-N). The deceleration phase of ASP blooms varied from two (L7c) to four weeks (L7a), averaging three and two weeks for DSP and PSP blooms, respectively (Fig. 3.26O-P).

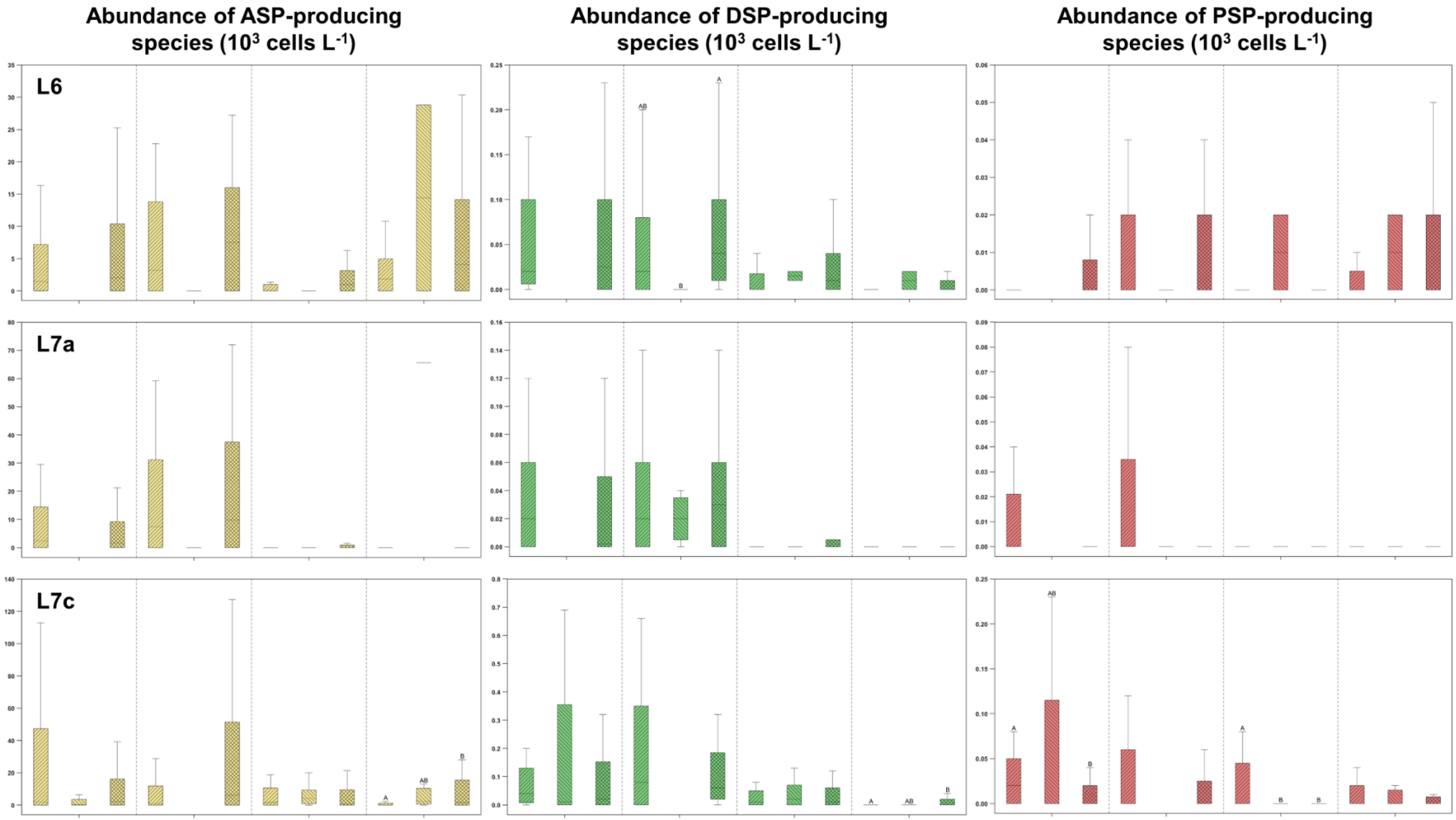
Abundance of ASP-producing species (10^3 cells L^{-1})
Abundance of DSP-producing species (10^3 cells L^{-1})
Abundance of PSP-producing species (10^3 cells L^{-1})
L6
L7a
L7c

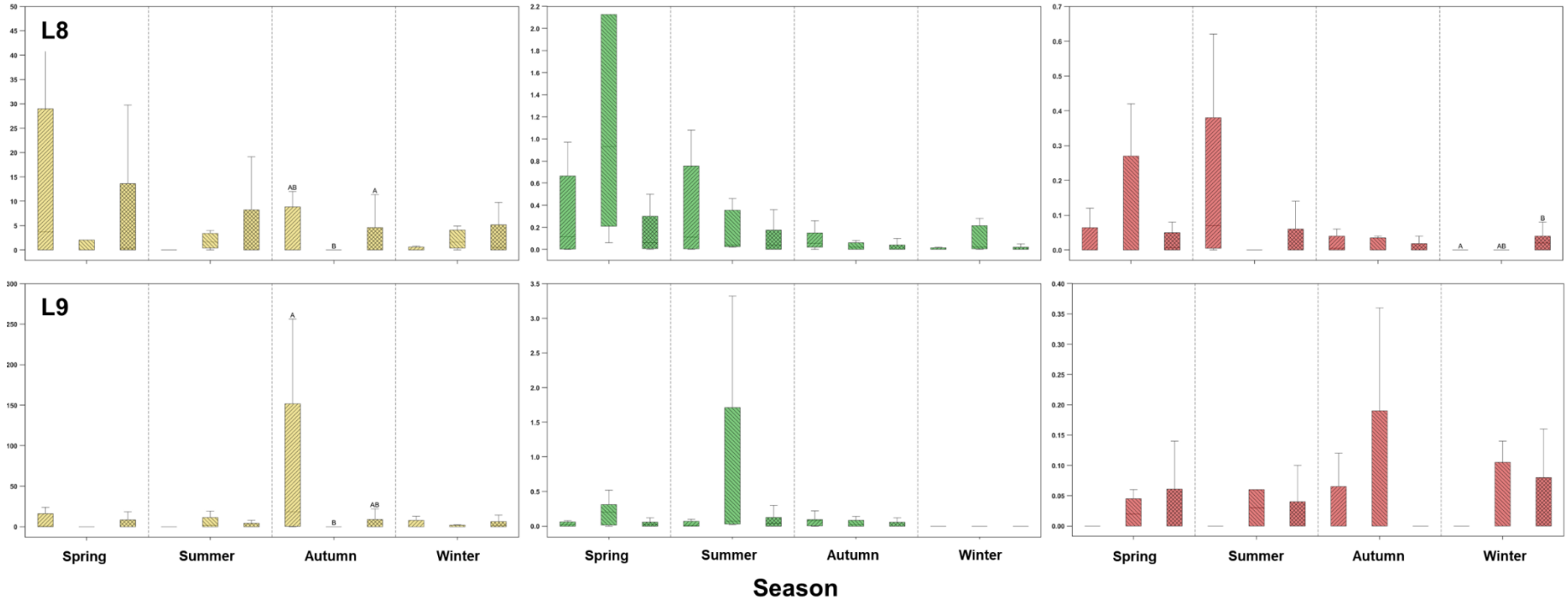

Figure 3.25 - Variability of the abundance of ASP (Amnesic Shellfish Poisoning), DSP (Diarrhetic Shellfish Poisoning) and PSP (Paralytic Shellfish Poisoning)-producing species, represented by yellow, green and red colors, respectively, for different coastal bivalve production areas (L6, L7a, L7c, L8, L9) binned into three different physical regimes: upwelling-favourable (single line bending upwards), downwelling-favourable (single line bending downwards) and mixed (crossed lines), for the four seasons of the year. Note differences in scale between harmful algal bloom (HAB) groups. Median values are identified by the central line within the box, the bottom and top edges of the box indicate the 25th and 75th percentiles, respectively, and the whiskers represent non-outlier limits. For each area, different uppercase letters over the bars denote significant differences between physical regimes within each season. See Figure 2.1 for location of areas.

3.3.3 Environmental drivers of harmful algal blooms

For ASP models, the most significant predictors differed across production areas, and model explanatory power varied from 7 to 8% (Fig. 3.27 and Table E.2). At L6 area, SST was the predictor with the highest partial effect on the abundance of ASP-producers, showing a negative non-linear influence for SST values above ca. 18 ºC. Chl-a exerted a positive linear influence, with positive ASP anomalies for Chl-a above ca. 0.6 µg L^{-1}. At L7a, PAR presented a positive linear effect, with positive ASP anomalies for PAR values above ca. 500 µmol photons m^{-2} s^{-1}. For L7c-L8 areas, MLD was the most significant predictor, followed by SST, both showing non-linear negative effects over the abundance of ASP-producers. MLD values below ca. 20 m, and SST below ca. 20ºC were associated with positive anomalies in ASP abundance. Guadalquivir river discharge appeared also as a strong predictor of ASP-producers ($p < 0.01$) with *quasi* linear negative effects, for L7c-L8 areas. At L9, along-shore current velocity and Guadiana river discharge were the most important predictors, although less significant compared with environmental predictors from other production areas ($p < 0.05$). Along-shore current velocity exerted a positive linear influence on the abundance of ASP-producers, while Guadiana river discharge presented a negative *quasi* linear effect, with a low positive anomaly in ASP abundance for river discharge below ca. 20 m^3 s^{-1} (Fig. 3.27).

The most relevant predictors of the abundance of DSP-producers also differed across bivalve production areas, but the explanatory power of DSP models was higher compared with ASP models (Fig. 3.28 and Table E.3). The percentage of variance explained by DSP increased from north to south along the west Portuguese coast (L6, L7a; 36-54%) and, along the south coast, decreased eastwards (L7c-L8, L9; 21- 36%). DSP-producers at L6 and L7a areas presented three common environmental predictors, PAR, MLD and SST. Over L6 area, PAR was the most important predictor, with positive non-linear partial effects for values below ca. 600 µmol photons m^{-2} s^{-1}, and negative effects for higher values. MLD was the second most influential predictor, followed by SST, both showing linear negative effects on DSP abundance. Positive anomalies in DSP-producers were associated with MLD values below ca. 20 m, and SST values below ca. 16 ºC. CSET, a less influential predictor ($p < 0.01$), showed a non-linear positive effect, with positive DSP anomalies associated with low (positive) CSET values, representative of downwelling periods. (Fig. 3.28). At L7a area, the most significant predictor of DSP-producers was Chl-a, with non-linear positive effects for Chl-a values from 0.3 to 0.6 µg L^{-1}, and negative effects for higher Chl-a values. MLD showed non-linear negative effects on DSP abundance, for MLD values below ca. 60 m. Partial effects of PAR were non-linear,

with a negative influence for PAR between 300-400 µmol photons m^{-2} s^{-1}, and a positive influence for higher values. SST was the least significant predictor for L7a area, showing partial negative effects for values up to 18 ºC, and positive effects for higher SST (Fig. 3.28).

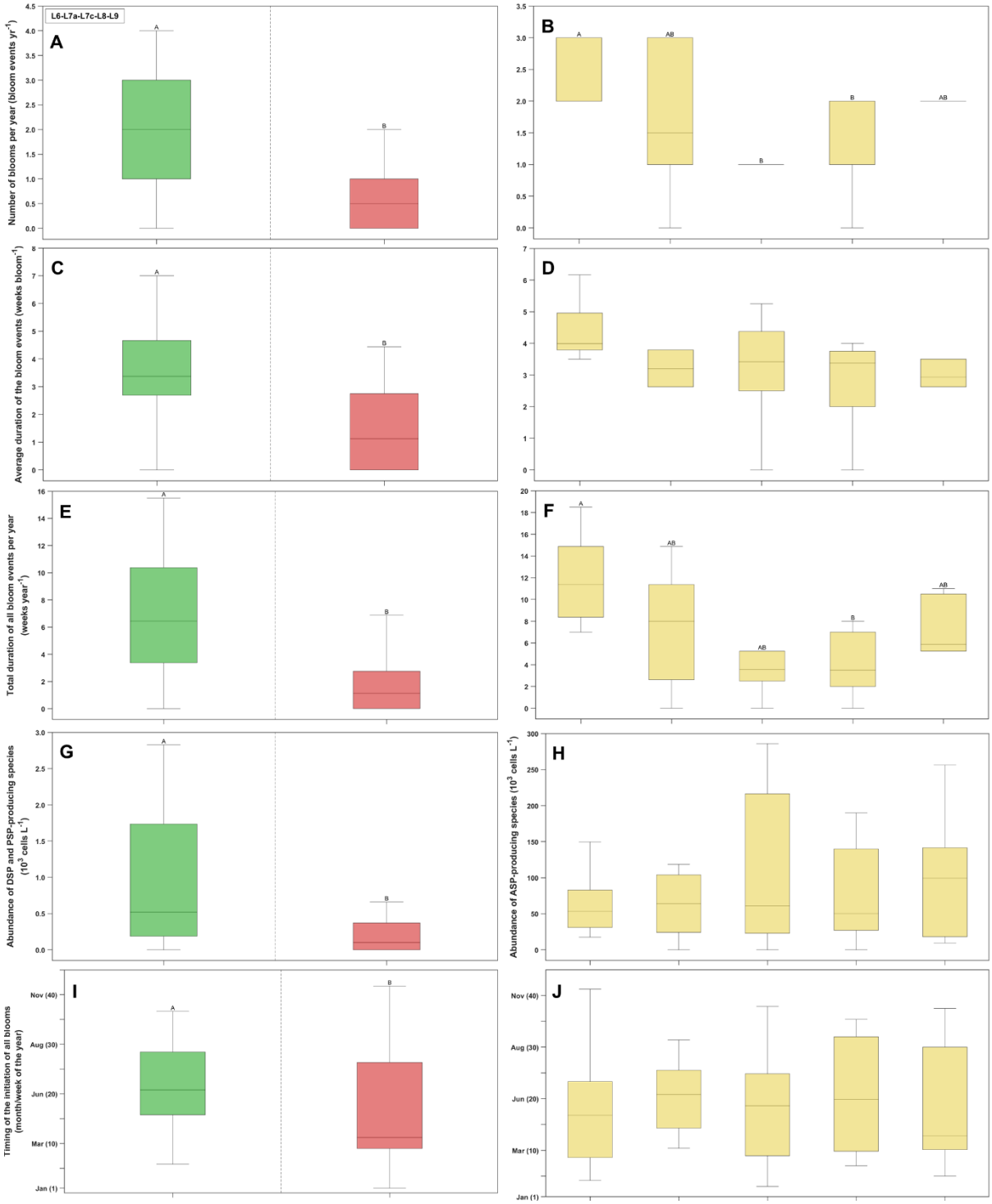

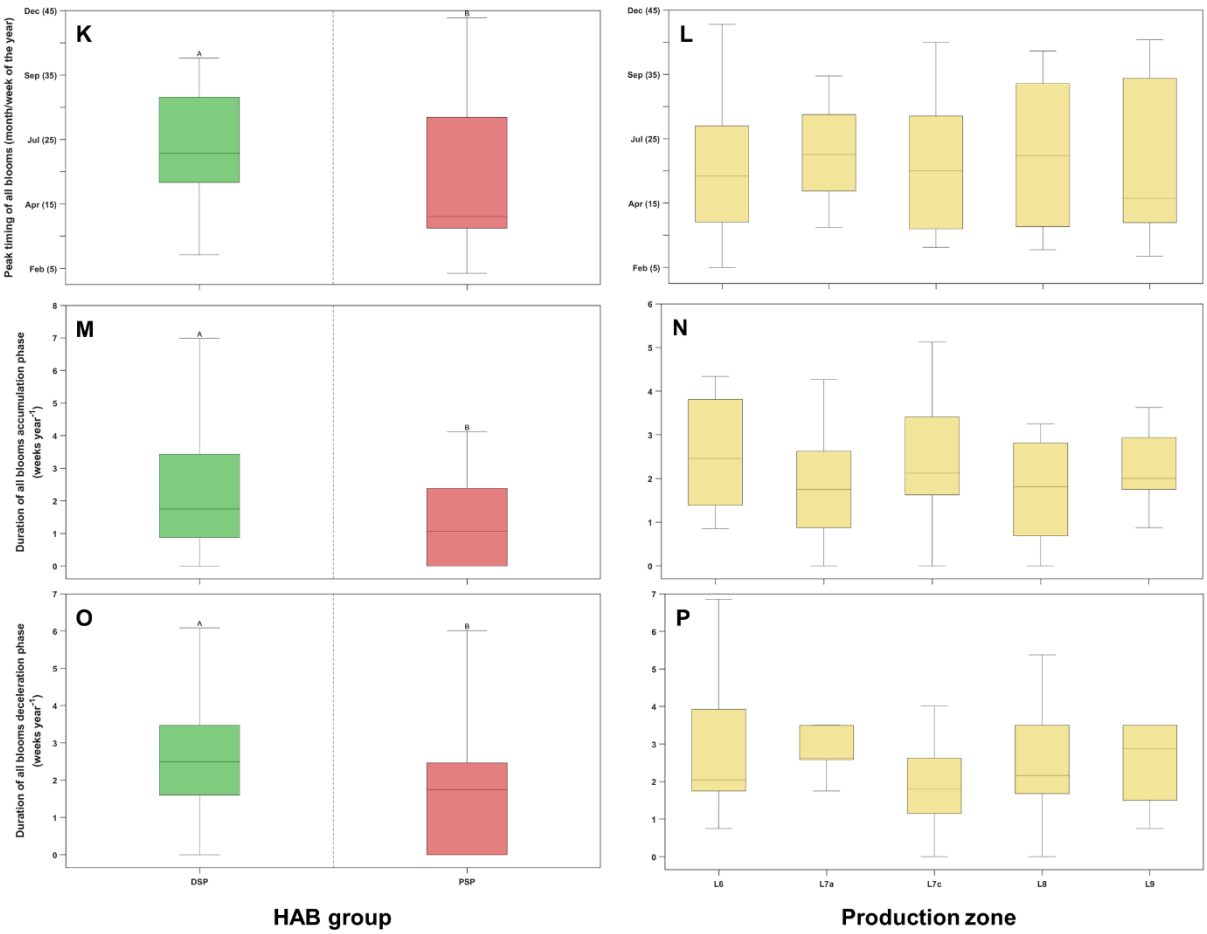

Figure 3.26 - Phytoplankton phenological indices for the three most frequently reported toxin-producing groups (Amnesic Shellfish Poisoning – ASP, Diarrhetic Shellfish Poisoning – DSP, and Paralytic Shellfish Poisoning – PSP, represented by yellow, green and red colors, respectively), over different coastal bivalve production areas (L6, L7a, L7c, L8, L9), during the period 2014-2019. The left column includes information for DSP and PSP-producers, groups with no differences in most phenological indices between production areas ($p>0.05$), and right column includes ASP-producers that exhibited differences between areas. Phenological indices: (A, B) Number of blooms per year; (C, D) Average duration of bloom events; (E, F) Total duration of all bloom events per year; (G, H) Peak abundance of toxin-producing species; (I, J) Bloom initiation timing; (K, L) Bloom peak timing; (M, N) Duration of bloom accumulation phase; and (O, P) Duration of bloom deceleration phase. Median values are identified by the central line within the box, the bottom and top edges of the box indicate the 25th and 75th percentiles, respectively, and the whiskers represent non-outlier limits. For each phenological index and HAB group, different uppercase letters over the bars denote significant differences across groups (see left column) or regions (see right column; $p < 0.05$). See Figure 2.1 for designation and location of specific production areas.

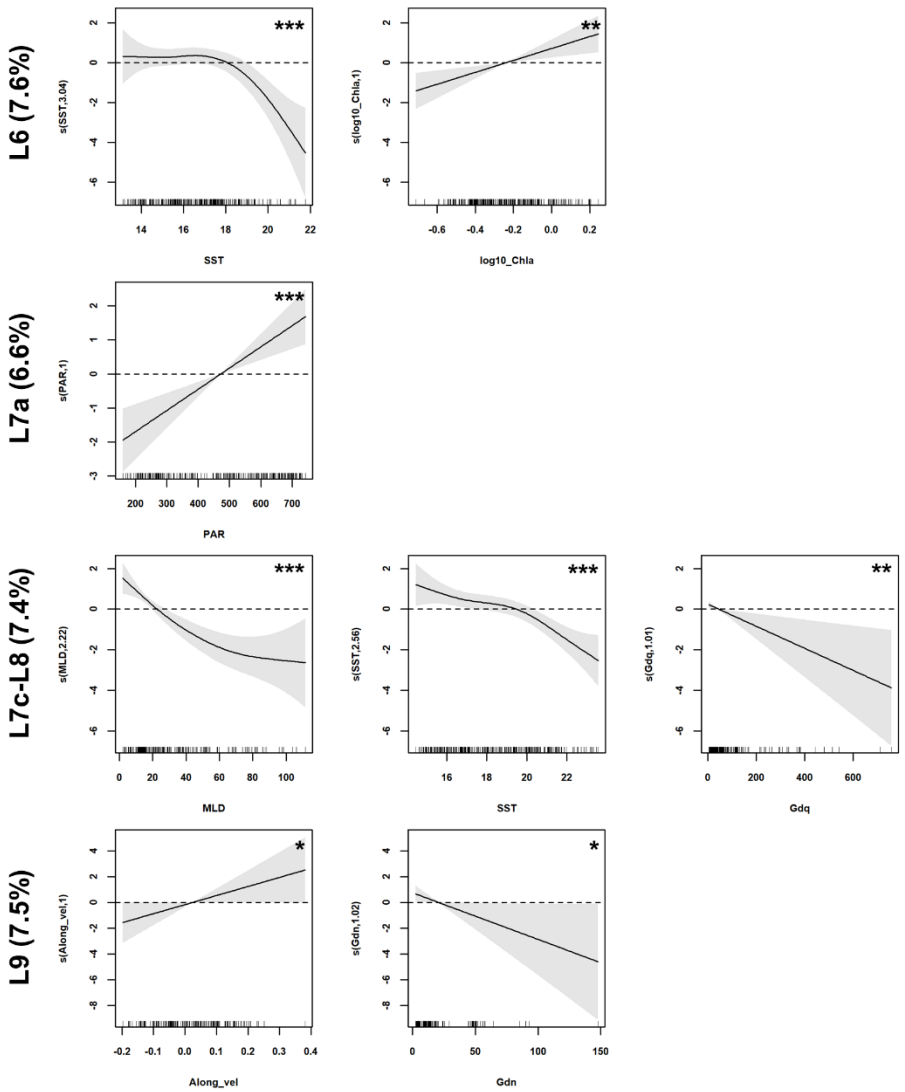

Figure 3.27 - Partial effects of individual environmental predictors on the abundance of Amnesic Shellfish Poisoning (ASP) producers, for each bivalve production area, during the period 2014-2019, derived from the best performing generalized additive models (GAM). Region-specific model explanatory power (as % of ASP variance explained) is presented in brackets after region abbreviation; the set of plots for each region is organized in descending order of their explanatory power, and the significance level (p-value) of each predictor is denoted by asterisk symbols (top right), where *, **, *** indicate p-value <0.05, <0.01 and <0.001, respectively. Solid lines represent the fitted models, and grey shaded areas depict 95% confidence intervals. Short vertical lines on the x-axis represent the actual predictor observations, and values on the y-axis denote the effective degrees of freedom (edf). Edf values of 1 represent a linear effect of the predictor on the abundance of ASP-producers, and values higher than 1 indicate non-linear effects. Positive (negative) y-values indicate a positive (negative) influence on the abundance of ASP producers. See Figure 2.1 for designation and location of specific production areas.

Along the south Portuguese coast, and for L7c-L8 areas, PAR was the most relevant predictor of DSP-producers, with positive non-linear effects for PAR up to ca. 600 µmol photons m^{-2} s^{-1}. Chl-a showed a positive influence up to ca. 0.3 µg L^{-1}, and a negative influence for higher values. As referred for ASP-producers, Guadalquivir river discharge was also a

significant predictor of DSP-producers for this production area ($p < 0.01$), with a small positive influence for river discharge below ca. 200 m^3 s^{-1}, and a negative influence for higher discharges. Along-shore current velocity exhibited non-linear negative effects on DSP abundance (Fig. 3.28). Over L9 bivalve production area, similarly to L6 and L7c-L8, PAR was the most influential predictor, showing linear positive effects, with positive DSP anomalies associated with PAR values above ca. 500 µmol photons m^{-2} s^{-1}. Guadiana river discharge and alongshore current velocity were also relevant but less significant predictors ($p < 0.05$). Guadiana discharge presented linear negative effects on DSP-producers, and alongshore current velocity exhibited non-linear positive effects, intensified during upwelling conditions (positive along-shore velocity).

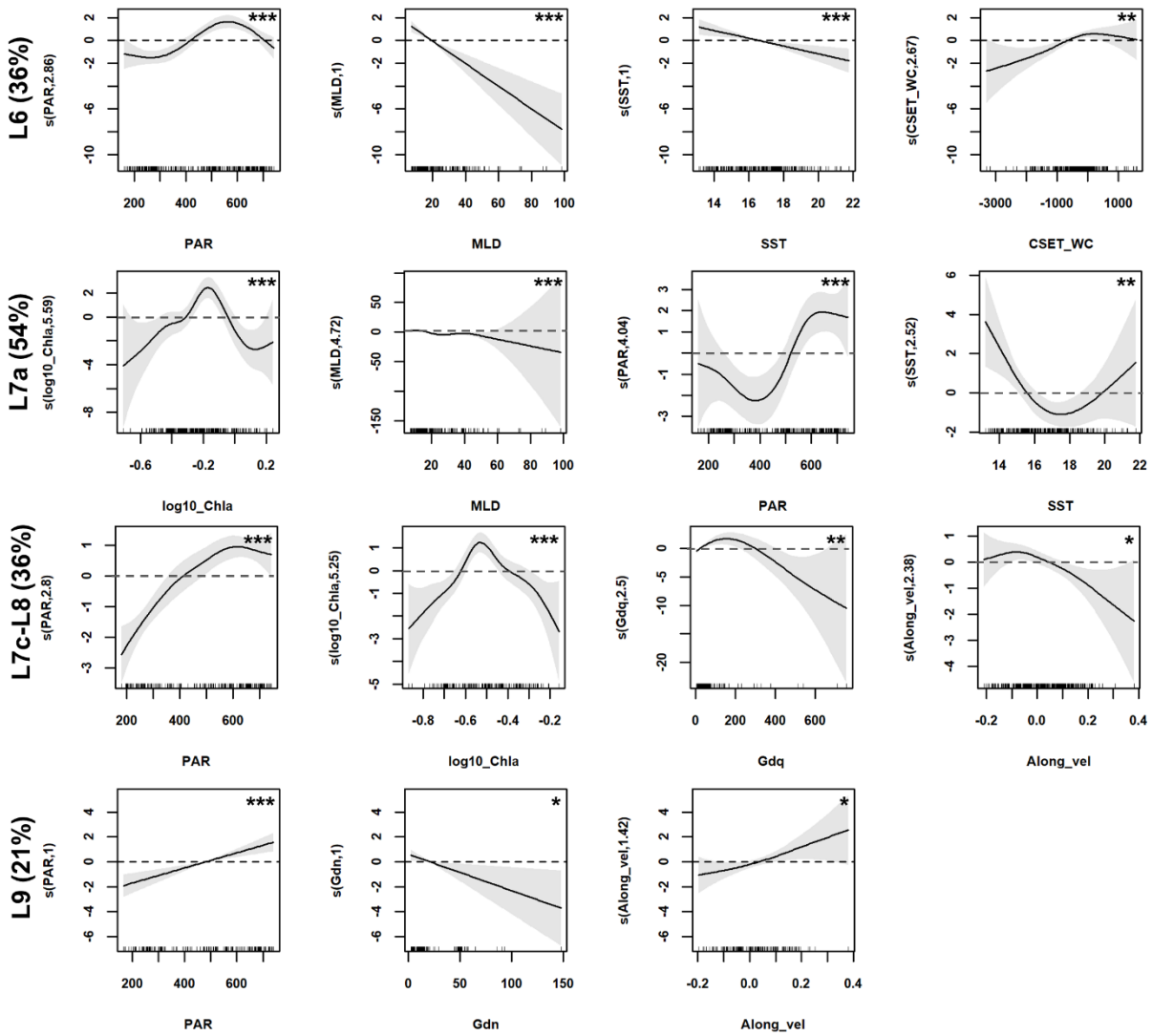

Figure 3.28 – Partial effects of individual environmental predictors on the abundance of Diarrhetic Shellfish Poisoning (DSP) producers, for each bivalve production area, during the period 2014-2019, derived from the best performing generalized additive models (GAM). Region-specific model explanatory power (as % of DSP variance explained) is presented in brackets after region abbreviation; the set of plots for each region is organized in descending

order of their explanatory power, and the significance level (p-value) of each predictor is denoted by asterisk symbols (top right), where *, **, *** indicate p-value <0.05, <0.01 and <0.001, respectively. The solid line is the fitted model and grey shaded areas represent the 95% confidence intervals. The short vertical lines on the x-axis represent the actual predictor observations, and the values on the y-axis denote the effective degrees of freedom (edf). Edf values of 1 represent a linear effect of the predictor on the abundance of DSP-producers, and values higher than 1 indicate non-linear effects. Positive (negative) y-values indicate a positive (negative) influence on the abundance of DSP producers. See Figure 2.1 for designation and location of specific production areas.

3.4 Phycotoxins in bivalve molluscs

Overall, the number of days of full or partial bivalve harvest interdiction caused by toxin concentrations above regulatory levels (see Annex A.3), during the study period (1 January 2015 – 31 December 2019), was lower at L7a area (47 days), intermediate at L7c (612 days) and L9 (738 days), and higher at L8 (1192 days) and L6 production areas (1268 days; data not shown).

Average concentration of ASP toxin, domoic acid (DA), in the most recurrently surveyed bivalve species in the study area ranged between 2.3 ± 0.6 mg DA/kg and 1.6 ± 1.0 DA mg/kg in *Mytilus* spp. and *Donax trunculus*, respectively (see Table 3.2). Mean concentration of DSP toxin, okadaic acid (OA), was 125.4 ± 33.7 µg OA equiv/kg in *Mytilus* spp., and 197.9 ± 10.7 µg OA equiv/kg in *Donax trunculus*. Average concentration of PSP toxin, saxitoxin (STX), was 168.0 µg STX equiv/kg in *Mytilus* spp., and 155.3 µg STX equiv/kg in *Donax trunculus*. For ASP and DSP-toxins in these bivalve species, no differences were observed across production areas (Fig. 3.29; ASP: data not shown). Thus, for subsequent analysis, data from all areas were combined for these toxins (*Mytilus* spp.: L6-L7a-L7c-L8; and *Donax trunculus*: L6-L7c-L8-L9).

Mean STX concentration in *Mytilus* spp. ranged from 82.2 ± 218.5 µg STX equiv/kg to 264.6 ± 1460.7 µg STX equiv/kg, at L7c and L6, respectively, and higher concentrations were detected at L7a (similar to L7c) with respect to L8 area ($p < 0.05$; Fig. 3.29). For *Donax trunculus*, mean STX levels varied from 62.6 ± 176.1 µg STX equiv/kg to 422.5 ± 796.5 µg STX equiv/kg, at L9 and L6, correspondingly, and higher concentrations were detected at L6 area ($p < 0.05$; Fig. 3.29). Thus, for subsequent analysis, PSP-toxin data were aggregated into two groups of production areas: L6, L7a-L7c, and L8 for *Mytilus* spp., and in L6, L7c-L8-L9 for *Donax trunculus*.

In respect with temporal variability, DA was detected in *Donax trunculus* only during the month of April, while in *Mytilus* spp., either null or extreme concentrations were present throughout the year (data not shown). The regulatory level for ASP toxins (20 mg DA/kg) was exceeded at L7c (0.5% samples) and L9 (0.4% samples) areas in *Mytilus* spp. and *Donax trunculus*, respectively. Also, for both species, this threshold concentration was surpassed during the winter-spring transition in 2019, which might reflect the influence of the same bloom event, affecting the two species (Fig. 3.30). Relatively low positive relationships between the abundance of ASP-producers and DA concentration in bivalves were detected only over the western production areas (L6, L7a), for *Mytilus* spp. (N = 94-108, p <0.05; see Appendices, Table G.1).

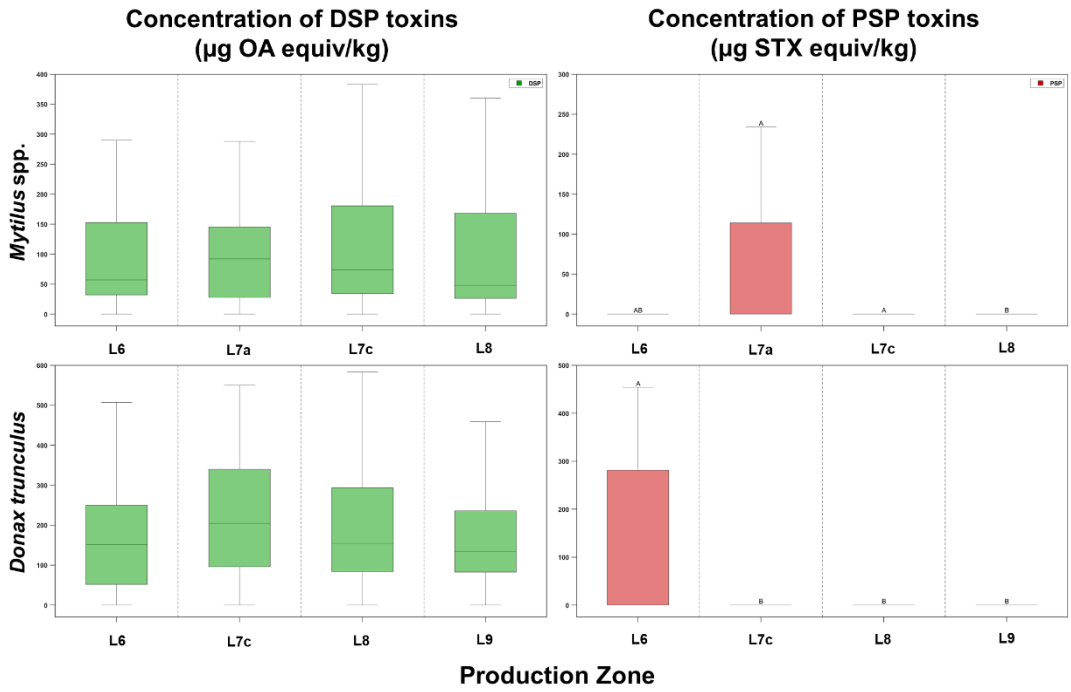

Figure 3.29 - Variability of the concentration of okadaic acid (OA) and saxitoxin (STX), represented by green and red colors, respectively, in two of the most recurrently surveyed bivalve species (*Mytilus* spp. and *Donax trunculus*), for different coastal bivalve production areas (L6, L7a, L7c, L8, L9) during the period 2014-2019. Domoic acid (DA) concentration was not represented due to the limited data available. Median values are identified by the central line within the box, the bottom and top edges of the box indicate the 25th and 75th percentiles, respectively, and the whiskers represent non-outlier limits. For each biotoxin group and bivalve species, different uppercase letters over the bars denote significant differences across regions ($p < 0.05$). See Figure 2.1 for designation and location of specific production areas.

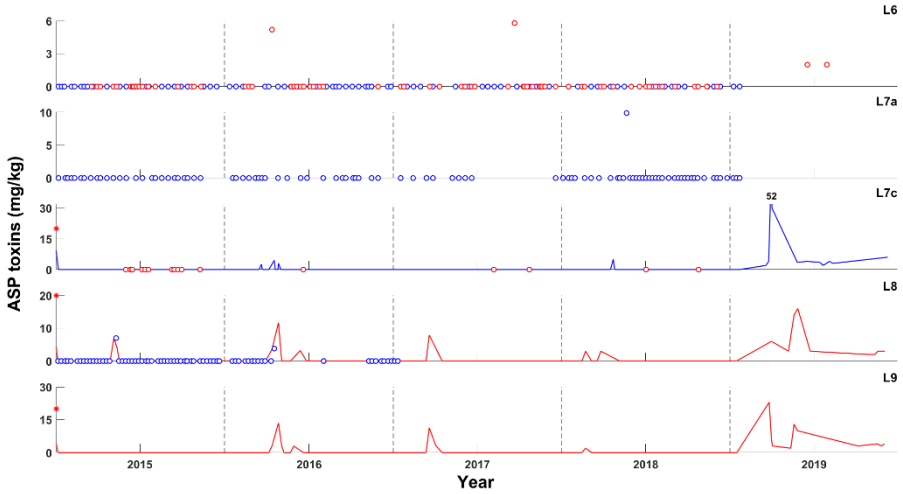

Figure 3.30 – Weekly time series of the concentration of domoic acid (DA) in two bivalve species, for different coastal bivalve production areas (L6, L7a, L7c, L8, L9), during the period 2014-2019. Blue and red colors represent the toxin content in *Mytilus* spp. and *Donax trunculus*, respectively. Numbers associated with peaks correspond to extreme out-of-scale observations. For areas and/or bivalve species with a reduced dataset, circle markers in the corresponding color were used for a more accurate representation. Red asterisks (see y-axis) signal the regulatory level for the ASP-toxin group in bivalves (20 mg DA kg^{-1}). See Figure 2.1 for site/area location.

OA concentration displayed similar intra-annual patterns for both bivalve species, i.e., a bimodal annual cycle, with peaks in summer (June-July) and autumn (October; Fig. 3.31), with higher concentrations for *Donax trunculus* than *Mytilus* spp. The regulatory level for DSP toxins in bivalves (160 µg OA equiv/kg) was exceeded almost continuously at all production areas, with the highest proportion of samples above the threshold detected over L8 area (33%), in *Donax trunculus* (Fig. 3.32). Overall, positive relationships between the abundance of DSP-producers and OA concentration in bivalves were detected for all production areas (N = 56-188, $p < 0.05$), except for L7c (N = 9, see Table G.1).

STX concentration for all production areas except L8, and both species, was higher during the autumn-winter period, with a maximum between October and December months (Fig. 3.33). At L8 area, these toxins were observed in bivalves only during spring (April - May). The regulatory level for PSP toxins (800 µg STX equiv/kg) was only exceeded in few samples (between 0.3 % at L8, and 5% at L6, in *Donax trunculus*; Fig. 3.34), and overall, all harvesting interdictions occurred during spring and autumn. For this group, the only positive relationship between the abundance of PSP-producers and STX concentration in bivalves was observed at L6 area for *Donax trunculus* (N = 57, $p < 0.05$; see Table G.1).

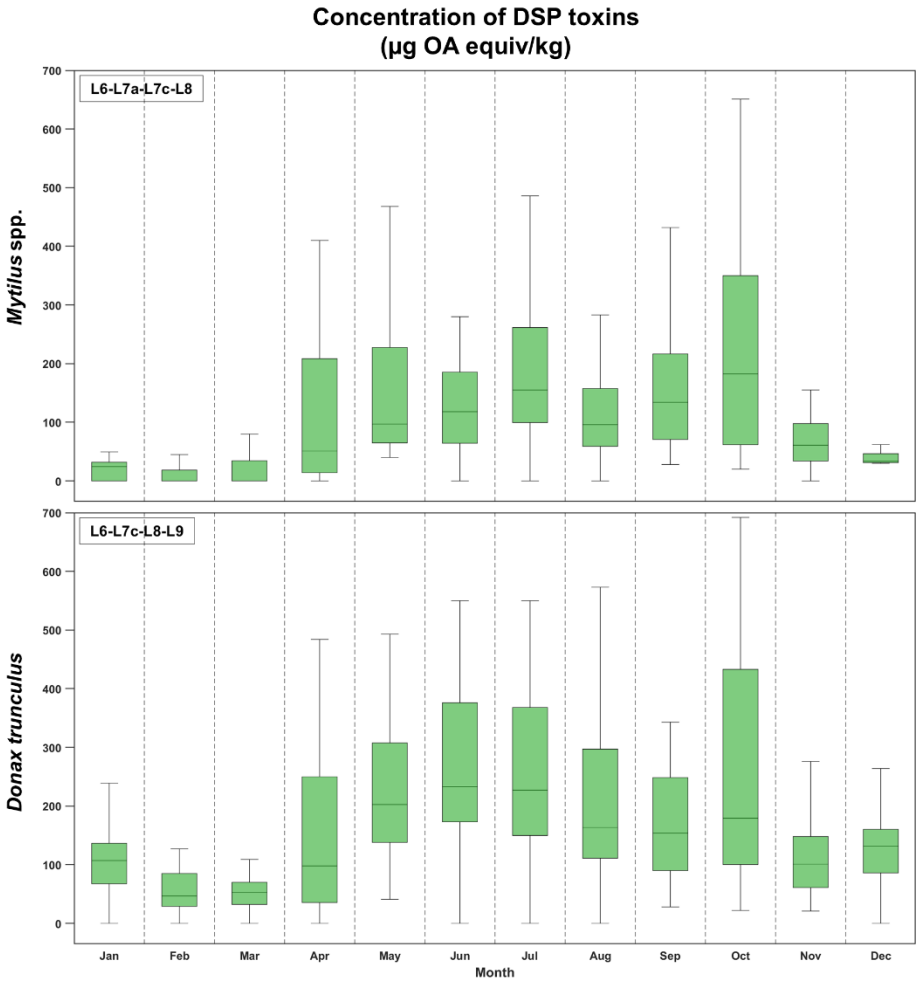

Figure 3.31 - Monthly variability of the concentration of okadaic acid (OA) in two bivalve species (*Mytilus* spp. and *Donax trunculus)*, for all coastal bivalve production areas combined (L6, L7a, L7c, L8, L9), during the period 2014-2019. Median values are identified by the central line within the box, the bottom and top edges of the box indicate the 25th and 75th percentiles, respectively, and the whiskers represent non-outlier limits. See Figure 2.1 for site/area location.

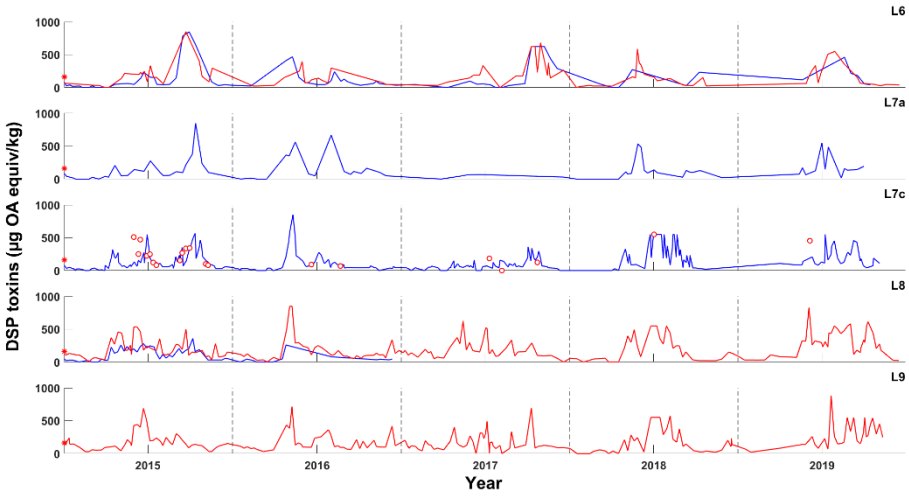

Figure 3.32 – Weekly time series of the concentration of okadaic acid (OA) in two bivalve species, for different coastal bivalve production areas (L6, L7a, L7c, L8, L9), during the period 2014-2019. Blue and red colors represent the toxin content in *Mytilus* spp. and *Donax*

trunculus, respectively. For areas and/or bivalve species with a reduced dataset, circle markers in the corresponding color were used for a more accurate representation. Red asterisks signal the regulatory level for the DSP-toxin group (160 µg OA equivalents kg^{-1}). See Figure 2.1 for site/area location.

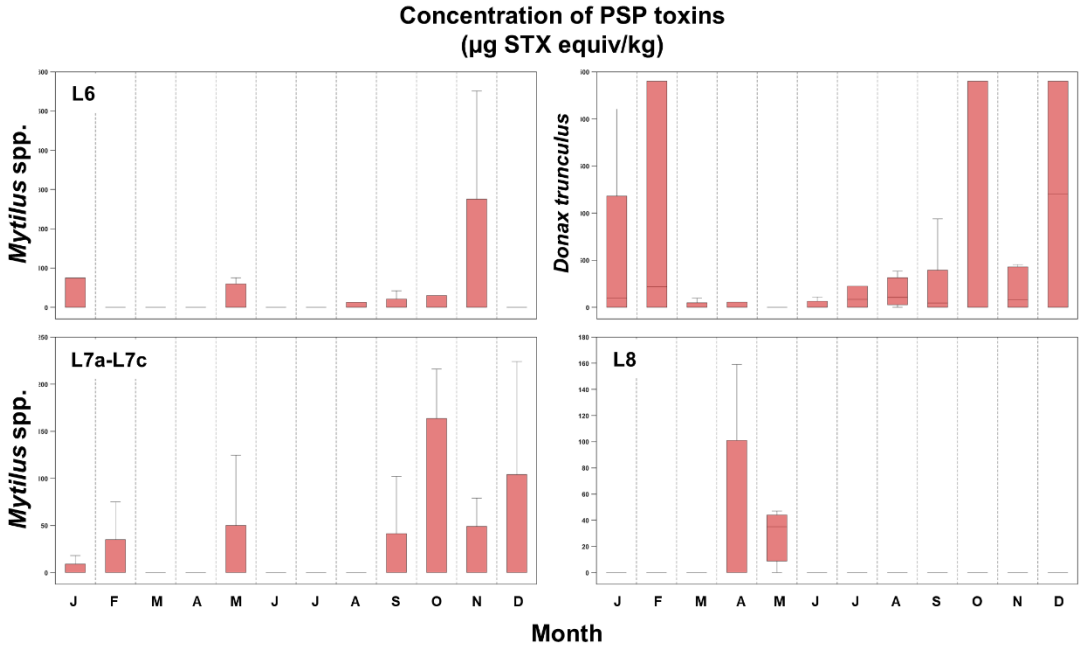

Figure 3.33 - Monthly variability of the concentration of saxitoxin (STX) in two bivalve species (*Mytilus* spp. and *Donax trunculus)*, for L6, L7a-L7c and L8 bivalve production areas, during the period 2014-2019. Median values are identified by the central line within the box, the bottom and top edges of the box indicate the 25th and 75th percentiles, respectively, and the whiskers represent non-outlier limits. See Figure 2.1 for site/area location.

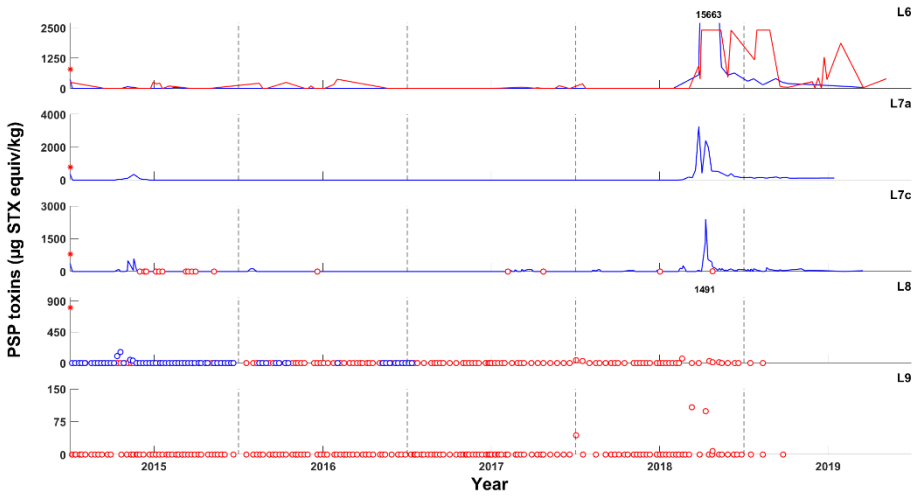

Figure 3.34 – Weekly time series of the concentration of STX (saxitoxin) in two bivalve species, for different coastal bivalve production areas (L6, L7a, L7c, L8, L9), during the period 2014-2019. Blue and red colors represent the toxin content in *Mytilus* spp. and *Donax trunculus*, respectively. Numbers associated with peaks correspond to extreme out-of-scale observations. For areas and/or bivalve species with a reduced dataset, circle markers in the corresponding color were used for a more accurate representation. Red asterisks signal the regulatory level of PSP-toxin group (800 µg STX equivalents kg^{-1}). See Figure 2.1 for site/area location.

4 Discussion

Most phenological studies of phytoplankton are based on satellite-retrieved Chl-a (e.g., Siegel et al., 2002; McClain et al., 2004; Henson and Thomas, 2007; Thomalla et al., 2011; Thomas et al., 2012), thus being representative of the biomass of all taxa within phytoplankton assemblages. Only few studies considered distinct phytoplankton functional types, such as phytoplankton size classes (Cabré et al., 2016; Kostadinov et al., 2017), and studies addressing toxigenic taxa have only focused on *Alexandrium* spp. (Carles et al., 2017; Bucci et al., 2020). In the current study, phytoplankton phenology and variability patterns off southern Portugal were first analysed over specific regions (coastal, transition and oceanic areas) using a 6-year time series of satellite-based Chl-a, and further explored considering *in situ* abundance data from the most frequently reported toxigenic phytoplankton taxa, included into two different functional groups (diatoms and dinoflagellates).

Phytoplankton biomass showed a marked difference between offshore and coastal domains, with higher Chl-a values at WC and Gdn regions and lower values at GoC. Intra-annual variability patterns included unimodal annual cycles with relative increases during late-winter over oceanic regions (WOff, GoC), and an additional summer peak over intermediate (SSlp) and upwelling-influenced regions (WC, SC). At Gdn, a river-influenced region, a single maximum was observed during spring. Interannual non-linear declining trends in Chl-a were detected for oceanic regions, while south coastal domains exhibited a decreasing pattern followed by an increase in later years, agreeing with the non-homogeneous Chl-a profiles over the North Atlantic basin illustrated in the latest CMS Ocean State Report (von Schuckmann et al., 2020). GAM models, used to explore the functional relationships between potential environmental determinants and phytoplankton biomass and key toxigenic data, depicted higher explanatory power (52-77 %) for open ocean (WOff, GoC) and river-influenced regions (60 %; Gdn), and identified SST as the main Chl-a predictor, followed by MLD and PAR, while large-scale climate indices (namely EA and AMO) had a minor influence. Overall, most coastal blooms of toxigenic phytoplankton were linked to DSP (43%) and ASP-producers (41%), and ASP blooms being associated with higher phytoplankton abundances, a probable result of the high potential in situ growth rates (Marañón, 2015) of this r-strategist opportunistic group (Weithoff and Beisner, 2019). Higher abundances of ASP and PSP-producers were attained in coastal upwelling (L6, L7c) and river-influenced regions (L8, L9), respectively, while distribution of DSP-producers appeared more complex (Trainer et al., 2012; Hallegraeff et al., 2012). HAB producers presented distinct intra-annual variability patterns, either with a

bimodal cycle with two maxima (ASP, expect at L7a) during spring and summer, or a unimodal cycle with maximum during late winter (PSP), spring (DSP, PSP, HY), or summer (DSP, HY). According with the best performing GAM models, the most important predictors of ASP and DSP-producers differed across coastal production areas. For instance, the upwelling regime was not a relevant predictor of ASP abundance in GAM models, for most coastal production areas (except L9), but positive DSP anomalies were linked to countercurrent-favourable conditions in all coastal areas (except L7a). Overall, downwelling/countercurrent regime favoured *Dinophysis* spp., and upwelling and/or mixed regimes promoted *Pseudo-nitzschia* spp., during autumn, over L9 production area. Based on this dataset, the working hypothesis was accepted in the case of *Dinophysis* spp., but partly accepted for *Pseudo-nitzschia* spp. ASP models attained lower explanatory power (7%-8%) compared to DSP models (21% - 54%), which probably reflected the occurrence of a high number of species within the genus *Pseudo-nitzschia*, potentially associated with variable ecological niches (see Lelong et al., 2012; Trainer et al., 2012; Bates et al., 2018, and references therein). Therefore, unlike previous modelling studies (see Table 4.1), the resultant models cannot be considered very effective at predicting the abundance of these target groups for the study area. Overall, positive relationships between the abundance of DSP-producers and OA concentration in bivalves, for most coastal areas, reflected the occurrence of a reduced number of toxigenic *Dinophysis* species, easily identifiable, in the study area (*D. acuminata* and *D. acuta*). By contrast, the weak relationship between PSP and ASP producers and associated toxin concentration in bivalves probably reflected the lack of a consistent dataset for PSP, and the presence of a high number of non-toxin producer *Pseudo-nitzschia* species, non-easily identifiable (Lelong et al., 2012; Bates et al., 2018).

4.1 Dynamics of phytoplankton off southern Portugal

Oceanic regions presented low Chl-a values, characteristic of oligotrophic conditions reported for the eastern subtropical North Atlantic (Longhurst, 2007; Teira et al., 2005). Higher Chl-a values over the coastal regions globally reflected enhanced nutrient inputs associated with favourable upwelling conditions, riverine discharges, and anthropogenic influences, as previously observed off south (Cardeira et al., 2013; Navarro et al., 2006) and west Portuguese coasts (Moita et al., 2003; Silva et al., 2009; Picado et al., 2014; Krug et al., 2017; Ferreira et al., 2019). Higher Chl-a at the west coast, in respect to south coastal regions (SC, Gdn), was associated with stronger upwelling intensities (see Fig. 3.5). Moreover, the southeastern transport of west-coast upwelled waters around the Cape São Vicente (see Fig. 2.1), apparently

extended the stimulatory influence of upwelling over the SSlp region (Krug et al., 2017). This enhancement of intermediate regions was also referred for the slope and oceanic regions off the west coast (Cravo et al., 2006; Krug et al., 2017), due to offshore advection of upwelled waters and associated Chl-a rich mesoscale filaments (Fiúza, 1983; Haynes et al., 1993), thereby justifying the similarity in Chl-a between these two regions (SSlp and WOff).

Phytoplankton at the oceanic regions presented a unimodal annual cycle, with bloom starting around October-November (autumn), as previously referred for these regions (Navarro and Ruiz, 2006; Navarro et al., 2012; Reboreda et al., 2014; Krug et al., 2017, 2018). Bloom initiation during the mixed-layer deepening period could be associated with nutrient entrainment through deepening of the surface mixed layer and/or with a relative reduction in phytoplankton grazing mortality, that overcomes the light-driven decreases in cell division rates, causing an increase of phytoplankton net growth rates (disturbance-recovery hypothesis, Behrenfeld et al., 2013; see reviews by Behrenfeld and Boss, 2014, 2018).

Oceanic blooms typically peaked in March, driven by increased light availability during the MLD shoaling phase (critical depth hypothesis; Sverdrup, 1953), and terminated in April, associated with low-nutrient and stratified conditions or overgrazing by heterotrophs (Banse, 1992), a phenological pattern consistent with global (e.g., D'Ortenzio et al., 2012) and basin-wide studies including the study area (Navarro et al., 2012; Krug et al., 2017, 2018; Salgado-Hernanz et al., 2019; Ferreira et al., 2021). As generally referred for temperate oceanic areas (Martinez et al., 2011; D'Ortenzio et al., 2012), and also for the study area (Navarro and Ruiz, 2006; Krug et al., 2017; Ferreira et al., 2019), low Chl-a during the summer period was possibly connected with reduced nutrient availability, due to increased SST and water column stratification. Interestingly, in the WOff region, higher Chl-a under upwelling-favourable conditions during summer (Fig. 3.14), probably reflected the influence of upwelling filaments and jet-like flows, previously observed off the west Portuguese coast (up to 400 km offshore) more frequently during summer months (Haynes et al., 1993; Peliz et al., 2002; Relvas and Barton, 2002). As reported by Krug *et al.* (2017), SST was the main predictor of Chl-a over oceanic areas, showing an overall negative influence that likely reflected the interplay between SST and MLD cycles (with higher temperatures favouring stratification), and the importance of vertical mixing in nutrient supply. MLD and PAR were also important drivers, although the latter did not exhibit a clear association with positive/negative Chl-a anomalies, corroborating previous findings in the same area (Ferreira et al., 2019). The reduced number of relevant

predictors emphasizes the need to consider more potential Chl-a drivers (e.g., sea surface height, meridional and zonal wind components, nutrients) in future modelling studies.

In addition to a primary late-winter/early-spring bloom, probably also influenced by riverine fluxes (Caballero et al., 2014), phytoplankton at the slope region exhibited a secondary Chl-a maximum during summer (see Fig. 3.11). This event was probably related with the southward advection of WC and SC upwelled waters, during a period of more intense upwelling and with less nutrients, that can be retained within the SSlp region, as suggested by Krug *et al.* (2017). This retentive circulation is driven by the cyclonic eddy formed off Cape São Vicente and limited to the west of Cape Santa Maria (Sánchez and Relvas, 2003; García-Lafuente et al., 2006). Indeed, higher Chl-a was observed during upwelling-favourable periods, particularly during spring and summer periods, possibly reflecting the combined effect of water column maxima stratification and upwelling-driven nutrient input on phytoplankton division rates (see review by Behrenfeld and Boss, 2014). However, there was no evidence for the influence of upwelling or river discharge in GAM models, which contrasts with the positive influence of Gdq over SSlp observed by Krug *et al.* (2017). In fact, the combined effects of upwelling, more intense in the western sector of the south Portuguese coast, and river discharge that prevails in the eastern sector, can attenuate the impact of each predictor on overall Chl-a variability in the south coast. As previously reported in the Gulf of Cádiz (Navarro et al., 2012), low SST, typical of the winter MLD deepening phase, coincided with high Chl-a values in SSlp, thereby fitting the argument that a stratified water-column in summer leads to depleted surface Chl-a, and a less stratified water-column in winter leads to enhanced surface Chl-a. Bloom frequency and timing over SSlp showed similarities with oceanic regions, consistent with former studies in this area (Krug et al., 2018; Ferreira et al., 2021). Although, bloom initiation timing was slightly delayed compared with the open ocean, as also reported by previous studies that included the study area (Navarro et al., 2012; Krug et al., 2018; Ferreira et al., 2021).

Table 4.1 - Summary of predictive models established for three specific toxigenic phytoplankton taxa (*Pseudo-nitzschia* spp., *Dinophysis* spp., *Gymnodinium catenatum*), from different studies, with information on study area, model significant predictors, the method utilized, and predictive power or goodness-of-fit measures. The estimated proportion of zeros can also be used as a rough indicator of the goodness-of-fit of the model to the data (Famoye and Singh, 2006; Özmen and Famoye, 2007). HAB: Harmful Algal Bloom, SST: Sea Surface Temperature, NAO: North Atlantic Oscillation, Chl-a: Chlorophyll-a, PAR: Photosynthetically Active Radiation, MLD: Mixed Layer Depth, CSET: Cross-Shore Ekman Transport, GAMM: Generalized Additive Mixed Models, SMA: Standardized Major Axis, NR: Not Referred by the authors.

Study area	Predictors	Method	Predictive power/Goodness-of-fit measures	Reference
		***Pseudo-nitzschia* spp.**		
Santa Barbara Channel (California)	Remote-sensing reflectance (412-555 nm, 510 nm, 555 nm, 510-555 nm), silicic acid:nitrate, particulate absorption (490 nm), Chl-a	Ordinary Least Squares regression	53-75% of bloom observations and 93-96% of non-bloom observations	Anderson *et al.* (2009)
Monterey Bay (California)	Silicic acid, Chl-a, SST, upwelling, river flow, nitrate	Logistic regression (annual & season-specific)	≥ 75% (blooms and non-blooms successfully predicted)	Lane *et al.* (2009)
Chesapeake Bay	Time of the year, location, phosphate, SST, nitrate plus nitrite, freshwater discharge, salinity, silicic acid, dissolved organic carbon, Secchi depth	Logistic Generalized Linear Model	0.25 – 0.53 (Heidke Skill Score range)	Anderson *et al.* (2010)
Lisbon Bay (west coast of Portugal)	Upwelling Index, SST	Zero-Inflated Generalized Poisson Regression Model	12 – 36% (estimated proportion of zeros)	Palma *et al.* (2010)
Santa Barbara Channel (California)	Remote-sensing reflectance (510/555 nm), silicic acid to nitrate*nitrite ratio, silicic acid to phosphate ratio, SST, salinity	Logistic Generalized Linear Model	0.42 – 0.74 (Heidke Skill Score range)	Anderson *et al.* (2011)

Pacific northwest coast	Wind-driven currents, wind-intermittency index, river plume	Numerical model	0.51 – 0.79 (Average Willmott Scores range)	Giddings *et al.* (2014)
Galician rias (northwest Spain)	Ria, day of the year, temperature, salinity, upwelling indices, bloom occurrence in previous weeks	Support Vector Machine Model	0.69 – 0.77 (Kappa value range)	González Vilas *et al.* (2014)
Southwest Ireland	SST, wind index	Zero-Inflated Negative Binomial Model	5934.02 (Akaike Information Criteria)	Cusack *et al.* (2015)
Southwest Ireland	Temperature, salinity, density, volumetric fluxes, current velocities	Hydrodynamic Model	NR	Cusack *et al.* (2016)
Coruña (northwest Iberia)	Upwelling Index, SST, nitrate concentration, cell size, maximum growth rates, optimum temperature for growth, maximum rates of nitrogen uptake	Generalized Additive Mixed Model, Standardized Major-Axis regression	29% (GAMM), 0.1 – 42% (SMA regressions)	Otero *et al.* (2018)
Bahía de La Paz (Mexico)	SST, Chl-a concentration, pH, salinity, dissolved oxygen	Generalized Additive Model	86%	Matus-Hernández *et al.* (2019)
Galician coast (northwest Iberia)	Salinity, Chl-a concentration, $Si(OH)_4$/N ratio	Generalized Additive Mixed Model	NR	Palenzuela *et al.* (2019)
Hawkesbury River estuary (southeast coast of Australia)	Rainfall, water temperature, turbidity, pH, Chl-a concentration, total cells, soluble reactive phosphorus, total nitrogen, Redfield ratio, week of the year	Generalized Additive Model	20 – 55%	Ajani *et al.* (2020)
Southwest Portugal	SST, Chl-a, PAR, MLD, Guadalquivir and Guadiana	Generalized Additive Model	7 – 8%	This study

	Rivers, Alongshore current velocity			
		***Dinophysis* spp.**		
Northwest Portugal	Upwelling intensity, river runoff, SST	Deterministic Lagrangian Model	43%	Moita *et al.* (2006)
Bantry Bay (southwest Ireland)	Wind index, SST	Hydrodynamic and probabilistic models (site-specific)	0.44 (R-squared)	Raine *et al.* (2010)
Northern Bay of Biscay	Surface currents	Deterministic Lagrangian Model	NR	Velo-Suárez *et al.* (2010)
Southeastern Arabian Sea (near Mangalore, India)	SST, salinity, dissolved inorganic nitrogen to phosphorus ratio, total suspended solids, pH, Secchi depth	Logistic Generalized Linear Model	0.04 – 0.46 (Heidke Skill Score range)	Singh *et al.* (2014)
Galician Rías Baixas (northwest Iberia)	NAO index, Cumulative Upwelling Index, SST, tidal range, *D. acuta inoculum*	Generalized Additive Model	13 – 77%	Díaz *et al.* (2016)
Galician Rías and shelf (northwest Iberia)	Surface currents	Deterministic Lagrangian Model	NR	Ruiz-Villarreal *et al.* (2016)
Coruña (northwest Iberia)	Upwelling Index, SST, nitrate concentration, cell size, maximum growth rates, optimum temperature for growth, maximum rates of nitrogen uptake	Generalized Additive Mixed Model, Standardized Major-Axis regression	29% (GAMM), 0.1 – 42% (SMA regressions)	Otero *et al.* (2018)
Southwest Portugal	PAR, MLD, SST, $CSET_{WC}$, Chl-a, Guadalquivir and Guadiana Rivers, Alongshore current velocity	Generalized Additive Model	21 – 54%	This study

Gymnodinium catenatum				
Rías Baixas (northwest Spain)	NAO index (1 month before the bloom event)	Binary Logistic regression (month-specific)	75% correctly classified for clearly favourable months and 72% for clearly unfavourable months	Báez *et al.* (2014)
Bahía de La Paz (Mexico)	SST, Chl-a concentration, pH, salinity, dissolved oxygen	Generalized Additive Model	94%	Matus-Hernández *et al.* (2019)
Southeast Alaska	SST, salinity, freshwater discharge, air temperature	Random Forest Model	37 – 50% (Overall Accuracy range)	Harley *et al.* (2020)
General				
West and south Portuguese coasts	Surface currents	Deterministic Lagrangian Model	NR	Pinto *et al.* (2016)
Portuguese coast (mainland)	Surface currents	Deterministic Lagrangian Model	85% (Forecast Accuracy)	Silva *et al.* (2016)
Northwest European shelf	Bathymetry, near bed temperature and salinity, sea surface temperature and salinity	Maximum Entropy (Maxent) Bioclimate Envelope Model	0.950 – 0.996 (Area under the Curve range)	Townhill *et al.* (2018)
Narmada River (India)	Water transparency, nitrate, temperature, total alkalinity	Generalized Additive Model	66%	Naskar *et al.* (2020)

As reported by Krug *et al.* (2018) for the same area, a higher number of short bloom events were observed in coastal regions compared with ocean and slope regions, suggesting that environmental factors controlling biomass accumulation are more intermittent for coastal regions, namely for WC. Phytoplankton at the WC region showed a primary Chl-a maximum during summer, possibly related with the higher upwelling intensity during this period (Relvas and Barton, 2002; Fig. 3.5). Similarly to Krug *et al.* (2017), this event was more intense than the late-winter bloom. This region presented the highest mean number of bloom events per year, which agrees with the frequent blooms driven by nutrient-rich upwelled waters often reported for coastal upwelling systems (Moita, 2001; Picado et al., 2014; Foukal and Thomas, 2014; Corredor-Acosta et al., 2015). High bloom frequency and short duration support the occurrence of a series of separate, short diatom blooms during upwelling events, interspersed with dinoflagellate blooms during upwelling-relaxation periods (Pitcher et al., 2010; Smayda and Trainer, 2010), reflecting the sequential upwelling-relaxation-upwelling-downwelling events regularly observed off the Iberian coast (Velo-Suárez et al., 2008; Ferreira et al., 2021). During the spring-summer period, higher Chl-a under upwelling or mixed oceanographic regimes compared to downwelling regimes probably reflected the increase in nutrient availability associated with upwelling events. For this region, the influence of upwelling was indirectly detected in GAM models, which showed positive Chl-a anomalies with lower SST values, typical of winter conditions and cold-upwelled waters, and MLD below ca. 20 m, reflecting the MLD shoaling during upwelling events. However, upwelling intensity itself was not identified as a relevant predictor of Chl-a for this region, probably due to the existence of time lags between the upwelling intensity and phytoplankton growth response. For instance, Palma *et al.* (2010), reported a 4-6 days lag for *Pseudo-nitzschia* blooms, which grow preferably under upwelling-favourable conditions, in Lisbon bay. Moreover, AMO showed a positive effect on Chl-a in WC region, contradicting previous studies over longer periods of time (15-18 years) that included the study area (Krug et al., 2017; Ferreira et al., 2019). This discrepancy between temporal ranges may justify the different results. Over the SC region, the late-winter Chl-a maximum might have been promoted by mixed layer deepening and riverine nutrient inputs, since the nutrient-rich Guadiana river plume, formed after periods of intense rainfall during winter, tends to drift westward, into SC region. Other studies also reported that riverine discharges may extend to adjacent coastal areas (Navarro and Ruiz, 2006; Caballero et al., 2014; Krug et al., 2017; Ferreira et al., 2019). Additional nutrient sources that could support this late-winter peak include low-flow streams, lagoons and estuaries in this region, and the indirect effects of local submarine groundwater discharges (Hugman et al., 2015; Krug

et al., 2017). A secondary Chl-a peak was observed during summer, probably generated by local upwelling events, driven by westerly winds (Cristina et al., 2016; Goela et al., 2014, 2016; Navarro and Ruiz, 2006; Krug et al., 2017, 2018). However, this secondary summer bloom was less intense than the WC summer bloom because upwelling intensities are weaker off the south coast (Relvas and Barton, 2002; Fig. 3.5). Chl-a for the SC region was higher under upwelling-favourable conditions during summer, reflecting the relevance of upwelling during periods of increased stratification and reduced availability of nutrients, but higher under countercurrent-favourable or mixed conditions during the winter season. The development of a narrow surface coastal countercurrent, usually during summer but can develop all year-round, that flows westward along the south Portuguese coast (Relvas and Barton, 2002, 2005; Garel et al., 2016), probably allowed the transport of riverine nutrients and/or phytoplankton biomass in the east-west direction, causing an increase in Chl-a over the SC region. In fact, previous studies (Amorim et al., 2004) showed that the development of *Lingulodinium polyedra* blooms in the south coast might have been favoured by the interaction of an upwelling plume and the alongshore flow, i.e., under mixed conditions. The positive influence of Guadalquivir river on Chl-a in the SC region was detected by GAM models, supporting prior findings in the same area that highlighted the importance of large river basins (e.g., Guadiana and Guadalquivir) as a source of nutrients for coastal phytoplankton communities (Huertas et al., 2006; Prieto et al., 2009; Caballero et al., 2014; Krug et al., 2017). However, the influence of Guadiana river was not detected by the models, probably due to the lower mean annual discharge of Gdn (29.6 m^3 s^{-1}) compared with Gdq river (43.5 m^3 s^{-1}).

Chl-a over the river-influenced region (Gdn) exhibited a unimodal annual cycle, with a late-winter maximum, related with water column convective mixing and maximum riverine discharges, as reported by previous studies for the study area (Navarro et al., 2006; Prieto et al., 2009; Caballero et al., 2014; Krug et al., 2017, 2018). This region presented multiple short bloom events throughout the year, typically initiating in mid-winter and terminating in spring, as also referred for river-influenced regions off Iberia (Krug et al., 2018; Ferreira et al., 2021). However, these phenological patterns should be interpreted carefully, due to the potential Chl-a overestimation, aggravated during high river discharge periods, for Case-II optically complex water masses. For these water masses, blue radiation is absorbed not only by phytoplankton but also by non-algal particles (of biological or terrestrial origin) and coloured dissolved organic matter (Caballero et al., 2014; Picado et al., 2014). As for the SC region, higher Chl-a values under countercurrent or mixed regimes during winter at Gdn region, could reflect the

increased transport of riverine nutrients or phytoplankton biomass from eastern locations, associated with freshwater discharges from Guadalquivir and Piedras estuaries (Huertas et al., 2006; Prieto et al., 2009; Krug et al., 2017), westwards by the coastal countercurrent, into the Gdn region.

4.2 Dynamics of potentially toxigenic phytoplankton off southern Portugal

ASP-producing species (*Pseudo-nitzschia* spp.) showed higher mean abundances at L6 and L7c areas, probably due to the higher upwelling intensities affecting these west coastal areas (Relvas and Barton, 2002; Fig. 3.5). Indeed, upwelling regimes usually favour diatom growth over other phytoplankton groups (Smayda and Trainer, 2010; Glibert, 2016), specifically this toxigenic group (Lelong et al., 2012; Trainer et al., 2012; Bates et al., 2018; Kudela et al., 2018). For most production areas (except L7a), ASP-producers exhibited a bimodal annual cycle, with blooms initiating in spring, slightly out of phase in relation to Chl-a (that showed bloom initiation in winter), and peaking during late-spring and summer, probably triggered by increased sunlight during the MLD shoaling phase (Sverdrup, 1953), and nutrient enrichment induced by upwelling conditions. According with Smayda and Trainer (2010), winter-spring and upwelling blooms can be dominated by diatoms, mainly favoured by well-mixed and nutrient-enriched waters. Nonetheless, while winter-spring blooms are usually sustained, upwelling blooms are composed by a series of mini-blooms interrupted by wind-induced, upwelling-relaxation events (Smayda and Trainer, 2010). By contrast, a unimodal annual cycle with a maximum during summer was detected for ASP-producers at the L7a region, probably related with intensified upwelling activity at the west and south coasts that outcompeted the light effects in the beginning of spring. The higher *Pseudo-nitzschia* spp. bloom frequency and duration of all bloom events per year over L6 region ($p < 0.05$), probably reflected more intense and persistent upwelling-favourable conditions along the west coast (Fig. 3.5; Relvas and Barton, 2002; Goela et al., 2016). Indeed, the abundance of *Pseudo-nitzschia* spp. at the southwest Portuguese coast is higher in spring and summer, and this group is frequently responsible for closures of shellfish harvesting during both seasons for this area (Danchenko et al., 2019).

Over the west coast, the abundance of ASP-producers did not differ among physical oceanographic regimes. Over the south coast during autumn, higher abundance was observed during upwelling-favourable (L9) and mixed periods (L8), probably reflecting the occurrence of intermittent westerly wind episodes responsible for local upwelling. Also, during winter, higher abundance of ASP-producers under mixed conditions (L7c) probably reflected the

increase of riverine-inputs of nutrients, from nearby estuaries (Gdn and Gdq rivers), that can be advected westward during upwelling-relaxation periods and cause ASP bloom development in the next upwelling phase. In other coastal upwelling systems such as California, *Pseudo-nitzschia* blooms are commonly associated with weak upwelling, freshwater runoff, and transitional periods (Kudela et al., 2004).

GAM models did not identify upwelling intensity as a relevant ASP predictor for the west Portuguese coast, thereby apparently contradicting most studies of *Pseudo-nitzschia* dynamics in upwelling systems (Pitcher et al., 2010; Mateus et al., 2013; Shumway et al., 2018; Matus-Hernández et al., 2019; Palenzuela et al., 2019). However, positive alongshore current velocities were associated to positive ASP anomalies in L9 area, which indicates that coastal upwelling was an important predictor over this area. *Pseudo-nitzschia* blooms usually develop after 4-6 days of the intensification of the upwelling event off the western Iberian margin, usually under an upwelling intensity lower than 1000 m^3 s^{-1} km^{-1} for the maintenance of relatively high abundances (Palma et al., 2010). Along California coast, *Pseudo-nitzschia* blooms and toxin accumulation can occur 1-2 weeks following the upwelling event (Smith et al., 2018). The occurrence of time lags and periods of intense upwelling-favourable conditions, that typically promote cell dispersion (Moita et al., 2016), might have been responsible for the lack of upwelling signature in GAM models for the west coast. Moreover, positive ASP anomalies associated with SST values below ca. 18 ºC (L6, L7c-L8), may represent an indirect effect of SST, either by upwelling that stimulates diatom communities or by surface cooling which is typically associated with well-mixed water columns responsible for the nutrient entrainment that supports phytoplankton growth (Behrenfeld et al., 2006). However, increases in SST under replete nutritional conditions, from 5 to 48 ºC (Kudela et al., 2018), depending on the species and strains, can also promote *Pseudo-nitzschia* growth rate, as reported for southern California (McCabe et al., 2016; Zhu et al., 2017; Kudela et al., 2020). However, for Bahía de La Paz (northwestern Mexico), GAM models predicted that *Pseudo-nitzschia* would likely be absent for SST higher than 24 ^{O}C (Matus-Hernández et al., 2019). Over L6 area, high *Pseudo-nitzschia* spp. abundances were associated with high Chl-a periods (above ca. 0.6 µg L^{-1}), reflecting the opportunistic nature and high potential growth rates of diatoms, that fully exploit high nutrients, high light and high turbulence conditions, and are usually relevant components of phytoplankton blooms (Glibert, 2016; Weithoff and Beisner, 2019). Previous studies along the west and south Portuguese coasts, also linked high Chl-a concentrations to diatom dominance, specifically to high abundances of *Pseudo-nitzschia* sp. (Brito et al., 2012;

Santos, 2020). MLD < 20 m (L7c-L8 regions) and PAR > 500 µmol photons m^{-2} s^{-1} (L7a) were also associated with positive ASP-producers anomalies, corresponding to upwelling periods.

Over the south coast (L7c-L8, L9), Guadiana and Guadalquivir river discharges showed a negative influence on the abundance of ASP-producers. This result could reflect the temporal mismatch between periods of *Pseudo-nitzschia* dominance over these coastal areas (spring-summer; Danchenko et al., 2019) and high river flow periods, usually associated with intense local rainfall (winter; Cravo et al., 2006; Caballero et al., 2014), not implying any causal relationship. Indeed, the stimulatory effect of river discharges on phytoplankton blooms was already reported along the southern Iberian coast (see Krug et al., 2017 and references therein). Nonetheless, small positive ASP anomalies were detected under low river discharges, probably reflecting the increase in nutrients and mean light intensity in the mixed layer due to haline stratification and shallowing of the MLD induced by river plumes (Barbosa and Chícharo, 2011).

The abundance of DSP-producing species (*Dinophysis* spp.) showed complex temporal variability patterns, and higher mean abundances were detected over L8 area, where upwelling intensity is reduced, favouring highly stratified water columns which constitute the preferable environment for dinoflagellate species (Smayda and Trainer, 2010). On the other hand, lower abundances were detected at L7a ($p < 0.05$), a transition zone that can comprise upwelled waters from either the western or the southern coast, or a combination of both, as reported by Goela *et al.* (2016). The combined effects of intense coastal upwelling and mesoscale filaments related with capes and coast irregularities, may be responsible for the advective transport of a large number of phytoplankton cells out of this coastal production area. In fact, Cravo *et al.* (2010) described an upwelling filament off southwest Iberia that carried a large amount of Chl-a as well as nutrients (considered a proxy of phytoplankton) offshore the coastal upwelling front. DSP-producers, usually dominated by *Dinophysis acuminata* and *D. acuta* off southern Portugal (Moita et al., 2006, 2016; Díaz et al., 2016, 2019), exhibited a unimodal pattern, with blooms occurring in spring or summer, as typically referred for dinoflagellates. This group is usually well adapted to relatively stratified and nutrient-poor environments given its specific set of life traits, including motility, mixotrophy, allelopathy (Smayda and Trainer, 2010; Glibert and Burford, 2017). Off Iberia, the initiation of *Dinophysis acuminata* growth season in spring-summer, that parallels Chl-a increases, has been also related with the beginning of the upwelling season (around March). Yet, earlier DSP blooms caused by this species were observed off northwest Iberia, due to a combination of persistent overwintering populations,

anomalous winter upwelling patterns, and suitable prey densities (*Mesodinium rubrum*; Díaz et al., 2013). In contrast, *D. acuta* thrives later, usually around mid-to-late summer, under thermal stratification and moderate upwelling events (Escalera et al., 2006, 2010; Reguera et al., 2012, Díaz et al., 2019). In comparison with ASP and PSP-producers, DSP-producers were associated with delayed and longer bloom events, that can be explained by the integration of earlier blooms of *D. acuminata* and later *D. acuta* blooms, occurring from late-spring until autumn in northwest Iberia (Escalera et al., 2006). During summer, DSP-forming species were more abundant under mixed oceanographic conditions, at L6 area, which possibly reflected dinoflagellate preference for relatively more stratified and nutrient-poor environments, when compared with upwelling conditions (Smayda and Trainer, 2010; Glibert and Burford, 2017). However, the same results were not expected during winter (at L7c), when nutrient-rich, well-mixed waters favour diatom growth. Mixed conditions are common during relaxation stages between moderate upwelling pulses, and under downwelling/countercurrent conditions, after the end of the upwelling season (Trainer et al., 2010; Reguera et al., 2012; Díaz et al., 2016, 2019; Vidal et al., 2017). GAM models associated low (positive) CSET values (L6) and negative alongshore current velocities (L7c-L8), representative of downwelling/countercurrent conditions favourable for dinoflagellates, to positive anomalies of DSP-producers, and over the south coast, high river discharges were related to negative DSP anomalies, probably reflecting the advective transport of phytoplankton populations associated with strong river flows. However, compared to *Pseudo-nitzschia* spp., *Dinophysis* species are more resistant to high Guadalquivir discharges because of the flagella organelle that allows them to swim under adverse conditions and maintain high cell densities in the thermocline, while diatom colonies of the genus *Pseudo-nitzschia* can only achieve a slow gliding motion (Glibert et al., 2018).

In general, PAR was the most relevant predictor (except for L7a), with higher values promoting increased abundance, which probably represented well-stratified and nutrient-poor conditions that favour dinoflagellates competitively over diatoms (Glibert and Burford, 2017). Higher abundances of DSP-producers on the west coast were associated with MLD < 20 m, SST above ca. 18 ºC or below 16 ºC, low upwelling intensity (above -1000 m^3 s^{-1} km^{-1} coastline), that can represent downwelling periods, and Chl-a values up to 0.6 µg L^{-1}. The combination of SST < 16 ºC and the remaining factors could indicate the occurrence of the species *D. acuminata*, which is highly correlated with stratification but associated with colder waters for the west Portuguese coast (Silva et al., 2009). In contrast, greater SST values were possibly associated with *D. acuta* populations that thrive when there is marked thermal

stratification and moderate upwelling (Reguera et al., 1995; Díaz et al., 2016, 2019). On the western and central sectors of the south coast (L7c-L8), higher abundances of *Dinophysis* spp. were associated with intermediate Chl-a values (between 0.3 and 0.4 μg L^{-1}), probably reflecting a dinoflagellate bloom-window during upwelling relaxation, when the water mass becomes warmer, mixing is less intense, and the nutricline and euphotic layer deepen due to lower biomass (as diatom sink out of the euphotic layer and flagellates reappear because of their motility; Smayda and Trainer, 2010). High Guadalquivir and Guadiana river discharge episodes potentially promoted cell dispersion at L7c-L8 and L9 areas, respectively. Yet, as for ASP-producers, medium to low discharges (Guadalquivir < 300 $m^3 s^{-1}$, Guadiana < 25 $m^3 s^{-1}$) were associated with positive anomalies in the abundance of DSP-producers, probably due to increases in nutrient availability and mean light intensity in the mixed layer, due to haline stratification (Barbosa and Chícharo, 2011). Negative along-shore velocities, corresponding to coastal countercurrents progressing westward (Relvas et al., 2007; Garel et al., 2016), were associated with positive DSP-producer anomalies at L7c-L8. This fact agrees with high densities of *D. acuta* detected in the Rías Baixas (northwest Iberia) at the end of the upwelling season, associated with upwelling relaxation and longshore transport from northern Portugal (Escalera et al., 2010; Díaz et al., 2019).

PSP-producing species, usually dominated by *Gymnodinium catenatum* off Iberia, presented higher mean abundances at L8 and L9 areas, characterized by less frequent and intense upwelling events, compared with the west coast and the westernmost sector of the south coast (Relvas and Barton, 2002; Fig. 3.5). This result agrees with *G. catenatum* preference for periods of upwelling relaxation, between weak upwelling pulses, or downwelling episodes along the Portuguese coast (Amorim et al., 2001; Moita, 2001; Moita et al., 2003) and other systems (Hallegraeff et al., 2012; see Shumway et al., 2018 and references therein). Under a relatively low upwelling-intensity, the fertilizing effect of river discharges combined with stratified conditions, might have been critical for PSP blooms to develop. As DSP-producers, PSP-producers showed also a unimodal annual cycle, but blooms initiated in spring and peaked few weeks later (late-spring), even though previous studies reported maximum abundances in autumn for the west Portuguese coast (Estrada, 1995; Moita et al., 2003; Pitcher et al., 2010). Bravo *et al.* (2010) observed *G. catenatum* blooms on the Galician coast (northwest Iberia), during autumn and winter. Particularly in the Rías Baixas, the predominance of strong southerly winds can sustain the Iberian Poleward Current (that promotes downwelling conditions) until spring, giving rise to later blooms (Crespo and Figueiras, 2007). There are

several possible explanations for the spring PSP maxima observed in this study: delayed deepening of the mixed layer after events of strong northward wind stress in the late upwelling season; reduced shoreward advection of offshore *G. catenatum* populations; alterations in benthic cysts distribution; and changes of dominance in zooplankton communities which have been associated with the Northern Hemisphere warming, causing an increase in grazing pressure during autumn that prevents bloom development, as suggested by Martinez *et al.* (2011) for the northeastern Atlantic.

Blooms of PSP-producers were less frequent and shorter than those of ASP and DSP-producers, although, potential similarities with other dinoflagellates (e.g., DSP group) might be masked by the lack of consistent data for PSP group. These phenological patterns support the occasional short-term PSTs (Paralytic Shellfish Toxins) toxicity episodes described for the southeastern Portuguese coast (Botelho et al., 2019). Also, bloom phenology of PSP-producers (initiation, peak, and termination timings, and total duration) obtained in the current study (dominated by *G. catenatum*) were comparable with bloom phenology reported for other PSP-producers, *Alexandrium* species, from local (Bucci et al., 2020) to broader scales (Carles et al., 2017).

During spring and autumn, PSP-producing species achieved higher abundances under upwelling regimes (L7c), contradicting most studies that reported PSP (dinoflagellate) blooms during upwelling relaxation (summer) or downwelling periods (autumn-winter), over the west Iberian margin (Amorim et al., 2001; Sordo et al., 2001; Moita et al., 2003; Crespo et al., 2006, 2008; Bravo et al., 2010; Pitcher et al., 2010). After the dissipation of upwelling-induced diatom blooms, the vertical swimming capability of large dinoflagellates, opposed to the more passive behavior of diatoms (sinking), allows them to counteract downwelling currents and remain in surface layers for bloom initiation (Fraga et al., 1988; Figueiras et al., 1994; Fermín et al., 1996). During winter, higher abundances of PSP-producers were detected under mixed oceanographic conditions (L8), probably reflecting the combined effects of riverine inputs that contribute to the residual nutrient pool while forming vertical haline stratification, and the transport of seed populations by the coastal countercurrent flowing westward. Hence, the favourable environmental conditions coupled with advective reseeding possibly created a window of opportunity for dinoflagellate blooms (Smayda and Trainer, 2010).

HY-producers (e.g., *Lingulodinium* spp.) peaked during the spring-summer transition, although previous studies in the Galician rias documented higher abundances during upwelling

relaxation periods in summer, and during the transition to downwelling periods in autumn (Míguez et al., 2001; Ospina-Álvarez et al., 2010; Pitcher et al., 2010; Zonneveld et al., 2013). For instance, extensive blooms of *L. polyedra* were reported near the Atlantic margin of Iberia in September (Amorim et al., 2001). As expected (see García-Moreiras et al., 2018 and references therein), HY-producers were only detected under downwelling or mixed conditions, when upper waters still contain nutrients from the prior upwelling event but have become stratified. However, no clear intra-annual pattern was identified for the former group due to the relatively reduced frequency of HY-producers over the study area.

5 Conclusions

The analysis of phytoplankton phenological patterns during a 6-year period revealed a marked difference between oceanic and coastal domains. Phytoplankton at oceanic regions presented a unimodal annual cycle, with few but prolonged bloom events per year, starting during the MLD deepening phase due to nutrient entrainment from deeper layers and/or reduced grazing mortality, peaking in early-spring, with increased light availability, and ending in mid-spring associated with low-nutrient and well-stratified environments. At the slope region, a secondary Chl-a maximum was observed during summer, probably reflecting the combined effects of water column maxima stratification associated with low nutrient availability, and nutrient advection from the south coast during strong upwelling events. Chl-a over west and south coastal areas also exhibited an additional peak during summer, although less intense at SC in respect with WC, due to weaker upwelling intensities off the south coast. Moreover, the development of a coastal countercurrent during upwelling relaxation periods, that flows westward and possibly carries riverine nutrients and phytoplankton biomass, might have also contributed to the increase in Chl-a over the south coast. Coastal regions presented more frequent, short bloom events throughout the year, with the occurrence of diatom mini-blooms (e.g., *Pseudo-nitzschia* spp., ASP-producers) interspersed with dinoflagellate blooms (e.g., *Dinophysis* spp., *G. catenatum*, DSP- and PSP-producers). GAMM analysis highlighted SST as the most important Chl-a predictor, followed by MLD and PAR, while large-scale climate indices (e.g., EA and AMO) showed significant but minor effects. However, the explanatory power of the statistical models decreased towards WC and SC regions, reflecting the increased complexity of phytoplankton forcing processes at coastal domains. At WC region, contrarily to what was expected, upwelling intensity was not identified as a relevant predictor, probably due to the existence of time lags between upwelling-favourable conditions and phytoplankton response. For the southern coast, both coastal regions (SC and Gdn) were positively influenced by Guadalquivir river discharge, although, no significant effect of Guadiana river was detected by the models, probably because of its lower mean annual discharge compared to Guadalquivir river.

As for Chl-a in coastal regions, ASP-producers exhibited a bimodal annual cycle (except at L7a), with the first blooms initiating in spring, later than Chl-a derived blooms, and peaking during late-spring and summer. However, at L7a production area, an unimodal cycle coincident with low phytoplankton abundances, could be explained by the combined effects of intense coastal upwelling from both west and south coasts, and mesoscale filaments associated with

coast protrusions, that can promote the advective transport of phytoplankton cells from this area into the oceanic domain. At the south coast, in the autumn-winter period, higher abundances of ASP-producers under upwelling-favourable and/or mixed conditions were a probable result of upwelling-derived nutrients during occasional westerly wind episodes, and river inputs transported westwards by the coastal countercurrent, that may enhance bloom development in subsequent upwelling phases. Low SST and MLD values, either reflecting upwelling or winter surface cooling associated with well-mixed nutrient-rich water columns, were identified as environmental conditions associated with ASP bloom maintenance and development. By contrast, high river discharges, that typically promote cell dispersion, exerted a negative influence on *Pseudo-nitzschia* spp. abundance. Despite their recognized preference for turbulent environments, upwelling intensity was not a relevant environmental factor to control the abundance of ASP-producers over the west coast. However, in L9 area, positive alongshore current velocities, representative of upwelling-favourable conditions, were associated with positive ASP-producer anomalies. High abundances of *Pseudo-nitzschia* spp. were also associated with high Chl-a concentrations, probably reflecting the high potential *in situ* growth rates of opportunistic diatoms.

DSP-producing species exhibited a unimodal annual cycle, with blooms initiating in spring-summer and peaking until late-summer, which resembles Chl-a variability patterns in coastal regions. The occurrence of two *Dinophysis* species' (*D. acuminata* and *D. acuta*) blooms might justify the extended bloom duration compared to the other toxigenic groups. At WC, during summer, DSP-producers were more abundant under mixed conditions, probably representing a dinoflagellate bloom-window period during relaxation stages between upwelling pulses. However, the same results were not expected during winter months, when diatoms, favoured in well-mixed water columns, outcompete dinoflagellate populations. Light intensity (represented by PAR) was the most relevant predictor for DSP-producers (except at L7a area), which probably reflected well-stratified and nutrient-poor conditions that favour dinoflagellates over diatoms. Low MLD values, intermediate Chl-a, and downwelling/countercurrent conditions were also identified by GAM models as important environmental conditions sustaining high abundances of DSP-producers. As for ASP-producers, high river discharges were associated with negative anomalies of DSP-producers, although, medium to low discharges seemed to positively influence both phytoplankton groups, probably due to increased nutrient and light availability driven by haline stratification. Also, positive correlations between the abundance of DSP-producers and the corresponding toxin

concentration (OA) in bivalves were detected for most coastal areas (except L7c), reflecting the occurrence of a reduced number of toxigenic *Dinophysis* species, easily identifiable (in opposition to ASP-producing species), in the study area.

As DSP-producers, PSP-producers revealed a unimodal annual cycle, with blooms initiating in spring and peaking towards late-spring, which disagrees with the commonly reported autumn PSP maxima. At the south coast, during spring and autumn, high abundances of PSP-producing species under upwelling-favourable conditions contradicted most studies which reported *G. catenatum* blooms during upwelling relaxation or downwelling periods. The lack of a consistent dataset for the former group might justify these discrepancies between our results and previous reports for this group. During winter, PSP-producers were more abundant under mixed conditions, possibly reflecting the combined effects of riverine inputs and advective transport by the coastal countercurrent.

As previously hypothesized, downwelling/countercurrent regime favoured *Dinophysis* spp. abundance, but *Pseudo-nitzschia* spp. was only promoted by upwelling and/or mixed regimes for the most southeastern coastal area.

GAM models applied to the two most abundant phytoplankton toxigenic groups off southern Portugal (ASP and DSP) presented low to moderate explanatory power, highlighting the need for more studies to improve GAM predictive capability. Future research should, therefore, incorporate other environmental predictors, such as nutrients, stratification, turbulence intensity, in situ growth rates, top-down controls (e.g., grazing, sinking, advection), cyst and phytoplankton species-specific abundances, consider different time lags (e.g., upwelling index), and include prey abundance (*Mesodinium rubrum*) for predicting *Dinophysis* blooms. Moreover, future studies should apply GAM analysis to different seasons, compare the performances of empirical GAM models with other models that combine multiple approaches (i.e., hybrid models), and investigate specific extreme events (e.g., heatwaves, cold snaps, droughts, floods).

References

Abdennadher, M., A. B. Kouari, W. F. Sahnoun, E. Alverca, A. Penna, and A. Hamza. 2017. *Ostreopsis cf. ovata* in the Gulf of Gabès (south-eastern Mediterranean Sea): morphological, molecular and ecological characterization. Harmful Algae 63: 56–67. doi:10.1016/j.hal.2017.01.009.

Ajani, P. A., M. E. Larsson, S. Woodcock, A. Rubio, H. Farrell, S. Brett, and S. A. Murray. 2020. Fifteen years of *Pseudo-nitzschia* in an Australian estuary, including the first potentially toxic *P. delicatissima* bloom in the southern hemisphere. Estuar. Coast. Shelf Sci. 236: 106651. doi:10.1016/j.ecss.2020.106651.

Alvarez, I., M. Gomez-Gesteira, M. deCastro, M. Lorenzo, A. Crespo, and J. Dias. 2011. Comparative analysis of upwelling influence between the western and northern coast of the Iberian Peninsula. Cont. Shelf Res. 31: 388–399. doi:10.1016/j.csr.2010.07.009.

Amorim, A., B. Dale, R. Godinho, and V. Brotas. 2001. *Gymnodinium catenatum*-like cysts (Dinophyceae) in recent sediments from the coast of Portugal. Phycologia 40: 572–582. doi:10.2216/i0031-8884-40-6-572.1.

Amorim, A., T. Moita, and P. Oliveira. 2004. Dinoflagellate blooms related to coastal upwelling plumes off Portugal. In: Steidinger, K., Landsberg, J., Thomas, C., Vargo, G. Eds., Harmful Algae 2002. Florida Fish and Wildlife Conservation Commission, Florida Institute of Oceanography, Intergovernmental Oceanographic Commission of UNESCO. 89–91.

Anderson, C. R., D. A. Siegel, R. M. Kudela, and M. A. Brzezinski. 2009. Empirical models of toxigenic *Pseudo-nitzschia* blooms: Potential use as a remote detection tool in the Santa Barbara Channel. Harmful Algae 8: 478–492. doi:10.1016/j.hal.2008.10.005.

Anderson, C. R., M. R. P. Sapiano, M. B. K. Prasad, W. Long, P. J. Tango, C. W. Brown, and R. Murtugudde. 2010. Predicting potentially toxigenic *Pseudo-nitzschia* blooms in the Chesapeake Bay. J. Mar. Syst. 83: 127–140. doi:10.1016/j.jmarsys.2010.04.003.

Anderson, C. R., R. M. Kudela, C. Benitez-Nelson, and others. 2011. Detecting toxic diatom blooms from ocean color and a regional ocean model. Geophys. Res. Lett. 38: L04603. doi:10.1029/2010GL045858.

Babin, M., C. Roesler, and J. J. Cullen. 2008. Real-time Coastal Observing Systems for Marine Ecosystem Dynamics and Harmful Algal Blooms: Theory, Instrumentation and Modelling.

Báez, J. C., R. Real, V. López-Rodas, E. Costas, A. E. Salvo, C. García-Soto, and A. Flores-Moya. 2014. The North Atlantic Oscillation and the Arctic Oscillation favour harmful algal blooms in SW Europe. Harmful Algae 39: 121–126. doi:10.1016/j.hal.2014.07.008.

Banse K. Eds. 1992. Grazing, Temporal Changes of Phytoplankton Concentrations, and the Microbial Loop in the Open Sea. In: Falkowski P.G., Woodhead A.D., Vivirito K. Primary

Productivity and Biogeochemical Cycles in the Sea. Environmental Science Research. 43. Springer, Boston, MA. doi:10.1007/978-1-4899-0762-2_22.

Barbosa, A. B., R. B. Domingues, and H. M. Galvão. 2010. Environmental Forcing of Phytoplankton in a Mediterranean Estuary (Guadiana Estuary, South-western Iberia): A Decadal Study of Anthropogenic and Climatic Influences. Estuaries and Coasts 33: 324–341. doi:10.1007/s12237-009-9200-x.

Barbosa, A. B., and M. A. Chícharo. 2011. Hydrology and Biota Interactions as Driving Forces for Ecosystem Functioning. In: E. Wolanski and D.B.T.-T. on E. and C.S. McLusky. Eds. Treatise on estuarine and coastal science. Academic Press. 7–47.

Bakun, A. 1973. Coastal upwelling indices, west coast of North America, 1946-1971. US Dept. Commerce NOAA Technical Report NMFS-SSRF 671: 1-103.

Barton, A. D., Z. V. Finkel, B. A. Ward, D. G. Johns, and M. J. Follows. 2013. On the roles of cell size and trophic strategy in North Atlantic diatom and dinoflagellate communities. Limnol. Oceanogr. 58(1): 254-266. doi:10.4319/lo.2013.58.1.0254.

Bates, S. S., C. J. Bird, A. S. W. de Freitas, and others. 1989. Pennate Diatom *Nitzschia pungens* as the Primary Source of Domoic Acid, a Toxin in Shellfish from Eastern Prince Edward Island, Canada. Can. J. Fish. Aquat. Sci. 46: 1203–1215.

Bates, S., K. Hubbard, N. Lundholm, M. Montresor, and C. Leaw. 2018. *Pseudo-nitzschia, Nitzschia*, and domoic acid: New research since 2011. Harmful Algae 79: 3–43. doi:10.1016/j.hal.2018.06.001.

Beaugrand, G. 2005. Monitoring pelagic ecosystems using plankton indicators. Ic 62: 333–338. doi:10.1016/j.icesjms.2005.01.002.

Behrenfeld, M. J., R. T. O'Malley, D. A. Siegel, and others. 2006. Climate-driven trends in contemporary ocean productivity. Nature 444: 752–755. doi:10.1038/nature05317.

Behrenfeld, M. J., S. C. Doney, I. Lima, E. S. Boss, and D. A. Siegel. 2013. Annual cycles of ecological disturbance and recovery underlying the subarctic Atlantic spring plankton bloom. Global Biogeochem. Cycles 27: 526–540. doi:10.1002/gbc.20050.

Behrenfeld, M. J., and E. S. Boss. 2014. Resurrecting the Ecological Underpinnings of Ocean Plankton Blooms. Ann. Rev. Mar. Sci. 6: 167–194. doi:10.1146/annurev-marine-052913-021325.

Behrenfeld, M., and E. Boss. 2018. Student's tutorial on bloom hypotheses in the context of phytoplankton annual cycles. Glob. Chang. Biol. 24: 55–77. doi:10.1111/gcb.13858.

Berdalet, E., L. E. Fleming, R. Gowen, and others. 2016. Marine harmful algal blooms, human health and wellbeing: challenges and opportunities in the 21st century. J. Mar. Biol. Assoc. UK 96: 61–91. doi:10.1017/S0025315415001733.

Bograd, S. J., I. Schroeder, N. Sarkar, X. Qiu, W. J. Sydeman, and F. B. Schwing. 2009. Phenology of coastal upwelling in the California Current. Geophys. Res. Lett. 36: 1–5. doi:10.1029/2008GL035933.

Bopp, L., O. Aumont, P. Cadule, S. Alvain, and M. Gehlen. 2005. Response of diatoms distribution to global warming and potential implications: A global model study. Geophys. Res. Lett. 32: 1–4. doi:10.1029/2005GL023653.

Botelho, M. J., C. Vale, and J. G. Ferreira. 2019. Seasonal and multi-annual trends of bivalve toxicity by PSTs in Portuguese marine waters. Sci. Total Environ. 664: 1095–1106. doi: 10.1016/j.scitotenv.2019.01.314.

Bravo, I., S. Fraga, R. Isabel Figueroa, Y. Pazos, A. Massanet, and I. Ramilo. 2010. Bloom dynamics and life cycle strategies of two toxic dinoflagellates in a coastal upwelling system (NW Iberian Peninsula). Deep Sea Res. Part II 57: 222–234. doi:10.1016/j.dsr2.2009.09.004.

Brito, A. C., T. Quental, T. P. Coutinho, M. A. C. Branco, M. Falcão, A. Newton, J. Icely, and T. Moita. 2012. Phytoplankton dynamics in southern Portuguese coastal lagoons during a discontinuous period of 40 years: An overview. Estuar. Coast. Shelf Sci. 110: 147–156. doi:10.1016/j.ecss.2012.04.014.

Bucci, A. F., A. C. Thomas, and I. Cetinić. 2020. Interannual Variability in the Thermal Habitat of *Alexandrium catenella* in the Bay of Fundy and the Implications of Climate Change. Front. Mar. Sci. 7: 587990. doi:10.3389/fmars.2020.587990.

Caballero, I., E. Morris, L. Pietro, and G. Navarro. 2014. The influence of the Guadalquivir River on the spatio-temporal variability of suspended solids and chlorophyll in the Eastern Gulf of Cadiz. Mediterr. Mar. Sci. 15: 721–738. doi:10.12681/mms844.

Caballero, I., R. Fernández, O. M. Escalante, L. Mamán, and G. Navarro. 2020. New capabilities of Sentinel-2A/B satellites combined with in situ data for monitoring small harmful algal blooms in complex coastal waters. Sci. Rep. 10: 1–14. doi:10.1038/s41598-020-65600-1.

Cabré, A., D. Shields, I. Marinov, and T. S. Kostadinov. 2016. Phenology of Size-Partitioned Phytoplankton Carbon-Biomass from Ocean Color Remote Sensing and CMIP5 Models. Front. Mar. Sci. 3: 1–20. doi:10.3389/fmars.2016.00039.

Cardeira, S., F. Rita, P. Relvas, and A. Cravo. 2013. Chlorophyll *a* and chemical signatures during an upwelling event off the South Portuguese coast (SW Iberia). Cont. Shelf Res. 52: 133–149. doi:10.1016/j.csr.2012.11.011.

Carles, G., B. Cedric, and C. Annie. 2017. Global and local factors driving the phenology of *Alexandrium minutum* (Halim) blooms and its toxicity. Harmful Algae 67: 44–60. doi: 10.1016/j.hal.2017.05.005.

Carr, M. 2002. Estimation of potential productivity in Eastern Boundary Currents using remote sensing. Deep. Res. Part II 49: 59–80.

Chavez, F. P., and M. Messié. 2009. A comparison of Eastern Boundary Upwelling Ecosystems. Prog. Oceanogr. 83: 80–96. doi:10.1016/j.pocean.2009.07.032.

Cloern, J. E., and R. Dufford. 2005. Phytoplankton community ecology: principles applied in San Francisco Bay. Mar. Ecol. Prog. Ser. 285: 11–28.

Core Team, R., 2020. R: A Language and Environment for Statistical Computing. R Foundation for Statistical Computing, Vienna, Austria http://www.R-project.org/ accessed 10.10.20.

Corredor-Acosta, A., C. E. Morales, S. Hormazabal, I. Andrade, and M. A. Correa-Ramirez. 2015. Phytoplankton phenology in the coastal upwelling region off central-southern Chile (35ºS–38ºS): Time-space variability, coupling to environmental factors, and sources of uncertainty in the estimates. J. Geophys. Res. Ocean. 120: 813–831. doi:10.1002/2014JC010330.

Costa, P. R., R. Rosa, and M. A. M. Sampayo. 2004. Tissue distribution of the amnesic shellfish toxin, domoic acid, in *Octopus vulgaris* from the Portuguese coast. Mar. Biol. 144: 971–976. doi:10.1007/s00227-003-1258-6.

Costa, P. R., R. Rosa, J. Pereira, and M. A. M. Sampayo. 2005. Detection of domoic acid, the amnesic shellfish toxin, in the digestive gland of *Eledone cirrhosa* and *E. moschata* (Cephalopoda, Octopoda) from the Portuguese coast. Aquat. Living Resour. 18: 395–400. doi:10.1051/alr:2005041.

Cravo, A., M. Madureira, H. Felícia, F. Rita, and M. J. Bebianno. 2006. Impact of outflow from the Guadiana River on the distribution of suspended particulate matter and nutrients in the adjacent coastal zone. Estuar. Coast. Shelf Sci. 70: 63–75. doi:10.1016/j.ecss.2006.05.034.

Cravo, A., P. Relvas, S. Cardeira, F. Rita, M. Madureira, and R. Sánchez. 2010. An upwelling filament off southwest Iberia: Effect on the chlorophyll *a* and nutrient export. Cont. Shelf Res. 30: 1601–1613. doi:10.1016/j.csr.2010.06.007.

Crespo, B. G., F. G. Figueiras, P. Porras, and I. G. Teixeira. 2006. Downwelling and dominance of autochthonous dinoflagellates in the NW Iberian margin: The example of the Ría de Vigo. Harmful Algae 5: 770–781. doi:10.1016/j.hal.2006.03.006.

Crespo, B. G., and F. G. Figueiras. 2007. A spring poleward current and its influence on microplankton assemblages and harmful dinoflagellates on the western Iberian coast. Harmful Algae 6: 686–699. doi:10.1016/j.hal.2007.02.007.

Crespo, B. G., I. G. Teixeira, F. G. Figueiras, and C. G. Castro. 2008. Microplankton composition off NW Iberia at the end of the upwelling season: source areas of harmful dinoflagellate blooms. Mar. Ecol. Prog. Ser. 355: 31-43. doi:10.3354/meps07261.

Cristina, S., C. Cordeiro, S. Lavender, P. Costa Goela, J. Icely, and A. Newton. 2016. MERIS Phytoplankton Time Series Products from the SW Iberian Peninsula (Sagres) Using Seasonal-Trend Decomposition Based on Loess. Remote Sens. 8: 449. doi:10.3390/rs8060449.

Cusack, C., H. Mouriño, M. T. Moita, and J. Silke. 2015. Modelling *Pseudo-nitzschia* events off southwest Ireland. J. Sea Res. 105: 30–41. doi:10.1016/j.seares.2015.06.012.

Cusack, C., T. Dabrowski, K. Lyons, and others. 2016. Harmful algal bloom forecast system for SW Ireland. Part II: Are operational oceanographic models useful in a HAB warning system. Harmful Algae 53: 86–101. doi:10.1016/j.hal.2015.11.013.

Danchenko, S., B. Fragoso, D. Guillebault, J. Icely, M. Berzano, and A. Newton. 2019. Harmful phytoplankton diversity and dynamics in an upwelling region (Sagres, SW Portugal) revealed by ribosomal RNA microarray combined with microscopy. Harmful Algae 82: 52–71. doi:10.1016/j.hal.2018.12.002.

David, V., M. Ryckaert, M. Karpytchev, C. Bacher, V. Arnaudeau, N. Vidal, D. Maurer, and N. Niquil. 2012. Spatial and long-term changes in the functional and structural phytoplankton communities along the French Atlantic coast. Estuar. Coast. Shelf Sci. 108: 37–51. doi:10.1016/j.ecss.2012.02.017.

deCastro, M., M. Gómez-Gesteira, M. N. Lorenzo, I. Alvarez, and A. J. C. Crespo. 2008. Influence of atmospheric modes on coastal upwelling along the western coast of the Iberian Peninsula, 1985 to 2005. Clim. Res. 36: 169–179. doi:10.3354/cr00742.

Díaz, P. A., B. Reguera, M. Ruiz-Villarreal, Y. Pazos, L. Velo-Suárez, H. Berger, and M. Sourisseau. 2013. Climate Variability and Oceanographic Settings Associated with Interannual Variability in the Initiation of *Dinophysis acuminata* Blooms. Mar. Drugs 11: 2964–2981. doi:10.3390/md11082964.

Díaz, P. A., M. Ruiz-villarreal, Y. Pazos, T. Moita, and B. Reguera. 2016. Climate variability and *Dinophysis acuta* blooms in an upwelling system. Harmful Algae 53: 145–159. doi:10.1016/j.hal.2015.11.007.

Díaz, P., B. Reguera, T. Moita, I. Bravo, M. Ruiz-Villarreal, and S. Fraga. 2019. Mesoscale Dynamics and Niche Segregation of Two *Dinophysis* Species in Galician-Portuguese Coastal Waters. Toxins (Basel). 11: 1–21. doi:10.3390/toxins11010037.

Dormann, C. F., J. Elith, S. Bacher, and others. 2013. Collinearity: a review of methods to deal with it and a simulation study evaluating their performance. Ecography (Cop.). 36: 27–46. doi:10.1111/j.1600-0587.2012.07348.x.

D'Ortenzio, F., D. Antoine, E. Martinez, and M. Ribera d'Alcalà. 2012. Phenological changes of oceanic phytoplankton in the 1980s and 2000s as revealed by remotely sensed ocean-color observations. Global Biogeochem. Cycles 26: GB4003. doi:10.1029/2011GB004269.

Dunn, O. J. 1961. Multiple Comparisons among Means. J. Am. Stat. Assoc. 56: 52–64. doi:10.1080/01621459.1961.10482090.

Escalera, L., B. Reguera, Y. Pazos, A. Moroño, and J. M. Cabanas. 2006. Are different species of *Dinophysis* selected by climatological conditions? African J. Mar. Sci. 28: 283–288. doi:10.2989/18142320609504163.

Escalera, L., B. Reguera, T. Moita, Y. Pazos, M. Cerejo, J. M. Cabanas, and M. Ruiz-Villarreal. 2010. Bloom dynamics of *Dinophysis acuta* in an upwelling system: In situ growth versus transport. Harmful Algae 9: 312–322. doi:10.1016/j.hal.2009.12.002.

Estrada, M. 1995. Dinoflagellate assemblages in the Iberian upwelling area. LAVOISIER, PARIS (FRANCE). 157-162.

Famoye, F., and K. Singh. 2006. Zero-inflated generalized Poisson regression model with an application to domestic violence data. J. Data Sci. 4: 117–130.

Fermín, E. G., F. G. Figueiras, B. Arbones, and M. L. Villarino. 1996. SHORT-TIME SCALE DEVELOPMENT OF A *GYMNODINIUM CATENATUM* POPULATION IN THE RIA DE VIGO (NW SPAIN)[1]. J. Phycol. 32: 212–221. doi:10.1111/j.0022-3646.1996.00212.x.

Ferreira, A. S., A. W. Visser, B. R. MacKenzie, and M. R. Payne. 2014. Accuracy and precision in the calculation of phenology metrics. J. Geophys. Res. Ocean. 119: 8438–8453. doi:10.1002/2014JC010323.

Ferreira, A., P. Garrido-Amador, and A. C. Brito. 2019. Disentangling Environmental Drivers of Phytoplankton Biomass off Western Iberia. Front. Mar. Sci. 6: 1–17. doi:10.3389/fmars.2019.00044.

Ferreira, A., V. Brotas, C. Palma, C. Borges, and A. C. Brito. 2021. Assessing Phytoplankton Bloom Phenology in Upwelling-Influenced Regions Using Ocean Color Remote Sensing. Remote Sens. 13: 1–27. doi:10.3390/rs13040675.

Figueiras, F. G., K. J. Jones, A. M. Mosquera, X. A. Alvarez-Salgado, A. Edwards, and N. MacDougall. 1994. Red tide assemblage formation in an estuarine upwelling ecosystem: Ria de Vigo. J. Plankton Res. 16: 857–878. doi:10.1093/plankt/16.7.857.

Fiúza, A. F. de G., M. E. de Macedo, and M. R. Guerreiro. 1982. Climatological space and time variation of the Portuguese coastal upwelling. Oceanol. AC 5: 31–40.

Fiúza, A. F. G. 1983. Upwelling Patterns off Portugal, p. 85–98. In E. Suess and J. Thiede. Eds. Coastal Upwelling Its Sediment Record: Part A: Responses of the Sedimentary Regime to Present Coastal Upwelling. Springer US.

Foukal, N. P., and A. C. Thomas. 2014. Biogeography and phenology of satellite-measured phytoplankton seasonality in the California current. Deep Sea Res. Part I Oceanogr. Res. Pap. 92: 11–25. doi:10.1016/j.dsr.2014.06.008.

Fraga, S., D. M. Anderson, I. Bravo, B. Reguera, K. A. Steidinger, and C. M. Yentsch. 1988. Influence of upwelling relaxation on dinoflagellates and shellfish toxicity in Ria de Vigo, Spain. Estuar. Coast. Shelf Sci. 27: 349–361. doi:10.1016/0272-7714(88)90093-5.

García-Lafuente, J., J. Delgado, F. Criado-Aldeanueva, M. Bruno, J. del Río, and J. M. Vargas. 2006. Water mass circulation on the continental shelf of the Gulf of Cádiz. Deep. Res. Part II 53: 1182–1197. doi:10.1016/j.dsr2.2006.04.011.

García-Lafuente, J., and J. Ruiz. 2007. The Gulf of Cádiz pelagic ecosystem: A review. Prog. Oceanogr. 74: 228–251. doi:10.1016/j.pocean.2007.04.001.

García-Moreiras, I., V. Pospelova, S. García-Gil, and C. Muñoz Sobrino. 2018. Climatic and anthropogenic impacts on the Ría de Vigo (NW Iberia) over the last two centuries: A high-resolution dinoflagellate cyst sedimentary record. Palaeogeogr. Palaeoclimatol. Palaeoecol. 504: 201–218. doi:10.1016/j.palaeo.2018.05.032.

Garel, E., I. Laiz, T. Drago, and P. Relvas. 2016. Characterisation of coastal counter-currents on the inner shelf of the Gulf of Cadiz. J. Mar. Syst. 155: 19–34. doi:10.1016/j.jmarsys.2015.11.001.

Giddings, S. N., P. MacCready, B. M. Hickey, and others. 2014. Hindcasts of potential harmful algal bloom transport pathways on the Pacific Northwest coast. J. Geophys. Res. Ocean. 119: 2439–2461. doi:10.1002/2013JC009622.

Glibert, P. M. 2016. Margalef revisited: A new phytoplankton mandala incorporating twelve dimensions, including nutritional physiology. Harmful Algae 55: 25–30. doi:10.1016/j.hal.2016.01.008.

Glibert, P., and M. Burford. 2017. Globally changing nutrient loads and harmful algal blooms: Recent advances, new paradigms, and continuing challenges. Oceanography 30: 58–69.

Glibert, P. M., E. Berdalet, M. A. Burford, G. C. Pitcher, and M. Zhou. Eds. 2018. Global ecology and oceanography of harmful algal blooms, Springer International Publishing AG.

Goela, P., S. Danchenko, J. D. Icely, L. M. Lubian, S. Cristina, and A. Newton. 2014. Using CHEMTAX to evaluate seasonal and interannual dynamics of the phytoplankton community off the South-west coast of Portugal. Estuar. Coast. Shelf Sci. 151: 112–123. doi:10.1016/j.ecss.2014.10.001.

Goela, P. C., C. Cordeiro, S. Danchenko, J. Icely, S. Cristina, and A. Newton. 2016. Time series analysis of data for sea surface temperature and upwelling components from the southwest coast of Portugal. J. Mar. Syst. 163: 12–22. doi:10.1016/j.jmarsys.2016.06.002.

González-García, C., J. Forja, M. C. González-Cabrera, M. P. Jiménez, and L. M. Lubián. 2018. Annual variations of total and fractionated chlorophyll and phytoplankton groups in the Gulf of Cadiz. Sci. Total Environ. 613–614: 1551–1565. doi:10.1016/j.scitotenv.2017.08.292.

González Vilas, L., E. Spyrakos, J. M. Torres Palenzuela, and Y. Pazos. 2014. Support Vector Machine-based method for predicting *Pseudo-nitzschia* spp. blooms in coastal waters (Galician rias, NW Spain). Prog. Oceanogr. 124: 66–77. doi:10.1016/j.pocean.2014.03.003.

Guerreiro, C., A. Oliveira, H. de Stigter, and others. 2013. Late winter coccolithophore bloom off central Portugal in response to river discharge and upwelling. Cont. Shelf Res. 59: 65–83. doi:10.1016/j.csr.2013.04.016.

Hallegraeff, G. 2004. Harmful algal blooms: A global overview., p. 25–49. In Manual on Harmful Marine Microalgae.

Hallegraeff, G. M., S. I. Blackburn, M. A. Doblin, and C. J. S. Bolch. 2012. Global toxicology, ecophysiology and population relationships of the chainforming PST dinoflagellate *Gymnodinium catenatum*. Harmful Algae 14: 130–143. doi:10.1016/j.hal.2011.10.018.

Harley, J. R., K. Lanphier, E. Kennedy, C. Whitehead, and A. Bidlack. 2020. Random forest classification to determine environmental drivers and forecast paralytic shellfish toxins in Southeast Alaska with high temporal resolution. Harmful Algae 99: 101918. doi:10.1016/j.hal.2020.101918.

Hastie, T. J., and R. J. Tibshirani. 1990. Generalized Additive Models. CRC Press.

Haynes, R., E. D. Barton, and I. Pilling. 1993. Development, Persistence, and Variability of Upwelling Filaments off the Ariantic Coast of the Iberian Peninsula. J. Geophys. Res. 98: 22.681-22.692. doi:10.1029/93JC02016.

Henson, S. A., and A. C. Thomas. 2007. Interannual variability in timing of bloom initiation in the California Current System. J. Geophys. Res. 112: C08007. doi:10.1029/2006JC003960.

Hilbe, J. M. 2011. Negative binomial regression (2nd edition). Cambridge: Cambridge University Press.

Hoagland, P., D. M. Anderson, Y. Kaoru, and A. W. White. 2002. The Economic Effects of Harmful Algal Blooms in the United States: Estimates, Assessment Issues, and Information Needs. Estuaries 25: 819–837. doi:10.1007/BF02804908.

Huertas, I. E., G. Navarro, S. Rodríguez-Gálvez, and L. M. Lubián. 2006. Temporal patterns of carbon dioxide in relation to hydrological conditions and primary production in the northeastern shelf of the Gulf of Cadiz (SW Spain). Deep Sea Res. Part II Top. Stud. Oceanogr. 53: 1344–1362. doi:10.1016/j.dsr2.2006.03.010.

Hugman, R., T. Y. Stigter, J. P. Monteiro, L. Costa, and L. M. Nunes. 2015. Modeling the spatial and temporal distribution of coastal groundwater discharge for different water use scenarios under epistemic uncertainty: case study in South Portugal. Environ. Earth Sci. 73: 2657–2669. doi:10.1007/s12665-014-3709-4.

Irwin, A. J., and Z. V Finkel. 2008. Mining a Sea of Data: Deducing the Environmental Controls of Ocean Chlorophyll. PLoS One 3: 1–6. doi:10.1371/journal.pone.0003836.

James, K. J., B. Carey, J. O'Halloran, F. N. A. M. van Pelt, and Z. Skrabáková. 2010. Shellfish toxicity: human health implications of marine algal toxins. Epidemiol. Infect. 138: 927–940. doi:10.1017/S0950268810000853.

Kemp, A. E. S., and T. A. Villareal. 2018. The case of the diatoms and the muddled mandalas: Time to recognize diatom adaptations to stratified waters. Prog. Oceanogr. 167: 138–149. doi:10.1016/j.pocean.2018.08.002.

Kostadinov, T. S., A. Cabré, H. Vedantham, and others. 2017. Inter-comparison of phytoplankton functional type phenology metrics derived from ocean color algorithms and Earth System Models. Remote Sens. Environ. 190: 162–177. doi:10.1016/j.rse.2016.11.014.

Krug, L., T. Platt, S. Sathyendranath, and A. B. Barbosa. 2017. Ocean surface partitioning strategies using ocean colour remote Sensing: A review. Prog. Oceanogr. 155: 41–53. doi:10.1016/j.pocean.2017.05.013.

Krug, L., T. Platt, S. Sathyendranath, and A. B. Barbosa. 2017. Unravelling region-specific environmental drivers of phytoplankton across a complex marine domain (off SW Iberia). Remote Sens. Environ. 203: 162–184. doi:10.1016/j.rse.2017.05.029.

Krug, L., T. Platt, S. Sathyendranath, and A. B. Barbosa. 2018. Patterns and drivers of phytoplankton phenology off SW Iberia: A phenoregion based perspective. Prog. Oceanogr. 165: 233–256. doi:10.1016/j.pocean.2018.06.010.

Kudela, R., W. Cochlan, and A. Roberts. 2004. Spatial and temporal patterns of *Pseudo-nitzschia* spp. in central California related to regional oceanography. In: Steidinger, K.A., Landsberg, J.H., Tomas, C.R., Vargo, G.A. Eds. Harmful Algae 2002. Florida Fish and Wildlife Conservation Commission. Florida Institute of Oceanography, and Intergovernmental Oceanographic Commission of UNESCO, St. Petersburg, FL, USA. 347–349.

Kudela, R., R. Raine, G. Pitcher, P. Gentien, E. Berdalet, H. Enevoldsen, and E. Urban. 2018. Establishment, Goals, and Legacy of the Global Ecology and Oceanography of Harmful Algal Blooms (GEOHAB) Programme. In: Global ecology and oceanography of harmful algal blooms. Springer, Cham. 27–49.

Kudela, R. M., K. Hayashi, and C. G. Caceres. 2020. Is San Francisco Bay resistant to *Pseudo-nitzschia* and domoic acid? Harmful Algae 92: 101617. doi:10.1016/j.hal.2019.05.010.

Lane, J. Q., P. T. Raimondi, and R. M. Kudela. 2009. Development of a logistic regression model for the prediction of toxigenic *Pseudo-nitzschia* blooms in Monterey Bay, California. Mar. Ecol. Prog. Ser. 383: 37–51.

Lelong, A., H. Hégaret, P. Soudant, and S. S. Bates. 2012. *Pseudo-nitzschia* (Bacillariophyceae) species, domoic acid and amnesic shellfish poisoning: revisiting previous paradigms. Phycologia 51: 168–216. doi:10.2216/11-37.1.

Leterme, S. C., R. D. Pingree, M. D. Skogen, L. Seuront, P. C. Reid, and M. J. Attrill. 2008. Decadal fluctuations in North Atlantic water inflow in the North Sea between 1958 – 2003: impacts on temperature and phytoplankton populations. Oceanologia 50: 59–72.

Li, M., W. Ni, F. Zhang, P. M. Glibert, and C.-H. (Michelle) Lin. 2020. Climate-induced interannual variability and projected change of two harmful algal bloom taxa in Chesapeake Bay, USA. Sci. Total Environ. 744: 140947. doi:10.1016/j.scitotenv.2020.140947.

Litchman, E., P. Pinto, C. Klausmeier, M. Thomas, and K. Yoshiyama. 2010. Linking traits to species diversity and community structure in phytoplankton. Hydrobiologia 653: 15–28. doi:10.1007/s10750-010-0341-5.

Litchman, E., P. de T. Pinto, K. F. Edwards, C. A. Klausmeier, C. T. Kremer, and M. K. Thomas. 2015. Global biogeochemical impacts of phytoplankton: a trait-based perspective. J. Ecol. 103: 1384–1396. doi:10.1111/1365-2745.12438.

Llope, M., K.-S. Chan, P. C. Reid, L. C. Stige, and N. C. Stenseth. 2009. Effects of environmental conditions on the seasonal distribution of phytoplankton biomass in the North Sea. Limnol. Oceanogr. 54: 512–524.

Lorenzo, L. M., B. Arbones, G. H. Tilstone, and F. G. Figueiras. 2005. Across-shelf variability of phytoplankton composition, photosynthetic parameters and primary production in the NW Iberian upwelling system. J. Mar. Syst. 54: 157–173. doi:10.1016/j.jmarsys.2004.07.010.

Longhurst, A. 2007. Ecological geography of the Sea. London: Academic Press.

Marañón, E. 2015. Cell Size as a Key Determinant of Phytoplankton Metabolism and Community Structure. Ann. Rev. Mar. Sci. 7: 241–264. doi:10.1146/annurev-marine-010814-015955.

Margalef, R. 1978. Phytoplankton communities in upwelling areas. The example of NW Africa. Oecologia Aquat. 3: 97–132.

Míguez, B. M., L. Fariña-Busto, F. G. Figueiras, and F. F. Pérez. 2001. Succession of phytoplankton assemblages in relation to estuarine hydrodynamics in the Ría de Vigo: a box-model approach. Sci. Mar. 65: 65–76. doi:10.3989/scimar.2001.65s165.

Martinez, E., D. Antoine, F. D'Ortenzio, and C. de B. Montégut. 2011. Phytoplankton spring and fall blooms in the North Atlantic in the 1980s and 2000s. J. Geophys. Res. 116: C11029. doi:10.1029/2010JC006836.

Mateus, M., A. D. Silva, H. de Pablo, M. T. Moita, T. Quental, and L. Pinto. 2013. Using Lagrangian elements to simulate alongshore transport of harmful algal blooms. Ocean Model. Coast. Manag. Stud. with MOHID 235–248.

Matus-Hernández, M. Á., R. O. Martínez-Rincón, R. J. Aviña-Hernández, and N. Y. Hernández-Saavedra. 2019. Landsat-derived environmental factors to describe habitat preferences and spatiotemporal distribution of phytoplankton. Ecol. Modell. 408: 108759. doi:10.1016/j.ecolmodel.2019.108759.

McCabe, R. M., B. M. Hickey, R. M. Kudela, and others. 2016. An unprecedented coastwide toxic algal bloom linked to anomalous ocean conditions. Geophys. Res. Lett. 43: 10,310-366,376. doi:10.1002/2016GL070023.

McClain, C. R., S. R. Signorini, and J. R. Christian. 2004. Subtropical gyre variability observed by ocean-color satellites. Deep Sea Res. Part II Top. Stud. Oceanogr. 51: 281–301. doi:10.1016/j.dsr2.2003.08.002.

Mendes, C. R., C. Sá, J. Vitorino, C. Borges, V. M. T. Garcia, and V. Brotas. 2011. Spatial distribution of phytoplankton assemblages in the Nazaré submarine canyon region (Portugal): HPLC-CHEMTAX approach. J. Mar. Syst. 87: 90–101. doi:10.1016/j.jmarsys.2011.03.005.

Moita, M. T., 2001. Estrutura, variabilidade e dinâmica do fitoplâncton na costa de Portugal continental. PhD dissertation. University of Lisbon, Lisbon. https://www.ipma.pt/resources.www/docs/publicacoes.site/teses/Teresa_Moita-thesis.pdf (accessed 05/10/2020).

Moita, M. T., P. B. Oliveira, J. C. Mendes, and A. S. Palma. 2003. Distribution of chlorophyll *a* and *Gymnodinium catenatum* associated with coastal upwelling plumes off central Portugal. Acta Oecologica 24: S125–S132. doi:10.1016/S1146-609X(03)00011-0.

Moita, M., L. Sobrinho-Gonçalves, P. Oliveira, S. Palma, and M. Falcão. 2006. A bloom of *Dinophysis acuta* in a thin layer off North-West Portugal. African J. Mar. Sci. 28: 265–269. doi:10.2989/18142320609504160.

Moita, M., Y. Pazos, C. Rocha, R. Nolasco, and P. B. Oliveira. 2016. Toward predicting *Dinophysis* blooms off NW Iberia: A decade of events. Harmful Algae 53: 17–32. doi:10.1016/j.hal.2015.12.002.

Naskar, M., S. Das Sarkar, R. K. Raman, P. Gogoi, S. K. Sahu, G. Chandra, and M. Bhor. 2020. Quantifying plankto-environmental interactions in a tropical river Narmada, India: An alternative model-based approach. Ecohydrol. Hydrobiol. 20: 265–275. doi:10.1016/j.ecohyd.2019.10.006.

Navarro, G., and J. Ruiz. 2006. Spatial and temporal variability of phytoplankton in the Gulf of Cádiz through remote sensing images. Deep. Res. Part II 53: 1241–1260. doi:10.1016/j.dsr2.2006.04.014.

Navarro, G., J. Ruiz, I. E. Huertas, C. M. García, F. Criado-Aldeanueva, and F. Echevarría. 2006. Basin-scale structures governing the position of the deep fluorescence maximum in the Gulf of Cádiz. Deep. Res. Part II 53: 1261–1281. doi:10.1016/j.dsr2.2006.04.013.

Navarro, G., I. Caballero, L. Prieto, A. Vázquez, S. Flecha, I. E. Huertas, and J. Ruiz. 2012. Seasonal-to-interannual variability of chlorophyll-a bloom timing associated with physical forcing in the Gulf of Cádiz. Adv. Sp. Res. 50: 1164–1172. doi:10.1016/j.asr.2011.11.034.

NOAA Harmful Algal BloomS Observing System. 2020. Retrieved from http://service.ncddc.noaa.gov/website/AGSViewers/HABSOS/maps.htm (03/05/2020).

Nykjaer, L., and L. Van Camp. 1994. Seasonal and interannual variability of coastal upwelling along northwest Africa and Portugal from 1981 to 1991. J. Geophys. Res. 99: 14.197-14.207.

Oliveira, M. M., A. S. Camanho, and M. B. Gaspar. 2015. The phycotoxins' impact on the revenue of the Portuguese artisanal dredge fleet. Mar. Policy 52: 45–51. doi:10.1016/j.marpol.2014.10.022.

Ospina-Álvarez, N., R. Prego, I. Alvarez, and others. 2010. Oceanographical patterns during a summer upwelling–downwelling event in the Northern Galician Rias: Comparison with the whole Ria system (NW of Iberian Peninsula). Cont. Shelf Res. 30: 1362–1372. doi:10.1016/j.csr.2010.04.018.

Otero, J., A. Bode, X. Álvarez-salgado, and M. Varela. 2018. Role of functional trait variability in the response of individual phytoplankton species to changing environmental conditions in a coastal upwelling zone. Mar. Ecol. Prog. Ser. 596: 33–47.

Otto, S. A., R. Diekmann, J. Flinkman, G. Kornilovs, and C. Mollmann. 2014. Habitat Heterogeneity Determines Climate Impact on Zooplankton Community Structure and Dynamics. PLoS One 9: 1–11. doi:10.1371/journal.pone.0090875.

Özmen, I., and F. Famoye. 2007. Count regression models with an application to zoological data containing structural zeros. J. Data Sci. 5: 491–502.

Palenzuela, J. M., L. González Vilas, F. M. Bellas, E. Garet, Á. González-Fernández, and E. Spyrakos. 2019. *Pseudo-nitzschia* Blooms in a Coastal Upwelling System: Remote Sensing Detection, Toxicity and Environmental Variables. Water 11. doi:10.3390/w11091954.

Palma, S., H. Mouriño, A. Silva, M. Barão, and T. Moita. 2010. Can *Pseudo-nitzschia* blooms be modeled by coastal upwelling in Lisbon Bay? Harmful Algae 9: 294–303. doi:10.1016/j.hal.2009.11.006.

Peliz, Á., T. L. Rosa, A. M. P. Santos, and J. L. Pissarra. 2002. Fronts, jets, and counter-flows in the Western Iberian upwelling system. J. Mar. Syst. 35: 61–77.

Peliz, Á., A. M. P. Santos, P. B. Oliveira, and J. Dubert. 2004. Extreme cross-shelf transport induced by eddy interactions southwest of Iberia in winter 2001. Geophys. Res. Lett. 31: 1–4. doi:10.1029/2004GL019618.

Pérez, F. F., X. A. Padín, Y. Pazos, M. Gilcoto, M. Cabanas, P. C. Pardo, M. D. Doval, and L. Farina-Bustos. 2010. Plankton response to weakening of the Iberian coastal upwelling. Glob. Chang. Biol. 16: 1258–1267. doi:10.1111/j.1365-2486.2009.02125.x.

Picado, A., I. Alvarez, N. Vaz, R. Varela, M. Gomez-Gesteira, and J. M. Dias. 2014. Assessment of chlorophyll variability along the northwestern coast of Iberian Peninsula. J. Sea Res. 93: 2–11. doi:10.1016/j.seares.2014.01.008.

Pinto, L., M. Mateus, and A. Silva. 2016. Modeling the transport pathways of harmful algal blooms in the Iberian coast. Harmful Algae 53: 8–16. doi:10.1016/j.hal.2015.12.001.

Pitcher, G. C., F. G. Figueiras, B. M. Hickey, and M. T. Moita. 2010. The physical oceanography of upwelling systems and the development of harmful algal blooms. Prog. Oceanogr. 85: 5–32. doi:10.1016/j.pocean.2010.02.002.

Pitcher, G. C., A. B. Jiménez, R. M. Kudela, and B. Reguera. 2017. Harmful algal blooms in eastern boundary upwelling systems: A GEOHAB Core Research Project. Oceanography 30: 22–35. doi:10.5670/oceanog.2017.107.

Prieto, L., G. Navarro, S. Rodríguez-Gálvez, I. E. Huertas, J. M. Naranjo, and J. Ruiz. 2009. Oceanographic and meteorological forcing of the pelagic ecosystem on the Gulf of Cadiz shelf (SW Iberian Peninsula). Cont. Shelf Res. 29: 2122–2137. doi:10.1016/j.csr.2009.08.007.

Prince, E. K., K. L. Poulson, T. L. Myers, R. D. Sieg, and J. Kubanek. 2010. Characterization of allelopathic compounds from the red tide dinoflagellate *Karenia brevis*. Harmful Algae 10: 39–48. doi:10.1016/j.hal.2010.06.003.

Raine, R., G. McDermott, J. Silke, K. Lyons, G. Nolan, and C. Cusack. 2010. A simple short range model for the prediction of harmful algal events in the bays of southwestern Ireland. J. Mar. Syst. 83: 150–157. doi:10.1016/j.jmarsys.2010.05.001.

Ralston, D. K., and S. K. Moore. 2020. Modeling harmful algal blooms in a changing climate. Harmful Algae 91: 101729. doi: 10.1016/j.hal.2019.101729.

Rao, S. T., J.-Y. Ku, and K. S. Rao. 1991. Analysis of Toxic Air Contaminant Data Containing Concentrations Below the Limit of Detection. J. Air & Waste Manag. Assoc. 41: 442–448. doi:10.1080/10473289.1991.10466856.

Reboreda, R., R. Nolasco, C. Castro, X. Álvarez-Salgado, N. Cordeiro, H. Queiroga, and J. Dubert. 2014. Seasonal cycle of plankton production in the Iberian margin based on a high resolution ocean model. J. Mar. Syst. 139: 396–408. doi:10.1016/j.jmarsys.2014.08.004.

Reguera, B., I. Bravo, and S. Fraga. 1995. Autoecology and some life history stages of *Dinophysis acuta* Ehrenberg. J. Plankton Res. 17: 999–1015. doi:10.1093/plankt/17.5.999.

Reguera, B., L. Velo-Suárez, R. Raine, and M. Park. 2012. Harmful *Dinophysis* species: A review. Harmful Algae 14: 87–106. doi:10.1016/j.hal.2011.10.016.

Reguera, B., P. Riobó, F. Rodríguez, P. Díaz, G. Pizarro, B. Paz, J. Franco, and J. Blanco. 2014. *Dinophysis* Toxins: Causative Organisms, Distribution and Fate in Shellfish. Mar. Drugs 12: 394–461. doi:10.3390/md12010394.

Regulation (EC) no. 853/2004 of the European Parliament and of the Council of 29 April 2004 Off. J. Eur. Communities. L139 (2004). 88-102.

Relvas, P., and E. Barton. 2002. Mesoscale patterns in the Cape São Vicente (Iberian Peninsula) upwelling region. J. Geophys. Res. 107: 1–23. doi:10.1029/2000JC000456.

Relvas, P., and E. D. Barton. 2005. A separated jet and coastal counterflow during upwelling relaxation off Cape São Vicente (Iberian Peninsula). Cont. Shelf Res. 25: 29–49. doi:10.1016/j.csr.2004.09.006.

Relvas, P., E. D. Barton, J. Dubert, P. B. Oliveira, Á. Peliz, J. C. B. da Silva, and A. M. P. Santos. 2007. Physical oceanography of the western Iberia ecosystem: Latest views and challenges. Prog. Oceanogr. 74: 149–173. doi:10.1016/j.pocean.2007.04.021.

Reynolds, C.S. 1987. Community organization in the freshwater plankton. Symp. Br. Ecol. Soc. 27: 297-325.

Robinson, I. 2010. Discovering the Ocean from Space. The Unique Applications of Satellite Oceanography. Springer-Praxis Books, Great Britain.

Ruiz-Villarreal, M., L. M. García-García, M. Cobas, P. A. Díaz, and B. Reguera. 2016. Modelling the hydrodynamic conditions associated with *Dinophysis* blooms in Galicia (NW Spain). Harmful Algae 53: 40–52. doi:10.1016/j.hal.2015.12.003.

Salgado-Hernanz, P. M., M.-F. Racault, J. S. Font-Muñoz, and G. Basterretxea. 2019. Trends in phytoplankton phenology in the Mediterranean Sea based on ocean-colour remote sensing. Remote Sens. Environ. 221: 50–64. doi:10.1016/j.rse.2018.10.036.

Sánchez, R. F., and P. Relvas. 2003. Spring–summer climatological circulation in the upper layer in the region of Cape St. Vincent, Southwest Portugal. ICES J. Mar. Sci. 60: 1232–1250. doi:10.1016/S1054-3139(03)00137-1.

Santos, A. M. P., A. S. Kazmin, and Á. Peliz. 2005. Decadal changes in the Canary Upwelling System as revealed by satellite observations: Their impact on productivity. J. Mar. Res. 63: 359–379. doi:10.1357/0022240053693671.

Santos, M., P. B. Oliveira, T. Moita, H. David, M. Caeiro, A. Zingone, A. Amorim, and A. Silva. 2019. Ocurrence of *Ostreopsis* in two temperate coastal Bays (SW Iberia): Insights from the plankton. Harmful Algae 86: 20–36. doi:10.1016/j.hal.2019.03.003.

Santos, M. S. V. D. 2020. Harmful Algal Blooms (HAB) in a changing world: the case of S and W Iberian Bays. Universidade de Lisboa, Faculdade de Ciências.

Santos, M., H. Mouriño, M. T. Moita, A. Silva, A. Amorim, and P. B. Oliveira. 2020. Characterizing phytoplankton biomass seasonal cycles in two NE Atlantic coastal bays. Cont. Shelf Res. 207: 104200. doi:10.1016/j.csr.2020.104200.

Shumway, S. E., J. M. Burkholder, and S. L. Morton. Eds. 2018. Harmful algal blooms: a compendium desk reference, John Wiley & Sons.

Siegel, D. A., S. C. Doney, and J. A. Yoder. 2002. The North Atlantic Spring Phytoplankton Bloom and Sverdrup's Critical Depth Hypothesis. Science. 296: 730–733. doi:10.1126/science.1069174.

Sildever, S., Y. Kawakami, N. Kanno, H. Kasai, A. Shiomoto, S. Katakura, and S. Nagai. 2019. Toxic HAB species from the Sea of Okhotsk detected by a metagenetic approach, seasonality and environmental drivers. Harmful Algae 87: 1–12. doi:10.1016/j.hal.2019.101631.

Silva, A., S. Palma, P. B. Oliveira, and M. T. Moita. 2009. Composition and interannual variability of phytoplankton in a coastal upwelling region (Lisbon Bay, Portugal). J. Sea Res. 62: 238–249. doi:10.1016/j.seares.2009.05.001.

Silva, A., L. Pinto, S. M. Rodrigues, H. de Pablo, M. Santos, T. Moita, and M. Mateus. 2016. A HAB warning system for shellfish harvesting in Portugal. Harmful Algae 53: 33–39. doi:10.1016/j.hal.2015.11.017.

Singh, A., K. Hårding, H. R. V Reddy, and A. Godhe. 2014. An assessment of *Dinophysis* blooms in the coastal Arabian Sea. Harmful Algae 34: 29–35. doi:10.1016/j.hal.2014.02.006.

Smayda, T. 1997. Bloom dynamics: Physiology, behavior, trophic effects. Limnol. Oceanogr. 42: 1132–1136.

Smayda, T., and C. Reynolds. 2001. Community assembly in marine phytoplankton: application of recent models to harmful dinoflagellate blooms. J. Plankton Res. 23: 447–461.

Smayda, T., and V. Trainer. 2010. Dinoflagellate blooms in upwelling systems: Seeding, variability, and contrasts with diatom bloom behaviour. Prog. Oceanogr. 85: 92–107. doi:10.1016/j.pocean.2010.02.006.

Smith, J., P. Connell, R. H. Evans, and others. 2018. A decade and a half of *Pseudo-nitzschia* spp. and domoic acid along the coast of southern California. Harmful Algae 79: 87–104. doi:10.1016/j.hal.2018.07.007.

Sordo, I., E. D. Barton, J. M. Cotos, and Y. Pazos. 2001. An Inshore Poleward Current in the NW of the Iberian Peninsula Detected from Satellite Images, and its Relation with *G. catenatum* and *D. acuminata* Blooms in the Galician Rias. Estuar. Coast. Shelf Sci. 53: 787–799. doi:10.1006/ecss.2000.0788.

Stauffer, B., H. Bowers, E. Buckley, and others. 2019. Considerations in Harmful Algal Bloom Research and Monitoring: Perspectives from a Consensus-Building Workshop and Technology Testing. Front. Mar. Sci. 6: 1–18. doi:10.3389/fmars.2019.00399.

Sverdrup, H. U. 1953. On Conditions for the Vernal Blooming of Phytoplankton. ICES J. Mar. Sci. 18: 287–295. doi:10.1093/icesjms/18.3.287.

Teira, E., B. Mouriño, E. Marañón, and others. 2005. Variability of chlorophyll and primary production in the Eastern North Atlantic Subtropical Gyre: potential factors affecting phytoplankton activity. Deep Sea Res. Part I Oceanogr. Res. Pap. 52: 569–588. doi:10.1016/j.dsr.2004.11.007.

Thackeray, S. J., I. D. Jones, and S. C. Maberly. 2008. Long-term change in the phenology of spring phytoplankton: species-specific responses to nutrient enrichment and climatic change. J. Ecol. 96: 523–535. doi:10.1111/j.1365-2745.2008.01355.x.

Thomalla, S. J., N. Fauchereau, S. Swart, and P. M. S. Monteiro. 2011. Regional scale characteristics of the seasonal cycle of chlorophyll in the Southern Ocean. Biogeosciences 8: 2849–2866. doi:10.5194/bg-8-2849-2011.

Thomas, M. K., C. T. Kremer, C. A. Klausmeier, and E. Litchman. 2012. A Global Pattern of Thermal Adaptation in Marine Phytoplankton. Science. 338: 1085–1088. doi:10.1126/science.1224836.

Townhill, B. L., J. Tinker, M. Jones, and others. 2018. Harmful algal blooms and climate change: exploring future distribution changes. ICES J. Mar. Sci. 75: 1882–1893. doi:10.1093/icesjms/fsy113.

Trainer, V. L., G. C. Pitcher, B. Reguera, and T. J. Smayda. 2010. The distribution and impacts of harmful algal bloom species in eastern boundary upwelling systems. Prog. Oceanogr. 85: 33–52. doi:10.1016/j.pocean.2010.02.003.

Trainer, V. L., S. S. Bates, N. Lundholm, A. E. Thessen, W. P. Cochlan, N. G. Adams, and C. G. Trick. 2012. *Pseudo-nitzschia* physiological ecology, phylogeny, toxicity, monitoring and impacts on ecosystem health. Harmful Algae 14: 271–300. doi: 10.1016/j.hal.2011.10.025.

Trainer, V. L., S. K. Moore, G. Hallegraeff, R. M. Kudela, A. Clement, J. I. Mardones, and W. P. Cochlan. 2020. Pelagic harmful algal blooms and climate change: Lessons from nature's experiments with extremes. Harmful Algae 91: 1–14. doi:10.1016/j.hal.2019.03.009.

Trombetta, T., F. Vidussi, S. Mas, D. Parin, M. Simier, and B. Mostajir. 2019. Water temperature drives phytoplankton blooms in coastal waters. PLoS One 14: e0214933. doi:10.1371/journal.pone.0214933.

Tweddle, J., M. Gubbins, and B. Scott. 2018. Should phytoplankton be a key consideration for marine management? Mar. Policy 97: 1–9. doi:10.1016/j.marpol.2018.08.026.

Vale, P., M. J. Botelho, S. M. Rodrigues, S. S. Gomes, and M. A. de M. Sampayo. 2008. Two decades of marine biotoxin monitoring in bivalves from Portugal (1986–2006): A review of exposure assessment. Harmful Algae 7: 11–25. doi:10.1016/j.hal.2007.05.002.

Velo-Suárez, L., S. González-Gil, P. Gentien, M. Lunven, C. Bechemin, L. Fernand, R. Raine, and B. Reguera. 2008. Thin layers of *Pseudo-nitzschia* spp. and the fate of *Dinophysis acuminata* during an upwelling – downwelling cycle in a Galician Ría. Limnol. Oceanogr. 53: 1816–1834.

Velo-Suárez, L., B. Reguera, S. González-Gil, M. Lunven, P. Lazure, E. Nézan, and P. Gentien. 2010. Application of a 3D Lagrangian model to explain the decline of a *Dinophysis acuminata* bloom in the Bay of Biscay. J. Mar. Syst. 83: 242–252. doi:10.1016/j.jmarsys.2010.05.011.

Vidal, T., A. J. Calado, M. T. Moita, and M. R. Cunha. 2017. Phytoplankton dynamics in relation to seasonal variability and upwelling and relaxation patterns at the mouth of Ria de Aveiro (West Iberian Margin) over a four-year period. PLoS One 1–25. doi:10.1371/journal.pone.0177237.

Villamaña, M., E. Marañón, P. Cermeño, and others. 2019. The role of mixing in controlling resource availability and phytoplankton community composition. Prog. Oceanogr. 178: 1–15.

von Schuckmann, K., P.-Y. Le Traon, N. Smith, and others. 2020. Copernicus Marine Service Ocean State Report, Issue 4. J. Oper. Oceanogr. 13: S1–S172. doi:10.1080/1755876X.2020.1785097.

Weithoff, G., and B. E. Beisner. 2019. Measures and Approaches in Trait-Based Phytoplankton Community Ecology – From Freshwater to Marine Ecosystems. Front. Mar. Sci. 6: 40. doi:10.3389/fmars.2019.00040.

Wood, S. N. 2000. Modelling and smoothing parameter estimation with multiple quadratic penalties. J. R. Stat. Soc. Ser. B 62: 413–428.

Wood, S. N., and N. H. Augustin. 2002. GAMs with integrated model selection using penalized regression splines and applications to environmental modelling. Ecol. Modell. 157: 157–177.

Wood, S. 2006. Generalized additive models: an introduction with R. Boca Raton, Chapman & Hall/CRC, p. 410.

Wooster, W. S., A. Bakun, and D. R. McLain. 1976. The seasonal upwelling cycle along the eastern boundary of the North Atlantic. J. mar. Res. 34: 131-141.

Zarauz, L., X. Irigoien, A. Urtizberea, and M. Gonzalez. 2007. Mapping plankton distribution in the Bay of Biscay during three consecutive spring surveys. Mar. Ecol. Prog. Ser. 345: 27–39. doi:10.3354/meps06970.

Zhang, H.-M., J. Bates, and R. Reynolds. 2006. Assessment of composite global sampling: Sea surface wind speed. Geophys. Res. Lett. 33: 1–5. doi:10.1029/2006GL027086.

Zhu, Z., P. Qu, F. Fu, N. Tennenbaum, A. O. Tatters, and D. A. Hutchins. 2017. Understanding the blob bloom: Warming increases toxicity and abundance of the harmful bloom diatom *Pseudo-nitzschia* in California coastal waters. Harmful Algae 67: 36–43. doi:10.1016/j.hal.2017.06.004.

Zonneveld, K. A. F., F. Marret, G. J. M. Versteegh, and others. 2013. Atlas of modern dinoflagellate cyst distribution based on 2405 data points. Rev. Palaeobot. Palynol. 191: 1–197. doi:10.1016/j.revpalbo.2012.08.003.

Zuur, A. F., E. N. Ieno, N. Walker, A. A. Saveliev, G. M. Smith. 2009. Mixed effects models and extensions in ecology with R. New York: Springer.

Zuur, A. F. 2012. A beginner's guide to generalized additive models with R.

Annexes

Annex A.1 – Alert and interdiction levels defined for the abundance of specific phytoplankton toxin-producing genera/species, aggregated in different biotoxin groups, used in the Portuguese phytoplankton and biotoxin monitoring program. The asterisk symbol signals the value that was recently modified to 50.000 cells L^{-1} (IPMA, 2021).

Biotoxin Group	Main toxin-producing genera/species	Alert Level (cells L^{-1})	Interdiction Level (cells L^{-1})
Paralytic toxins	*Gymnodinium catenatum*	500	> 1.500
	Pyrodinium bahamense		
	Marine cyanobacteria	10.000.000	> 20.000.000
Amnesic toxins	*Pseudo-nitzschia* spp. *seriata* group (cell width > 3 µm)	80.000	200.000
	Pseudo-nitzschia spp. delicatissima group (cell width < 3 µm)	500.000*	1.000.000
Ocadaic acid, dinophysistoxins and pectenotoxins	*Dinophysis* spp.	200	500
	Prorocentrum spp. except *P. minimum*	500	1.000 (*P. minimum*: $1x10^6$)
Yessotoxins	*Gonyaulax spinifera*	1.000	1.000.000
	Lingulodinium polyedra		
	Protoceratium reticulatum		

Annex A.2 – HAB-forming species reported under the scope of the Portuguese HAB Monitoring Program held by the Portuguese Institute for the Sea and Atmosphere (IPMA) and used in this study. ASP: Amnesic Shellfish Poisoning, DSP: Diarrhetic Shellfish Poisoning, PSP: Paralytic Shellfish Poisoning. Source: https://www.ipma.pt/pt/bivalves/fito/index.jsp.

Human toxic syndrome	HAB-forming organisms
ASP	*Pseudo-nitzschia* spp.
	Nitzschia navis-varingica
	Amphora caffeaeformis
DSP	*Dinophysis* spp.
	Prorocentrum spp. (except *P. minimum*)

	Phalacroma sp.
PSP	*Gymnodinium* spp. (including *G. catenatum*)
	Alexandrium spp.
	Pyrodinium bahamense var. compressum
Homoyesso- and Yessotoxin producing dinophyceae	*Lingulodinium* spp. (including *L. polyedra*)
	Gonyaulax spinifera
	Protoceratium reticulatum

Annex A.3 – Maximum authorized levels of different biotoxin groups, responsible for different human poisoning syndromes (Paralytic Shellfish Poisoning - PSP, Amnesic Shellfish Poisoning - ASP, Diarrhetic Shellfish Poisoning - DSP), prescribed in Regulation 853/2004 for live bivalve mollusks, measured in the whole body or any part edible separately.

Biotoxin Group	Human syndrome	Maximum Permissible Quantity
Paralytic toxins	PSP	800 μg of saxitoxin equivalents per kg
Amnesic toxins	ASP	20 mg of domoic acid per kg
Ocadaic acid, dinophysistoxins and pectenotoxins	DSP	160 μg of okadaic acid equivalents per kg
Yessotoxins	DSP	3.75 mg of yessotoxin equivalents per kg

Annex A.4 – List of bivalve mollusk species associated with different coastal production areas in southern Portugal (L6, L7a, L7c, L8, L9). L7c area includes species from L7c1 (Litoral S. Vicente-Lagos) and L7c2 (Litoral Lagos-Albufeira).

Production Area	Code	Species scientific name
Litoral Setúbal-Sines	L6	*Spisula solida*
		Callista chione
		Donax trunculus
		Patella spp.

		Solen marginatus
		Ensis spp.
		Mytilus spp.
		Paracentrotus lividus
Litoral Aljezur-S.Vicente	L7a	*Patella* spp.
		Mytilus spp.
		Paracentrotus lividus
Litoral S.Vicente-Albufeira	L7c	*Patella* spp.
		Mytilus spp.
		Crassostrea gigas
		Spisula solida
		Donax trunculus
		Ostrea edulis
		Chamelea gallina
Litoral Faro-Olhão	L8	*Spisula solida*
		Donax trunculus
		Chamelea gallina
Litoral Tavira-Vila Real de Santo António	L9	*Spisula solida*
		Donax trunculus
		Chamelea gallina

Appendices

Table A.1 – Significant Spearman rank correlation (r_s) coefficients between multiple environmental factors for the six regions off southern Portugal, during the period 2014-2019. Significant r_s values at $p < 0.05$ are given in bold.

WOff

Environmental predictors	log10_Chla	SST	PAR	Im	MLD	AMO	EA	MEI	NAO	WeMO
log10_Chla		**-0.76**	**-0.31**	**-0.51**	**0.50**	**-0.36**	-0.01	0	**0.20**	**0.31**
SST			**0.29**	**0.50**	**-0.53**	**0.45**	**0.20**	**0.15**	**-0.25**	**-0.40**
PAR				**0.91**	**-0.80**	-0.04	**0.12**	0.04	**-0.33**	**-0.35**
Im					**-0.96**	0.06	0.12	0.03	**-0.30**	**-0.42**
MLD						-0.04	-0.11	-0.03	**0.22**	**0.43**
AMO							**0.17**	**-0.16**	**-0.16**	**-0.26**
EA								0.04	0.04	-0.10
MEI									-0.04	-0.03
NAO										**0.19**
WeMO										

GoC

Environmental predictors	log10_Chla	SST	PAR	Im	MLD	AMO	EA	MEI	NAO	WeMO
log10_Chla		**-0.82**	**-0.53**	**-0.71**	**0.70**	**-0.26**	-0.06	-0.09	**0.22**	**0.38**
SST			**0.36**	**0.58**	**-0.61**	**0.45**	**0.22**	**0.13**	**-0.22**	**-0.41**
PAR				**0.89**	**-0.77**	-0.06	0.12	0.03	**-0.32**	**-0.33**
Im					**-0.96**	0.05	**0.14**	0.08	**-0.31**	**-0.42**
MLD						-0.06	**-0.14**	-0.08	**0.27**	**0.42**
AMO							**0.17**	**-0.16**	**-0.16**	**-0.26**
EA								0.04	0.04	-0.10
MEI									-0.04	-0.03
NAO										**0.19**
WeMO										

SSIp

Environmental predictors	log10_Chla	SST	PAR	Im	MLD	CSET_WCSM	CSET_ECSM	Along_vel	AMO	EA	MEI	NAO	WeMO	Gdn	Gdq
log10_Chla		**-0.72**	**-0.29**	**-0.50**	**0.51**	-0.07	-0.09	0.11	**-0.29**	-0.02	0.09	0.06	**0.31**	**0.43**	**0.16**
SST			**0.36**	**0.58**	**-0.61**	0.05	0.09	**-0.24**	**0.48**	**0.23**	0.06	**-0.20**	**-0.45**	**-0.46**	-0.11
PAR				**0.91**	**-0.80**	**-0.26**	**-0.18**	-0.01	-0.07	0.10	0.02	**-0.31**	**-0.33**	**-0.15**	0.00
Im					**-0.96**	**-0.16**	-0.09	-0.11	0.06	**0.16**	0.08	**-0.32**	**-0.42**	**-0.25**	-0.03
MLD						0.12	0.06	**0.15**	-0.07	**-0.17**	-0.09	**0.28**	**0.43**	**0.24**	0.03
CSET_WCSM							**0.95**	**-0.54**	**0.16**	-0.02	0.00	0.12	-0.04	-0.13	**-0.32**
CSET_ECSM								**-0.59**	**0.18**	0.04	-0.01	0.09	-0.09	-0.10	**-0.27**
Along_vel									**-0.18**	**-0.21**	-0.14	-0.10	**0.29**	0.02	0.05
AMO										**0.17**	**-0.16**	**-0.16**	**-0.26**	**-0.25**	**-0.27**
EA											0.04	-0.10	-0.06	-0.06	-0.04
MEI												-0.04	-0.03	0.08	-0.10
NAO													**0.19**	0.07	-0.03
WeMO														0.12	-0.10
Gdn															**0.39**
Gdq															

WC

Environmental predictors	log10_Chla	SST	PAR	Im	MLD	CSET_WC	AMO	EA	MEI	NAO	WeMO
log10_Chla		**-0.18**	**0.45**	**0.20**	**-0.21**	**-0.16**	-0.07	**0.17**	0.08	**-0.22**	-0.08
SST			**0.20**	**0.46**	**-0.52**	0.09	**0.50**	**0.17**	0.10	**-0.13**	**-0.47**
PAR				**0.87**	**-0.67**	**-0.30**	-0.06	0.10	0.02	**-0.32**	**-0.34**
Im					**-0.90**	**-0.13**	0.04	**0.12**	0.07	**-0.28**	**-0.42**
MLD						0.01	-0.10	**-0.13**	-0.07	**0.21**	**0.37**
CSET_WC							0.03	-0.07	0.08	0.05	**-0.12**
AMO								**0.17**	**-0.16**	**-0.16**	**-0.26**
EA									0.04	0.04	-0.10
MEI										-0.04	-0.03
NAO											**0.19**
WeMO											

SC

Environmental predictors	log10_Chla	SST	PAR	Im	MLD	CSET_WCSM	CSET_ECSM	Along_vel	AMO	EA	MEI	NAO	WeMO	Gdn	Gdq
log10_Chla		**-0.68**	**-0.18**	**-0.39**	**0.37**	**-0.16**	**-0.17**	0.12	**-0.29**	-0.07	**0.14**	4.11E-03	**0.28**	**0.44**	**0.20**
SST			**0.38**	**0.60**	**-0.63**	0.07	0.12	**-0.26**	**0.47**	**0.23**	0.05	**-0.20**	**-0.47**	**-0.46**	-0.11
PAR				**0.91**	**-0.80**	**-0.26**	**-0.17**	-0.01	-0.06	0.11	0.02	**-0.31**	**-0.33**	**-0.16**	-2.09E-03
Im					**-0.95**	**-0.16**	-0.07	-0.12	0.09	**0.18**	0.07	**-0.32**	**-0.43**	**-0.26**	-0.05
MLD						0.12	0.05	**0.16**	-0.10	**-0.19**	-0.10	**0.28**	**0.42**	**0.25**	0.06
CSET_WCSM							**0.95**	**-0.54**	**0.16**	-0.02	2.66E-03	0.12	-0.04	-0.13	**-0.32**
CSET_ECSM								**-0.59**	**0.18**	0.04	-0.01	0.09	-0.09	-0.10	**-0.27**
Along_vel									**-0.18**	**-0.21**	-0.14	-0.10	**0.29**	0.02	0.05
AMO										**0.17**	**-0.16**	**-0.16**	**-0.26**	**-0.25**	**-0.27**
EA											0.04	0.04	-0.10	-0.06	-0.04
MEI												-0.04	-0.03	0.08	-0.10
NAO													**0.19**	0.07	-0.03
WeMO														0.12	-0.10
Gdn															**0.39**
Gdq															

Gdn

Environmental predictors	log10_Chla	SST	PAR	Im	MLD	CSET_ECSM	Along_vel	AMO	EA	MEI	NAO	WeMO	Gdn	Gdq
log10_Chla		**-0.75**	**-0.29**	**-0.50**	**0.45**	**-0.17**	**0.16**	**-0.33**	**-0.16**	0.09	0.09	**0.36**	**0.51**	**0.24**
SST			**0.44**	**0.65**	**-0.67**	0.10	**-0.25**	**0.45**	**0.24**	0.04	**-0.22**	**-0.49**	**-0.46**	-0.09
PAR				**0.91**	**-0.78**	**-0.17**	-0.03	-0.05	0.11	0.02	**-0.31**	**-0.34**	**-0.16**	-0.01
Im					**-0.93**	-0.07	-0.14	**0.12**	**0.20**	0.06	**-0.34**	**-0.44**	**-0.31**	-0.07
MLD						0.06	**0.18**	**-0.15**	**-0.21**	-0.11	**0.28**	**0.41**	**0.31**	0.09
CSET_ECSM							**-0.59**	**0.18**	0.04	-0.01	0.09	-0.09	-0.10	**-0.27**
Along_vel								**-0.18**	**-0.21**	-0.14	-0.10	**0.29**	0.02	0.05
AMO									**0.17**	**-0.16**	**-0.16**	**-0.26**	**-0.25**	**-0.27**
EA										0.04	0.04	-0.10	-0.06	-0.04
MEI											-0.04	-0.03	0.08	-0.10
NAO												**0.19**	0.07	-0.03
WeMO													0.12	-0.10
Gdn														**0.39**
Gdq														

Table A.2 – Significant Spearman rank correlation (r_s) coefficients between potential environmental drivers of ASP abundance, for the five coastal bivalve production areas, during the period 2014-2019. Significant r_s values at $p < 0.05$ are given in bold.

L6

Environmental predictors	ASP_abundance	ASP_abundance_tf	log10_Chla	SST	PAR	MLD	CSET_WC
ASP_abundance		**1**	**0.33**	**-0.20**	**0.20**	-0.07	**-0.19**
ASP_abundance_tf			**0.33**	**-0.20**	**0.20**	-0.07	**-0.19**
log10_Chla				**-0.25**	**0.42**	**-0.14**	**-0.29**
SST					**0.17**	**-0.51**	**0.14**
PAR						**-0.64**	**-0.23**
MLD							-0.04
CSET_WC							

L7a

Environmental predictors	ASP_abundance	ASP_abundance_tf	log10_Chla	SST	PAR	MLD	CSET_WC
ASP_abundance		**1**	**0.33**	0.03	**0.45**	**-0.28**	**-0.19**
ASP_abundance_tf			**0.33**	0.03	**0.45**	**-0.28**	**-0.19**
log10_Chla				**-0.22**	**0.43**	**-0.15**	**-0.30**
SST					**0.18**	**-0.51**	**0.16**
PAR						**-0.63**	**-0.20**
MLD							-0.06
CSET_WC							

L7c-L8

Environmental predictors	ASP_abundance	ASP_abundance_tf	log10_Chla	SST	PAR	MLD	CSET_SC	Along_vel	Gdq	Gdn
ASP_abundance		**1**	**0.12**	-0.07	**0.11**	**-0.11**	-0.07	**0.17**	**-0.18**	**-0.12**
ASP_abundance_tf			**0.12**	-0.07	**0.11**	**-0.11**	-0.07	**0.17**	**-0.18**	**-0.12**
log10_Chla				**-0.67**	**-0.20**	**0.38**	**-0.31**	**0.28**	**0.16**	**0.39**
SST					**0.35**	**-0.61**	**0.13**	**-0.34**	-0.05	**-0.45**
PAR						**-0.80**	**-0.24**	-0.07	**0.15**	-0.06
MLD							**0.14**	**0.16**	-0.05	**0.19**
CSET_SC								**-0.51**	**-0.26**	-0.07
Along_vel									-0.02	-0.02
Gdq										**0.36**
Gdn										

L9

Environmental predictors	ASP_abundance	ASP_abundance_tf	log10_Chla	SST	PAR	MLD	CSET_ECSM	Along_vel	Gdq	Gdn
ASP_abundance		**1**	**0.21**	**-0.22**	-0.05	0.05	**-0.16**	**0.30**	-0.04	-0.05
ASP_abundance_tf			**0.21**	**-0.22**	-0.05	0.05	**-0.16**	**0.30**	-0.04	-0.05
log10_Chla				**-0.75**	**-0.28**	**0.45**	**-0.27**	**0.23**	**0.19**	**0.49**
SST					**0.42**	**-0.66**	0.10	**-0.26**	-0.05	**-0.43**
PAR						**-0.77**	**-0.22**	-0.01	0.08	-0.06
MLD							0.11	0.09	0.05	**0.24**
CSET_ECSM								**-0.60**	**-0.27**	-0.05
Along_vel									0.05	-0.08
Gdq										**0.40**
Gdn										

Table A.3 – Significant Spearman rank correlation (r_s) coefficients between potential environmental drivers of DSP abundance, for the five coastal bivalve production areas, during the period 2014-2019. Significant r_s values at $p < 0.05$ are given in bold.

L6

Environmental predictors	DSP_abundance	DSP_abundance_tf	log10_Chla	SST	PAR	MLD	CSET_WC
DSP_abundance		**1**	**0.17**	**0.27**	**0.36**	**-0.43**	3.64E-03
DSP_abundance_tf			**0.17**	**0.27**	**0.36**	**-0.43**	3.64E-03
log10_Chla				**-0.25**	**0.42**	**-0.14**	**-0.29**
SST					**0.17**	**-0.51**	**0.14**
PAR						**-0.64**	**-0.23**
MLD							-0.04
CSET_WC							

L7a

Environmental predictors	DSP_abundance	DSP_abundance_tf	log10_Chla	SST	PAR	MLD	CSET_WC
DSP_abundance		**1**	**0.15**	**0.25**	**0.45**	**-0.45**	-0.02
DSP_abundance_tf			**0.15**	**0.25**	**0.45**	**-0.45**	-0.02
log10_Chla				**-0.22**	**0.43**	**-0.15**	**-0.30**
SST					**0.18**	**-0.51**	**0.16**
PAR						**-0.63**	**-0.20**
MLD							-0.06
CSET_WC							

L7c-L8

Environmental predictors	DSP_abundance	DSP_abundance_tf	log10_Chla	SST	PAR	MLD	CSET_SC	Along_vel	Gdq	Gdn
DSP_abundance		**1**	**-0.15**	**0.28**	**0.30**	**-0.40**	**0.15**	**-0.27**	-0.05	-0.05
DSP_abundance_tf			**-0.15**	**0.28**	**0.30**	**-0.40**	**0.15**	**-0.27**	-0.05	-0.05
log10_Chla				**-0.67**	**-0.20**	**0.38**	**-0.31**	**0.28**	**0.16**	**0.39**
SST					**0.35**	**-0.61**	**0.13**	**-0.34**	-0.05	**-0.45**
PAR						**-0.80**	**-0.24**	-0.07	**0.15**	-0.06
MLD							**0.14**	**0.16**	-0.05	**0.19**
CSET_SC								**-0.51**	**-0.26**	-0.07
Along_vel									-0.02	-0.02
Gdq										**0.36**
Gdn										

L9

Environmental predictors	DSP_abundance	DSP_abundance_tf	log10_Chla	SST	PAR	MLD	CSET_ECSM	Along_vel	Gdq	Gdn
DSP_abundance		**1**	**-0.23**	**0.37**	**0.29**	**-0.32**	0.05	-0.13	-0.02	**-0.13**
DSP_abundance_tf			**-0.23**	**0.37**	**0.29**	**-0.32**	0.05	-0.13	-0.02	**-0.13**
log10_Chla				**-0.75**	**-0.28**	**0.45**	**-0.27**	**0.23**	**0.19**	**0.49**
SST					**0.42**	**-0.66**	0.10	**-0.26**	-0.05	**-0.43**
PAR						**-0.77**	**-0.22**	-0.01	0.08	-0.06
MLD							0.11	0.09	0.05	**0.24**
CSET_ECSM								**-0.60**	**-0.27**	-0.05
Along_vel									0.05	-0.08
Gdq										**0.40**
Gdn										

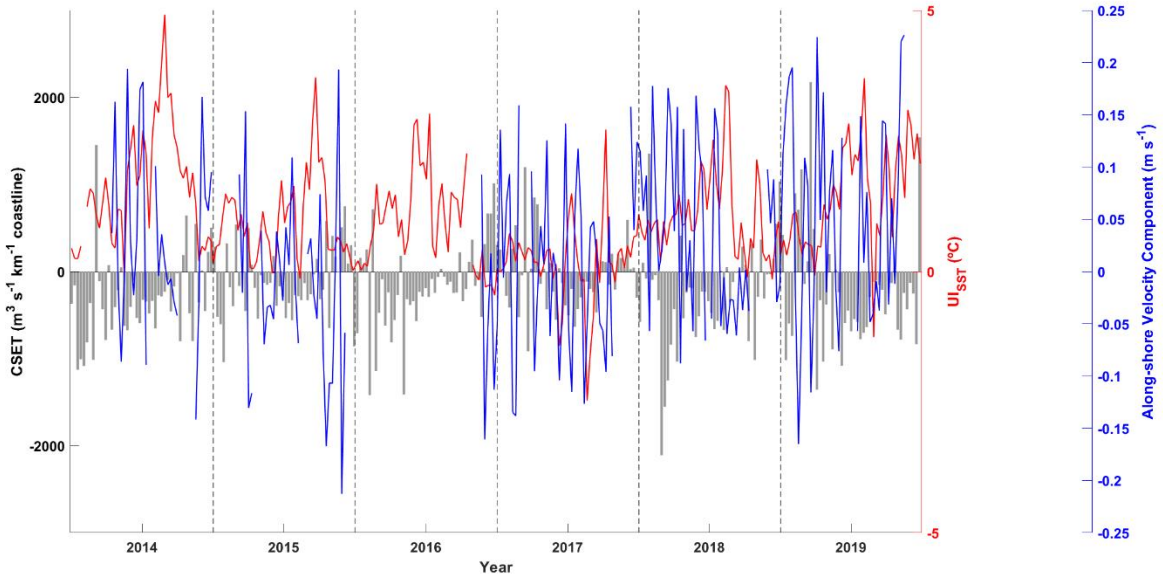

Appendix B.1 – Temporal variability (2014-2019) of cross-shore Ekman transport (CSET) represented by the grey bars, upwelling index based on SST difference (UI_{SST}) indicated in red

color, and the alongshore velocity component measured at the Armona site (see Figure 2.1 for location) represented in blue color. Both upwelling indices were estimated for the west side of CSM.

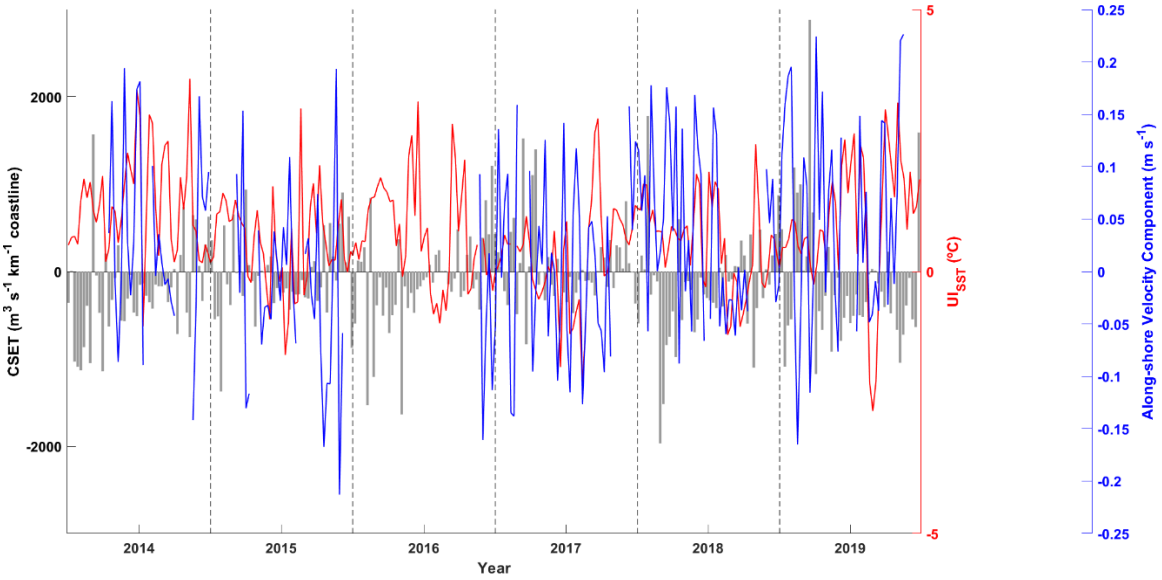

Appendix B.2 – Temporal variability (2014-2019) of cross-shore Ekman transport (CSET) represented by the grey bars, upwelling index based on SST difference (UI_{SST}) indicated in red color, and the alongshore velocity component measured at the Armona site (see Figure 2.1 for location) represented in blue color. Both upwelling indices were estimated for the east side of CSM.

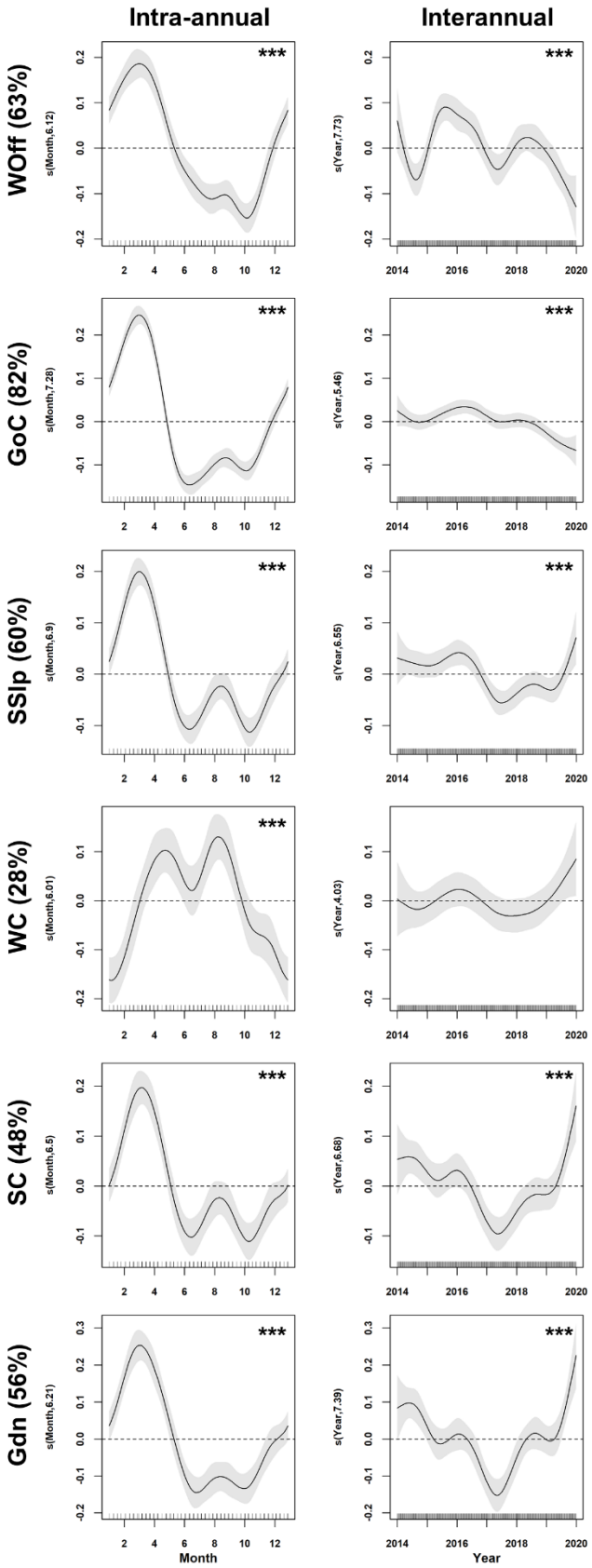
Intra-annual
Interannual
WOff (63%)
GoC (82%)
SSlp (60%)
WC (28%)
SC (48%)
Gdn (56%)
s(Month,6.12)
s(Year,7.73)
s(Month,7.26)
s(Year,5.46)
s(Month,6.9)
s(Year,6.55)
s(Month,6.01)
s(Year,4.03)
s(Month,6.5)
s(Year,6.68)
s(Month,6.21)
s(Year,7.39)
***
Month
Year

Appendix C.1 – Generalized additive mixed models (GAMM) of Chl-a temporal variability, using month and year as covariates. For each region, the model explanatory power (as % of Chl-a variance explained) is presented in brackets after region abbreviation, and the significance level (p-value) of each predictor is denoted by asterisk symbols (top right), where *, **, *** indicate p-value <0.05, <0.01 and <0.001, respectively. In the left column are the plots representing intra-annual variability, and in the right column, the plots of interannual variability for each region. The solid line is the fitted model and grey shaded areas represent the 95% confidence intervals. The short vertical lines on the x-axis represent the actual predictor observations, and the values on the y-axis denote the effective degrees of freedom (edf). Edf values of 1 represent a linear effect of the predictor on Chl-a anomaly, and values higher than 1 indicate non-linear effects. Positive (negative) y-values indicate that the predictor exerts a positive (negative) influence on Chl-a concentration.

Table C.1 – Summary results of the best-performing generalized additive mixed models (GAMM) used to decompose region-specific Chl-a time series into seasonal and interannual components. Information includes model adjusted coefficient of determination (Adj. R^2), Akaike's Information Criteria (AIC), parametric coefficients (intercept ± standard error) and test statistic (t/F value), estimated degrees of fredoom (edf) and significance level (p-value) for the model covariates. Smoothing functions are represented by s(i), for each covariate. Edf values of 1 imply a linear effect and values higher than 1 indicate non-linear effects. Asterisk symbols are associated with different p-value cutoff scores: <0.05 (*); <0.01 (**); <0.001 (***).

Model WOff	n	Coefficients (Std. Error)		t(F)-value	p-value	edf	Adj. R-sq.	AIC
log(Chla) ~ s(Month) + s(Year)	276	Intercept	-0.6753 (0.006)	-109.5	<2e-16 ***	-	0.628	-418.7
		s(Month)	-	39.662	<2e-16 ***	6.115		
		s(Year)	-	9.521	<2e-16 ***	7.732		

Model GoC	n	Coefficients (Std. Error)		t(F)-value	p-value	edf	Adj. R-sq.	AIC
log(Chla) ~ s(Month) + s(Year)	275	Intercept	-0.8043 (0.004)	-208.4	<2e-16 ***	-	0.816	-678.4
		s(Month)	-	135.165	<2e-16 ***	7.278		
		s(Year)	-	8.888	<2e-16 ***	5.460		

Model SSlp	n	Coefficients (Std. Error)		t(F)-value	p-value	edf	Adj. R-sq.	AIC
log(Chla) ~ s(Month) + s(Year)	276	Intercept	-0.6318 (0.005)	-125.9	<2e-16 ***	-	0.603	-534.6
		s(Month)	-	45.127	<2e-16 ***	6.898		
		s(Year)	-	5.985	2.25e-16 ***	6.546		

Model WC	n	Coefficients (Std. Error)		t(F)-value	p-value	edf	Adj. R-sq.	AIC
log(Chla) ~ s(Month) + s(Year)	275	Intercept	-0.2443 (0.01)	-25.35	<2e-16 ***	-	0.276	-190.8
		s(Month)	-	12.26	<2e-16 ***	6.009		
		s(Year)	-	1.93	0.114	4.030		

Model SC	n	Coefficients (Std. Error)		t(F)-value	p-value	edf	Adj. R-sq.	AIC
log(Chla) ~ s(Month) + s(Year)	276	Intercept	-0.4858 (0.007)	-71.90	<2e-16 ***	-	0.482	-372.7
		s(Month)	-	23.929	<2e-16 ***	6.501		
		s(Year)	-	9.133	<2e-16 ***	6.677		

Model Gdn	n	Coefficients	(Std. Error)	t(F)-value	p-value	edf	Adj. R-sq.	AIC
log(Chla) ~ s(Month) + s(Year)	275	Intercept	-0.3664 (0.008)	-45.45	<2e-16 ***	-	0.559	-272.8
		s(Month)	-	31.07	<2e-16 ***	6.211		
		s(Year)	-	13.15	<2e-16 ***	7.393		

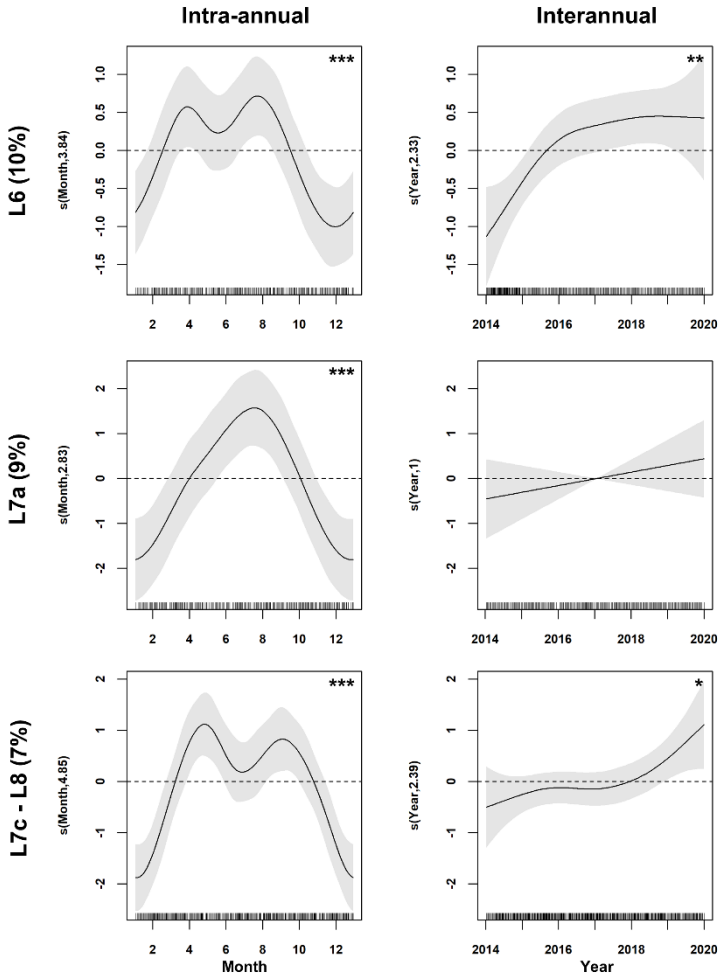

Appendix C.2 – Generalized additive models (GAM) of ASP abundance temporal variability, using month and year as covariates. For each region, the model explanatory power (as % of ASP variance explained) is presented in brackets after region abbreviation, and the significance level (p-value) of each predictor is denoted by asterisk symbols (top right), where *, **, *** indicate p-value <0.05, <0.01 and <0.001, respectively. In the left column are the plots representing intra-annual variability, and in the right column, the plots of interannual variability for each region. The solid line is the fitted model and grey shaded areas represent the 95% confidence intervals. The short vertical lines on the x-axis represent the actual predictor

observations, and the values on the y-axis denote the effective degrees of freedom (edf). Edf values of 1 represent a linear effect of the predictor on ASP abundance, and values higher than 1 indicate non-linear effects. Positive (negative) y-values indicate that the predictor exerts a positive (negative) influence on ASP abundance.

Table C.2 – Summary results of the best-performing generalized additive models (GAM) or mixed models (GAMM) used to decompose region-specific ASP abundance time series into seasonal and interannual components. Information includes model adjusted coefficient of determination (Adj. R^2), equivalente to explained deviance, smoothing parameter estimation using the restricted maximum likelihood (REML) method, Akaike's Information Criteria (AIC), parametric coefficients (intercept ± standard error) and test statistic (t/F/z/Chi-square value), estimated degrees of fredoom (edf) and significance level (p-value) for the model covariates. Smoothing functions are represented by s(i), for each covariate. Edf values of 1 imply a linear effect and values higher than 1 indicate non-linear effects. k values indicate the estimated dispersion parameter. Asterisk symbols are associated with different p-value cutoff scores: <0.05 (*); <0.01 (**); <0.001 (***).

Model L6	n	Coefficients (Std. Error)		t(F)-value	p-value	edf	k	Adj. R-sq.	AIC
ASP_abundance_rd ~ s(Month) + s(Year)	347	Intercept	8.8933 (0.133)	66.83	<2e-16 ***	-	0.113	0.0981	1469.4
		s(Month)	-	2.818	5.24e-05 ***	3.844			
		s(Year)	-	6.827	0.001 **	2.332			

Model L7a	n	Coefficients (Std. Error)		z(Chi.sq)-value	p-value	edf	k	Deviance expl. (%)	-REML	AIC
ASP_abundance_rd ~ s(Month) + s(Year)	290	Intercept	8.7881 (0.252)	34.92	<2e-16 ***	-	0.054	9.04	1629.7	3264.4
		s(Month)	-	22.865	8.49e-06 ***	2.827				
		s(Year)	-	1.052	0.306	1.001				

Model L7c-L8	n	Coefficients (Std. Error)		z(Chi.sq)-value	p-value	edf	k	Deviance expl. (%)	-REML	AIC
ASP_abundance_rd ~ s(Month) + s(Year)	655	Intercept	9.3828 (0.135)	69.64	<2e-16 ***	-	0.084	6.83	4633.7	9265.9
		s(Month)	-	48.314	<2e-16 ***	4.851				
		s(Year)	-	7.929	0.042 *	2.394				

Model L9	n	Coefficients (Std. Error)		z(Chi.sq)-value	p-value	edf	k	Deviance expl. (%)	-REML	AIC
ASP_abundance_rd ~ s(Month) + s(Year)	299	Intercept	9.4525 (0.259)	36.55	<2e-16 ***	-	0.05	0.426	1676.7	3360.1
		s(Month)	-	0.001	0.633	0.001				
		s(Year)	-	0.908	0.341	1.001				

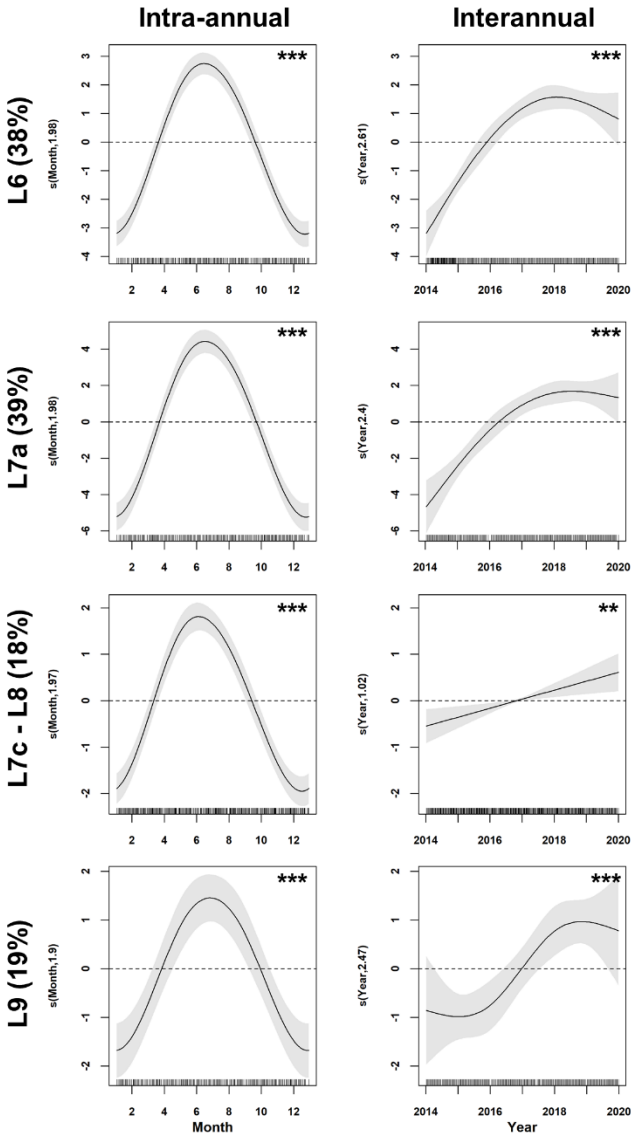

Appendix C.3 – Generalized additive models (GAM) of DSP abundance temporal variability, using month and year as covariates. For each region, the model explanatory power (as % of DSP variance explained) is presented in brackets after region abbreviation, and the significance level (p-value) of each predictor is denoted by asterisk symbols (top right), where *, **, *** indicate p-value <0.05, <0.01 and <0.001, respectively. In the left column are the plots representing intra-annual variability, and in the right column, the plots of interannual variability for each region. The solid line is the fitted model and grey shaded areas represent the 95% confidence intervals. The short vertical lines on the x-axis represent the actual predictor observations, and the values on the y-axis denote the effective degrees of freedom (edf). Edf values of 1 represent a linear effect of the predictor on DSP abundance, and values higher than 1 indicate non-linear effects. Positive (negative) y-values indicate that the predictor exerts a positive (negative) influence on DSP abundance.

Table C.3 – Summary results of the best-performing generalized additive models (GAM) used to decompose region-specific DSP abundance time series into seasonal and interannual components. Information includes total explained deviance, smoothing parameter estimation using the restricted maximum likelihood (REML) method, Akaike's Information Criteria (AIC), parametric coefficients (intercept ± standard error) and test statistic (z/Chi-square

value), estimated degrees of fredoom (edf) and significance level (p-value) for the model covariates. Smoothing functions are represented by s(i), for each covariate. k values associated with the smoothing functions represent restrictions to edf values. Edf values of 1 imply a linear effect and values higher than 1 indicate non-linear effects. k values indicate the estimated dispersion parameter. Asterisk symbols are associated with different p-value cutoff scores: <0.05 (*); <0.01 (**); <0.001 (***).

Model L6	**n**	**Coefficients**	**(Std. Error)**	**z(Chi.sq)-value**	**p-value**	**edf**	**k**	**Deviance expl. (%)**	**-REML**	**AIC**
DSP_abundance_rd ~ s(Month, k=4) + s(Year, k=4)	347	Intercept	4.4887 (0.142)	31.55	<2e-16 ***	-	0.145	37.9	1437.5	2870.3
		s(Month)	-	215.9	<2e-16 ***	1.981				
		s(Year)	-	114.0	<2e-16 ***	2.605				

Model L7a	**n**	**Coefficients**	**(Std. Error)**	**z(Chi.sq)-value**	**p-value**	**edf**	**k**	**Deviance expl. (%)**	**-REML**	**AIC**
DSP_abundance_rd ~ s(Month, k=4) + s(Year, k=4)	290	Intercept	4.4087 (0.235)	18.79	<2e-16 ***	-	0.067	39.2	870.5	1740.4
		s(Month)	-	197.51	<2e-16 ***	1.981				
		s(Year)	-	62.49	<2e-16 ***	2.403				

Model L7c-L8	n	Coefficients (Std. Error)		z(Chi.sq)-value	p-value	edf	k	Deviance explained (%)	-REML	AIC
DSP_abundance_rd ~ s(Month, k=4) + s(Year, k=4)	655	Intercept	5.3732 (0.106)	50.82	<2e-16 ***	-	0.137	18.1	3050	6096.3
		s(Month)	-	153.778	<2e-16 ***	1.975				
		s(Year)	-	9.191	0.003 **	1.015				

Model L9	n	Coefficients (Std. Error)		z(Chi.sq)-value	p-value	edf	k	Deviance expl. (%)	-REML	AIC
DSP_abundance_rd ~ s(Month, k=4) + s(Year, k=4)	299	Intercept	4.8910 (0.186)	26.27	<2e-16 ***	-	0.097	18.5	1143.2	2287.6
		s(Month)	-	36.44	<2e-16 ***	1.898				
		s(Year)	-	18.84	3.05e-04 ***	2.467				

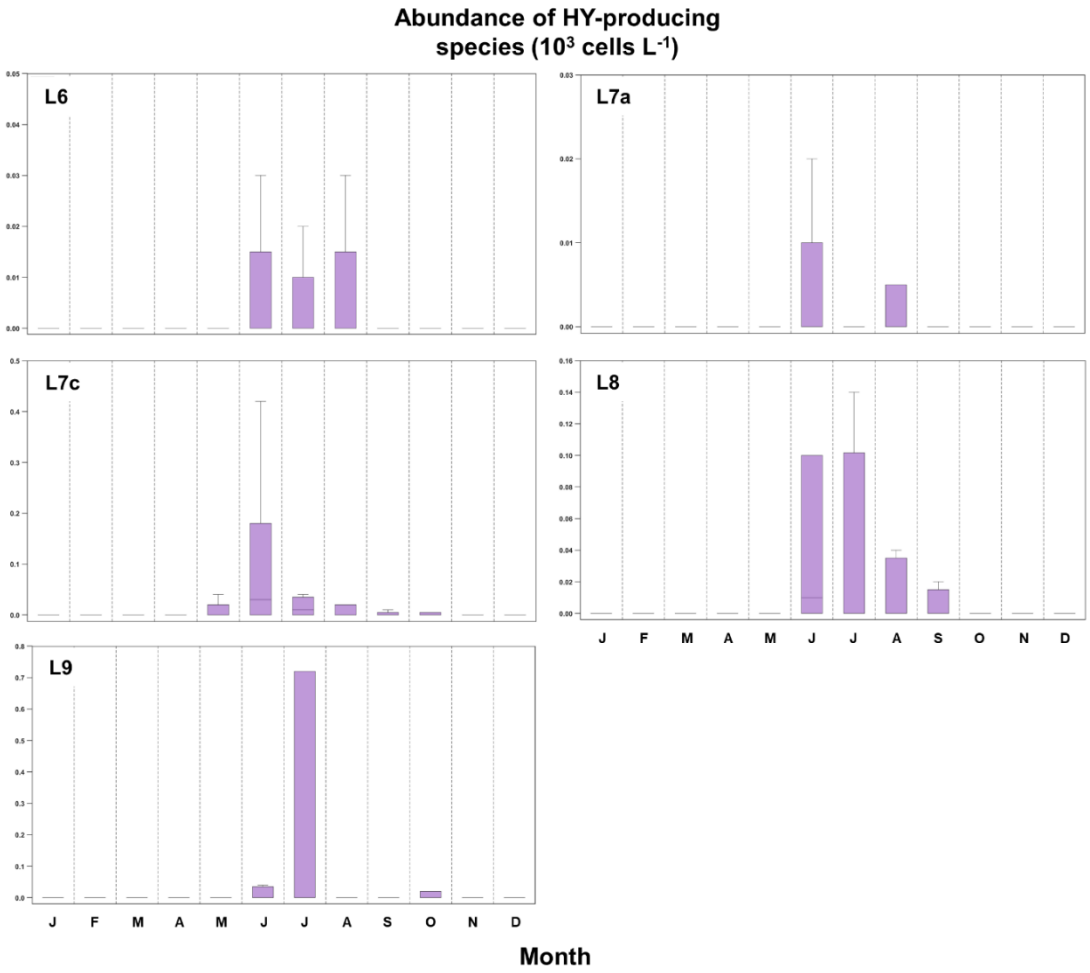

Appendix D.1 - Seasonal variability of the abundance of HY-producing species, for each coastal bivalve production area, during the period 2014-2019. Median values are identified by the central line within the box, the bottom and top edges of the box indicate the 25th and 75th percentiles, respectively, and the whiskers represent non-outlier limits.

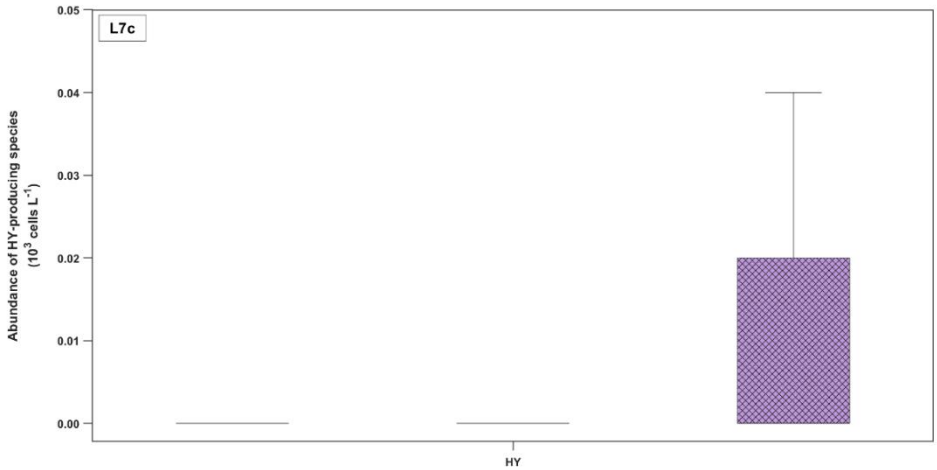

Appendix D.2 - Variability of the abundance of HY-producing species, in L7c area, according to three different physical regimes estimated with the upwelling index based on wind (UI_{ET}): upwelling-favourable (single line bending upwards), downwelling-favourable (single line bending downwards) and mixed (crossed lines). Median values are identified by the central

line within the box, the bottom and top edges of the box indicate the 25th and 75th percentiles, respectively, and the whiskers represent non-outlier limits.

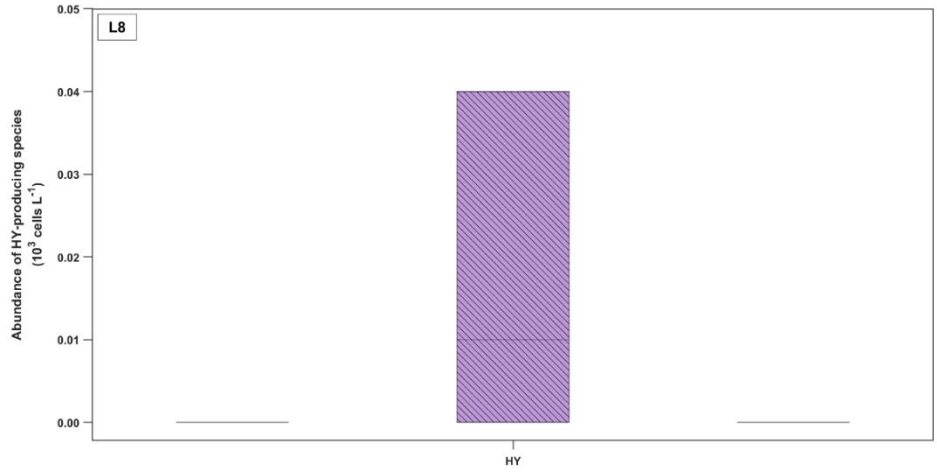

Appendix D.3 - Variability of the abundance of HY-producing species, in L8 area, according to three different physical regimes estimated with the alongshore velocity component measured at Armona site (see Figure 2.1 for location): upwelling-favourable (single line bending upwards), downwelling-favourable (single line bending downwards) and mixed (crossed lines). Median values are identified by the central line within the box, the bottom and top edges of the box indicate the 25th and 75th percentiles, respectively, and the whiskers represent non-outlier limits.

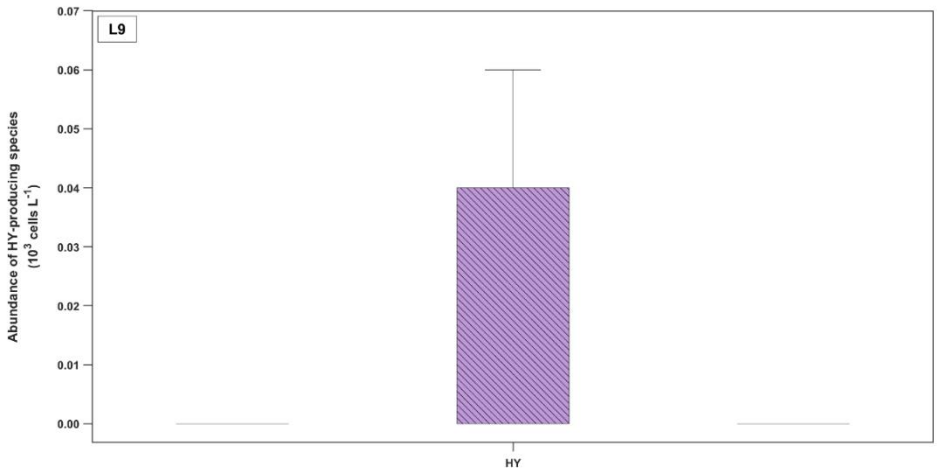

Appendix D.4 - Variability of the abundance of HY-producing species, in L9 area, according to three different physical regimes estimated with the alongshore velocity component measured at Armona site (see Figure 2.1 for location): upwelling-favourable (single line bending upwards), downwelling-favourable (single line bending downwards) and mixed (crossed lines). Median values are identified by the central line within the box, the bottom and top edges of the box indicate the 25th and 75th percentiles, respectively, and the whiskers represent non-outlier limits.

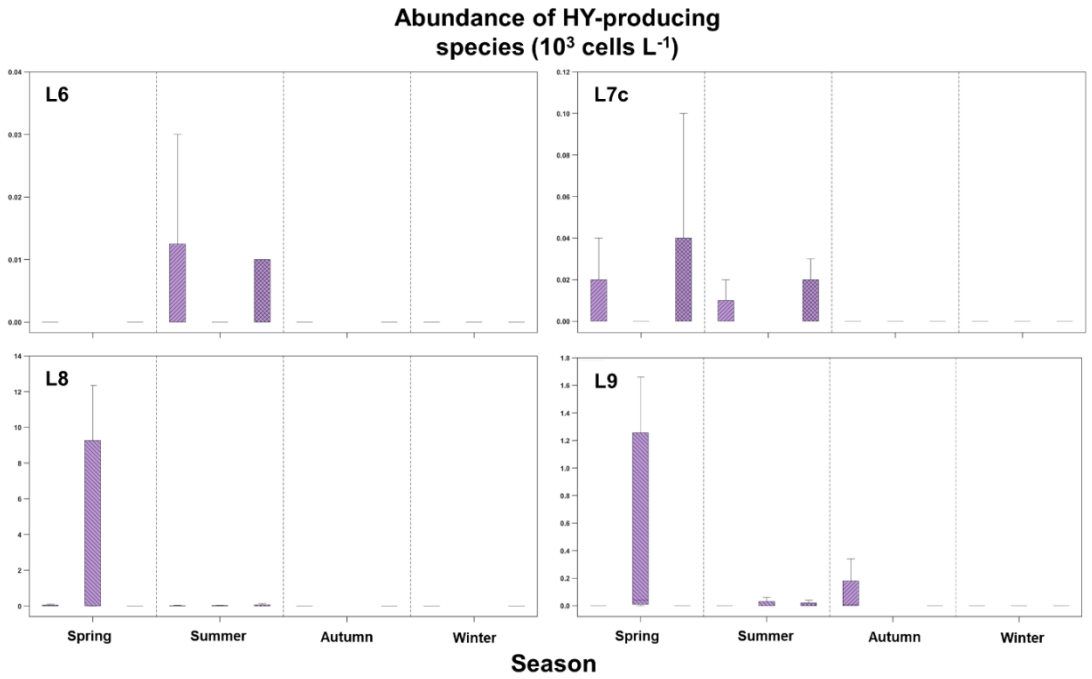

Appendix D.5 - Variability in HY-producing species abundance, according to three different physical regimes estimated with the upwelling index based on wind (UI_{ET}): upwelling-favourable (single line bending upwards), downwelling-favourable (single line bending downwards) and mixed (crossed lines), for the four seasons of the year. Median values are identified by the central line within the box, the bottom and top edges of the box indicate the 25th and 75th percentiles, respectively, and the whiskers represent non-outlier limits.

Table E.1 – Summary results of the best-performing generalized additive mixed models (GAMM) used to identify the most relevant environmental predictors of Chl-a variability. Thus, only statistically significant covariates were preserved in the models. Information includes model adjusted coefficient of determination (Adj. R^2), Akaike's Information Criteria (AIC), parametric coefficients (intercept ± standard error) and test statistic (t/F value), estimated degrees of fredoom (edf) and significance level (p-value) for the model covariates. Smoothing functions are represented by s(i), for each covariate. Edf values of 1 imply a linear effect and values higher than 1 indicate non-linear effects. Asterisk symbols are associated with different p-value cutoff scores: <0.05 (*); <0.01 (**); <0.001 (***).

Model WOff	n	Coefficients (Std. Error)		t(F)-value	p-value	edf	Adj. R-sq.	AIC
log(Chla) ~ s(SST) + s(MLD)	276	Intercept	-0.6751 (0.018)	-38.1	<2e-16 ***	-	0.523	-603.4
		s(SST)	-	77.855	<2e-16 ***	1.000		
		s(MLD)	-	9.136	2.37e-06 ***	3.628		

Model GoC	n	Coefficients (Std. Error)		t(F)-value	p-value	edf	Adj. R-sq.	AIC
log(Chla) ~ s(SST) + s(PAR) + s(EA)	275	Intercept	-0.8044 (0.012)	-68.89	<2e-16 ***	-	0.765	-792.3
		s(SST)	-	42.509	<2e-16 ***	3.692		
		s(PAR)	-	4.110	0.016 *	2.129		
		s(EA)	-	4.962	0.027 *	1.000		

Model SSlp	n	Coefficients (Std. Error)		t(F)-value	p-value	edf	Adj. R-sq.	AIC
log(Chla) ~ s(SST)	276	Intercept	-0.6308 (0.016)	-40.55	<2e-16 ***	-	0.486	-753.8
		s(SST)	-	94.08	<2e-16 ***	1.000		

Model WC	n	Coefficients (Std. Error)		t(F)-value	p-value	edf	Adj. R-sq.	AIC
log(Chla) ~ s(SST) + s(MLD) + s(AMO)	275	Intercept	-0.2443 (0.025)	-9.924	<2e-16 ***	-	0.135	-329.2
		s(SST)	-	53.574	<2e-16 ***	2.242		
		s(MLD)	-	6.172	2.22e-05 ***	5.605		
		s(AMO)	-	8.864	0.003 **	1.000		

Model SC	n	Coefficients (Std. Error)		t(F)-value	p-value	edf	Adj. R-sq.	AIC
log(Chla) ~ s(SST) + s(Gdq) + s(PAR)	274	Intercept	-0.4853 (0.018)	-26.81	<2e-16 ***	-	0.444	-608.2
		s(SST)	-	119.154	<2e-16 ***	1.000		
		s(Gdq)	-	2.751	0.040 *	1.733		

		s(PAR)	-	3.921	0.049 *	1.000		

Model Gdn	n	Coefficients (Std. Error)		t(F)-value	p-value	edf	Adj. R-sq.	AIC
log(Chla) ~ s(SST) + s(Gdq)	273	Intercept	-0.3665 (0.015)	-23.98	<2e-16 ***	-	0.602	-458.1
		s(SST)	-	130.660	<2e-16 ***	1.000		
		s(Gdq)	-	12.350	4.25e-06 ***	2.240		

Table E.2 – Summary results of the best-performing generalized additive models (GAM) used to identify the most relevant environmental predictors of ASP abundance. Information includes total explained deviance, smoothing parameter estimation using the restricted maximum likelihood (REML) method, Akaike's Information Criteria (AIC), parametric coefficients (intercept ± standard error) and test statistic (z/Chi-square value), estimated degrees of fredoom (edf) and significance level (p-value) for the model covariates. Smoothing functions are represented by s(i), for each covariate. Edf values of 1 imply a linear effect and values higher than 1 indicate non-linear effects. k values indicate the estimated dispersion parameter. Asterisk symbols are associated with different p-value cutoff scores: <0.05 (*); <0.01 (**); <0.001 (***).

Model L6	n	Coefficients (Std. Error)		z (Chi.sq)-value	p-value	edf	k	Deviance expl. (%)	-REML	AIC
ASP_abundance_rd ~ s(SST) +s(log10_Chla)	302	Intercept	8.7500 (0.164)	53.23	<2e-16 ***	-	0.123	7.58	2287.2	4578
		s(SST)	-	20.268	4.85e-04 ***	3.039				
		s(log10_Chla)	-	9.894	0.002 **	1.001				

Model L7a	n	Coefficients (Std. Error)		z (Chi.sq)-value	p-value	edf	k	Deviance expl. (%)	-REML	AIC
ASP_abundance_rd ~ s(PAR)	253	Intercept	9.0618 (0.261)	34.7	<2e-16 ***	-	0.058	6.64	1488.9	2982.1

		s(PAR)	-	17.6	2.82e-05 ***	1.000				

Model L7c-L8	n	Coefficients (Std. Error)		z (Chi.sq)-value	p-value	Edf	k	Deviance expl. (%)	-REML	AIC
ASP_abundance_rd ~ s(MLD) + s(SST) + s(Gdq)	575	Intercept	9.4043 (0.143)	65.98	<2e-16 ***	-	0.086	7.36	4103.1	8209.6
		s(MLD)	-	32.831	5.02e-07 ***	2.223				
		s(SST)	-	24.140	3.13e-05 ***	2.557				
		s(Gdq)	-	7.548	0.006 **	1.013				

Model L9	n	Coefficients (Std. Error)		z (Chi.sq)-value	p-value	edf	k	Deviance expl. (%)	-REML	AIC
ASP_abundance_rd ~ s(Along_vel) + s(Gdn)	162	Intercept	8.5164 (0.377)	22.58	<2e-16 ***	-	0.043	7.52	783.07	1573.9
		s(Along_vel)	-	3.943	0.047 *	1.001				
		s(Gdn)	-	4.373	0.039 *	1.020				

Table E.3 – Summary results of the best-performing generalized additive models (GAM) used to identify the most relevant environmental predictors of DSP abundance. Information includes total explained deviance, smoothing parameter estimation using the restricted maximum likelihood (REML) method, Akaike's Information Criteria (AIC), parametric coefficients (intercept ± standard error) and test statistic (z/Chi-square value), estimated degrees of fredoom (edf) and significance level (p-value) for the model covariates. Smoothing functions are represented by s(i), for each covariate. k values associated with the smoothing functions represent restrictions to edf values. Edf values of 1 imply a linear effect and values higher than 1 indicate non-linear effects. k values indicate the estimated dispersion parameter. Asterisk symbols are associated with different p-value cutoff scores: <0.05 (*); <0.01 (**); <0.001 (***).

Model L6	n	Coefficients (Std. Error)		z (Chi.sq)-value	p-value	edf	k	Deviance expl. (%)	-REML	AIC
DSP_abundance_rd ~ s(PAR, k=4) + s(MLD) + s(SST, k=4) + s(CSET_WC)	302	Intercept	4.6586 (0.157)	29.72	<2e-16 ***	-	0.139	36.3	1271.8	2545.0
		s(PAR)	-	34.21	5.23e-08 ***	2.858				
		s(MLD)	-	24.80	1.41e-06 ***	1.001				
		s(SST)	-	11.61	6.60e-04 ***	1.001				
		s(CSET_WC)	-	16.83	0.001 **	2.666				

Model L7a	n	Coefficients (Std. Error)		z (Chi.sq)-value	p-value	edf	k	Deviance expl. (%)	-REML	AIC
DSP_abundance_rd ~ s(log10_Chla) + s(MLD) + s(PAR) + s(SST, k=4)	253	Intercept	2.770 (0.926)	2.991	0.003 **	-	0.083	54.4	757.7	1518.3
		s(log10_Chla)	-	46.17	<2e-16 ***	5.593				
		s(MLD)	-	38.04	3.47e-06 ***	4.724				
		s(PAR)	-	31.50	7.41e-06 ***	4.044				
		s(SST)	-	13.27	0.003 **	2.519				

Model L7c-L8	n	Coefficients (Std. Error)		z (Chi.sq)-value	p-value	edf	k	Deviance expl. (%)	-REML	AIC
DSP_abundance_rd ~ s(PAR) + s(log10_Chla) + s(Gdq, k=4) + s(Along_vel)	359	Intercept	5.0321 (0.129)	38.99	<2e-16 ***	-	0.185	35.8	1809.4	3617.9
		s(PAR)	-	67.732	<2e-16 ***	2.795				
		s(log10_Chla)	-	49.637	<2e-16 ***	5.252				
		s(Gdq)	-	16.826	0.001 **	2.497				
		s(Along_vel)	-	9.814	0.021 *	2.380				

Model L9	n	Coefficients (Std. Error)		z (Chi.sq)-value	p-value	edf	k	Deviance expl. (%)	-REML	AIC
DSP_abundance_rd ~ s(PAR) + s(Gdn) + s(Along_vel)	144	Intercept	5.3523 (0.262)	20.46	<2e-16 ***	-	0.102	21.1	606.9	1221.3
		s(PAR)	-	18.356	1.82e-05 ***	1.000				
		s(Gdn)	-	6.069	0.014 *	1.001				
		s(Along_vel)	-	6.788	0.043 *	1.425				

Table F.1 – Descriptive statistics of phytoplankton phenological indices for the six regions off southern Portugal, estimated for each annual cycle (September – August), during the period 2014-2019. Information included minimum (Min), maximum (Max) and mean values and standard deviation (SD).

Phenological Index	Min - Max						Mean ± SD					
	WOff	GoC	SSlp	WC	SC	Gdn	WOff	GoC	SSlp	WC	SC	Gdn
Number of bloom events per year (bloom events year^{-1})	1 - 4	1 - 3	1-3	4 - 6	2 - 4	1 - 6	2.50 ± 1.38	1.67 ± 0.82	2 ± 0.89	4.67 ± 0.82	3 ± 0.89	3.33 ± 2.07
Average duration of bloom events (weeks bloom^{-1})	4 - 19	6.33 - 20	6-13	2.80 - 5.25	4 - 10	3.17 - 15	9.51 ± 6.59	13.31 ± 5.26	9.50 ± 3.10	3.88 ± 0.89	6.11 ± 2.05	7.36 ± 4.70
Total duration of all bloom events per year (weeks year^{-1})	13 - 19	15 - 22	13-21	14 - 21	12 - 20	11 - 20	16.67 ± 2.25	18.83 ± 2.32	16.83 ± 3.71	17.67 ± 2.58	17.17 ± 2.99	17 ± 3.41
Chlorophyll-a peak value (µg L^{-1})	0.38 - 0.77	0.28 - 0.44	0.38 - 0.55	1.25 - 1.75	0.55 - 0.83	0.89 - 1.68	0.59 ± 0.16	0.36 ± 0.06	0.47 ± 0.06	1.56 ± 0.17	0.68 ± 0.10	1.21 ± 0.35
Chl-a peak timing of the principal bloom (week of the year)	22 - 28	22 - 25	22 - 27	31 - 43	22 - 27	21 - 32	24 ± 2.45	24 ± 1.10	24.33 ± 1.75	35.50 ± 5.47	24.17 ± 1.72	24.67 ± 3.98
Chl-a peak timing of secondary blooms (week of the year)	11 - 33	12 - 43	1 - 44	1 - 45	1 - 45	5 - 44	22.33 ± 7.81	28.50 ± 14.89	30.50 ± 19.30	26.23 ± 13.33	32.33 ± 14.78	26.79 ± 12.78
Timing of the principal bloom initiation (week of the year)	7.42 - 26.15	8.94 - 14.24	10.53 - 18.32	26.20 - 40.53	10.31 - 20.66	8.17 - 21.07	16.51 ± 8.17	11.32 ± 2.44	16 ± 3.19	33.27 ± 6.64	17.31 ± 4.22	17.21 ± 5.20
Timing of initiation for secondary bloom events (week of the year)	9.42 - 31.62	8.76 - 42.29	1 - 42.07	1 - 39.69	1 - 41.71	4.29 - 43.48	19.77 ± 7.33	24.92 ± 15.11	29.18 ± 16.95	23.14 ± 13.06	29.94 ± 13.65	24.60 ± 13.02

Timing of the principal bloom termination (week of the year)	26.79 - 32.75	28.22 - 31.14	27.64 - 33.79	32.90 - 46	24.94 - 33.41	26.74 - 33.88	28.94 ± 2.21	29.86 ± 0.97	29.80 ± 2.21	37.81 ± 5.98	29.18 ± 2.92	29.18 ± 2.52
Timing of termination for secondary bloom events (week of the year)	12.95 - 35.83	13.68 - 44.43	2.23 - 46	4.27 - 46	2.83 - 46	6.50 - 45.58	24.64 ± 7.64	31.57 ± 13.75	32.12 ± 18.98	28.21 ± 13.16	33.86 ± 14.80	28.56 ± 12.61
Principal bloom duration (weeks year^{-1})	3.70 - 19.45	15.33 - 20.74	10.66 - 17.37	3.53 - 7.69	6.01 - 17.46	8.09 - 19.75	12.44 ± 6.28	18.43 ± 2.04	14.13 ± 2.99	5.52 ± 1.64	12.07 ± 4.24	12.15 ± 5.27
Duration of the principal bloom accumulation phase (weeks year^{-1})	1.85 - 15.58	10.57 - 15.06	3.74 - 13.47	0.99 - 5.80	3.08 - 13.69	1.93 - 15.83	7.69 ± 5.86	12.48 ± 1.86	8.60 ± 3.44	2.93 ± 1.87	6.89 ± 4.04	7.99 ± 6.42
Duration of the principal bloom deceleration phase (weeks year^{-1})	1.85 - 6.75	4.22 - 7.84	1.98 - 8.79	0.90 - 4	2.94 - 8.41	1.88 - 6.97	4.94 ± 1.86	5.86 ± 1.42	5.47 ± 2.69	2.31 ± 1.04	5.02 ± 2.12	4.51 ± 2.13

Table F.2 – Descriptive statistics of phytoplankton phenological indices for the five coastal bivalve production areas, estimated for each HAB annual cycle (January-December), considering ASP-producing species, during the period 2014-2019. Information included minimum (Min), maximum (Max) and mean values and standard deviation (SD).

Phenological Index	**Min - Max**					**Mean ± SD**				
	L6	**L7a**	**L7c**	**L8**	**L9**	**L6**	**L7a**	**L7c**	**L8**	**L9**
Number of bloom events per year (bloom events year^{-1})	2 - 3	0 - 3	0 - 3	0 - 2	2 - 3	2.67 ± 0.52	1.67 ± 1.21	1.17 ± 0.98	1.17 ± 0.75	2.17 ± 0.41
Average duration of bloom events (weeks bloom^{-1})	3.50 - 6.17	0 - 14.88	0 - 5.25	0 - 4	2.63 - 5.50	4.40 ± 1	4.61 ± 5.20	3.16 ± 1.86	2.75 ± 1.52	3.35 ± 1.10
Total duration of all bloom events per year (weeks year^{-1})	7 - 18.50	0 - 14.88	0 - 12.25	0 - 8	5.25 - 11	11.92 ± 4.23	7.48 ± 5.57	4.52 ± 4.19	4 ± 3.02	7.29 ± 2.70

ASP-producing species peak value (cells L^{-1})	17570 - 149650	0 - 297250	0 - 607620	0 - 311482	9424 - 256250	61501.34 ± 39375.57	76167.18 ± 82982.72	150937.50 ± 206616.46	93248.25 ± 105664.28	94190.38 ± 82521.48
ASP-producing species peak timing of all blooms (week of the year)	5 - 42.75	0 - 34.75	0 - 40	0 - 38.63	6.75 - 40.38	20.58 ± 10.63	23.29 ± 7.90	20.93 ± 11.78	22.95 ± 12.40	21.10 ± 12.33
Timing of initiation for all bloom events (week of the year)	4.15 - 41.23	0 - 31.38	0 - 37.88	0 - 35.38	5 - 37.50	17.59 ± 10.12	21.13 ± 7.20	18.15 ± 12.07	20.96 ± 11.91	18.63 ± 12.09
Timing of termination for all bloom events (week of the year)	9.34 - 44.59	0 - 36.60	0 - 41.38	0 - 40.38	10.25 - 43.25	23.32 ± 10.08	27.55 ± 7.30	23.10 ± 11.20	25.81 ± 12.45	23.88 ± 12.65
All blooms duration (weeks $year^{-1}$)	3.16 - 13.13	0 - 16.63	0 - 7.88	0 - 8.25	4.38 - 9.13	5.74 ± 2.44	5.83 ± 4.03	4.33 ± 2.33	4.24 ± 2.29	5.25 ± 1.33
Duration of all blooms accumulation phase (weeks $year^{-1}$)	0.85 - 11.38	0 - 4.27	0 - 5.13	0 - 3.25	0.88 - 5.25	2.99 ± 2.54	1.96 ± 1.29	2.43 ± 1.60	1.73 ± 1.24	2.46 ± 1.14
Duration of all blooms deceleration phase (weeks $year^{-1}$)	0.75 - 6.85	0 - 14	0 - 4.02	0 - 5.38	0.75 - 7.38	2.75 ± 1.67	3.87 ± 3.66	1.90 ± 1.22	2.51 ± 1.69	2.79 ± 1.74

Table F.3 – Descriptive statistics of phytoplankton phenological indices for the five coastal bivalve production areas, estimated for each HAB annual cycle (January-December), considering DSP-producing species, during the period 2014-2019. Information included minimum (Min), maximum (Max) and mean values and standard deviation (SD).

Phenological Index	**Min - Max**					**Mean ± SD**				
	L6	**L7a**	**L7c**	**L8**	**L9**	**L6**	**L7a**	**L7c**	**L8**	**L9**
Number of bloom events per year (bloom events $year^{-1}$)	1 - 3	1 - 2	1 - 3	0 - 4	0 - 3	2.17 ± 0.75	1.50 ± 0.55	2.33 ± 0.82	1.83 ± 1.47	1.33 ± 1.03
Average duration of bloom events (weeks $bloom^{-1}$)	2.75 - 7	2.69 - 6.13	2.58 - 3.69	0 - 7	0 - 4.67	4.14 ± 1.55	4.96 ± 1.17	3.06 ± 0.46	3.05 ± 2.35	2.80 ± 1.58

Total duration of all bloom events per year (weeks year^{-1})	3.50 - 14	5.25 - 10.50	2.75 - 10.13	0 - 15.50	0 - 14	9.10 ± 4.60	7.15 ± 2.57	7.08 ± 2.42	7.25 ± 6.74	4.94 ± 4.98
DSP-producing species peak value (cells L^{-1})	90 - 192920	40 - 685720	80 - 429160	0 - 6540	0 - 1780	15396.69 ± 53342.23	77148.89 ± 228226.15	33025.93 ± 114084.94	1735.56 ± 2165.56	645 ± 668.52
DSP-producing species peak timing of all blooms (week of the year)	15 - 36.88	14.38 - 36.63	13.88 - 37.38	0 - 34.75	0 - 37.63	28.52 ± 6.84	23.26 ± 7.41	24.56 ± 8.59	20.30 ± 8.47	24.80 ± 7.08
Timing of initiation for all bloom events (week of the year)	13.50 - 36.06	13.38 - 28.38	10.46 - 36.63	0 - 32.48	0 - 34.24	26.08 ± 7.06	19.68 ± 5.52	22.84 ± 8.44	17.43 ± 8.03	22.35 ± 6.90
Timing of termination for all bloom events (week of the year)	18 - 39.90	17.75 - 37.50	16.46 - 40	0 - 35.41	0 - 38.49	31.49 ± 6.93	26.25 ± 6.43	27.15 ± 8.58	22.67 ± 8.34	27.78 ± 6.93
All blooms duration (weeks year^{-1})	3.62 - 10.47	4.13 - 10.50	2.75 - 7.77	0 - 9.47	0 - 8.73	5.41 ± 2.32	6.57 ± 2.43	4.31 ± 1.37	4.80 ± 2.37	4.83 ± 2.27
Duration of all blooms accumulation phase (weeks year^{-1})	0.82 - 6.54	0.75 - 8.75	0.12 - 3.42	0 - 7.74	0 - 6.99	2.44 ± 1.58	3.58 ± 2.80	1.72 ± 1.14	2.63 ± 2.07	2.18 ± 2.17
Duration of all blooms deceleration phase (weeks year^{-1})	0.63 - 6.09	0.88 - 9.63	0.12 - 4.42	0 - 5.12	0 - 5.25	2.97 ± 1.58	2.99 ± 2.74	2.59 ± 1.25	2.18 ± 1.45	2.66 ± 1.72

Table F.4 – Descriptive statistics of phytoplankton phenological indices for the five coastal bivalve production areas, estimated for each HAB annual cycle (January-December), considering PSP-producing species, during the period 2014-2019. Information included minimum (Min), maximum (Max) and mean values and standard deviation (SD).

Phenological Index	**Min - Max**					**Mean ± SD**				
	L6	**L7a**	**L7c**	**L8**	**L9**	**L6**	**L7a**	**L7c**	**L8**	**L9**
Number of bloom events per year (bloom events year^{-1})	0 - 1	0 - 1	0 - 3	0 - 2	0 - 1	0.50 ± 0.55	0.67 ± 0.52	1 ± 1.26	0.67 ± 1.03	0.50 ± 0.55

Average duration of bloom events (weeks bloom^{-1})	0 - 2.63	0 - 4.38	0 - 3.75	0 - 4.44	0 - 4.13	1.25 ± 1.38	2.04 ± 1.72	1.68 ± 1.87	1.31 ± 2.06	1.71 ± 1.93
Total duration of all bloom events per year (weeks year^{-1})	0 - 2.63	0 - 4.38	0 - 11.25	0 - 8.88	0 - 4.13	1.25 ± 1.38	2.04 ± 1.72	3.52 ± 4.70	2.63 ± 4.12	1.71 ± 1.93
PSP-producing species peak value (cells L^{-1})	0 - 4750	0 - 660	0 - 3180	0 - 3126.67	0 - 3040	861.67 ± 1909.43	246.67 ± 261.89	443.33 ± 1029.95	535.83 ± 1071.39	610 ± 1200.92
PSP-producing species peak timing of all blooms (week of the year)	0 - 35.38	0 - 28.25	0 - 43.88	0 - 29	0 - 11.38	20.75 ± 12.73	16.78 ± 7.90	22.35 ± 14.71	18.53 ± 8.55	9.21 ± 3.54
Timing of initiation for all bloom events (week of the year)	0 - 33.50	0 - 26.50	0 - 41.74	0 - 27.28	0 - 8.96	18.63 ± 12.88	14.78 ± 8.06	19.89 ± 14.95	16.87 ± 8.71	6.20 ± 4.50
Timing of termination for all bloom events (week of the year)	0 - 37.88	0 - 31.75	0 - 46	0 - 31.36	0 - 14.70	22.79 ± 13.12	19.84 ± 8.06	24.81 ± 14.20	21.73 ± 7.36	11.61 ± 4.17
All blooms duration (weeks year^{-1})	0 - 5.25	0 - 6.25	0 - 7	0 - 7.40	0 - 6.07	2.08 ± 2.41	3.38 ± 2.70	3.28 ± 2.64	2.43 ± 2.89	2.71 ± 3.03
Duration of all blooms accumulation phase (weeks year^{-1})	0 - 3.50	0 - 2.63	0 - 3.50	0 - 2.45	0 - 4.13	1.06 ± 1.41	1.33 ± 1.08	1.64 ± 1.43	0.83 ± 0.97	1.51 ± 1.77
Duration of all blooms deceleration phase (weeks year^{-1})	0 - 2.50	0 - 4.50	0 - 4.61	0 - 6.01	0 - 3.32	1.02 ± 1.15	2.04 ± 1.83	1.64 ± 1.62	1.60 ± 2.12	1.20 ± 1.42

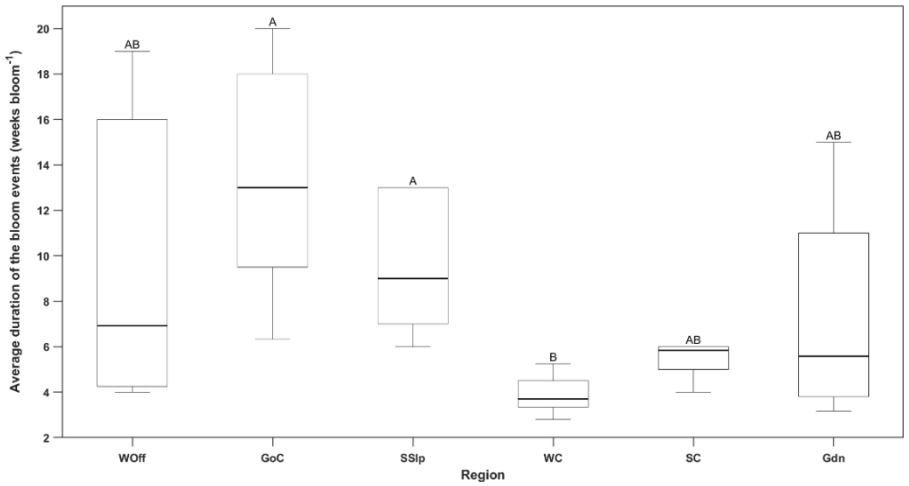

Appendix F.1 – Average duration of the bloom events for the six regions off southern Portugal, estimated for each annual cycle (September-August) during the period 2014-2019. Median values are identified by the central line within the box, the bottom and top edges of the box indicate the 25th and 75th percentiles, respectively, and the whiskers represent non-outlier limits. Different uppercase letters over the bars denote significant differences across regions ($p < 0.05$).

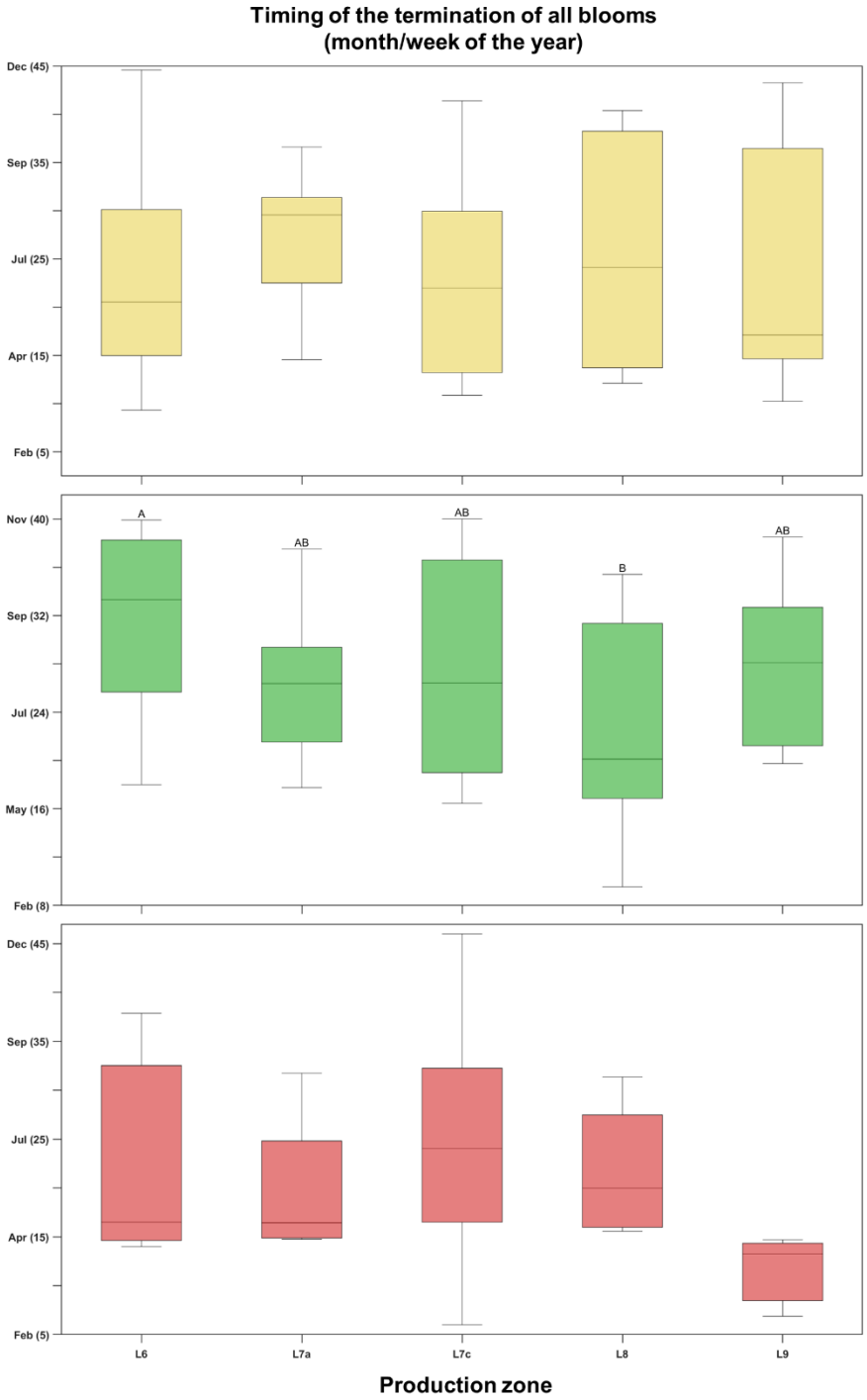

Appendix F.2 – Timing of all blooms termination for the five coastal bivalve production areas, estimated for each HAB annual cycle (January-December), considering the three most frequently reported toxin-producing groups (ASP, DSP, and PSP represented by yellow, green and red colors, respectively), during the period 2014-2019. Median values are identified by the central line within the box, the bottom and top edges of the box indicate the 25th and 75th percentiles, respectively, and the whiskers represent non-outlier limits. For each group, different uppercase letters over the bars denote significant differences across regions ($p < 0.05$).

Table G.1 – Spearman rank correlation (r_s) coefficients, and corresponding number of samples (N), to evaluate the strength of monotonic relationships between the abundance of three specific toxigenic groups responsible for ASP (Amnesic Shellfish Poisoning), DSP (Diarrhetic Shellfish Poisoning) and PSP (Paralytic Shellfish Poisoning) human syndromes, and the respective toxin concentration in two bivalve species (*Mytilus* spp. and *Donax trunculus*), for the five coastal bivalve production areas, during the period 2014-2019. '-' refer to production areas where toxins were not detected in specific bivalve species. Asterisk symbols are associated with different p-value cutoff scores: <0.05 (*); <0.01 (**).

HAB group	Production Area	*Mytilus* spp.		*Donax trunculus*	
		r	**N**	**r**	**N**
ASP-producing species (x 10^3 cells L^{-1})	L6	-0.22*	108	0.20	50
	L7a	-0.20*	94	-	-
	L7c	0.13	213	0.54	9
	L8	-0.22	80	0.02	114
	L9	-	-	0.05	88
DSP-producing species (x 10^3 cells L^{-1})	L6	0.29**	95	0.59**	56
	L7a	0.36**	86	-	-
	L7c	0.47**	188	0.20	9
	L8	0.39**	78	0.39**	121
	L9	-	-	0.30**	101
PSP-producing species (x 10^3 cells L^{-1})	L6	-0.04	110	0.28*	57
	L7a	0.09	93	-	-
	L7c	-3.44E-03	203	0.59	9
	L8	0.05	75	0.09	115
	L9	-	-	0.08	84